An Evaluation of the History of Aqueous Activity on Mars through a Survey of Select Hypothesized Martian Deltas and Paleolakes via the Analysis of Mineralogy, Morphology, and Thermophysical Properties

A Thesis Presented for the
Master of Science
Degree
The University of Tennessee, Knoxville

Andréa C. G. Hughes
May, 2012

DEDICATION

"… Whatever you do, do it all for the glory of God."

– 1 Corinthians 10:31

ACKNOWLEDGEMENTS

First, thank you to my family, for supporting me in every way they could, for encouraging me to pursue my dreams and to persevere when things get hard, and for believing in me (before I even started) – and even for a little healthy competition sometimes; and to my friends for constant support and encouragement.

Second, thank you to my advisers, Devon and Jeff, for their great guidance, patience, support, and intellectual contributions; and for being great Jedi masters in teaching me the ways of Planetary Science. Also, thank you to my summer adviser, Scott, for thinking up this project, giving me the opportunity to work on it, and for having the patience to teach me about spectroscopy and CRISM; and for believing in me and supporting me from the beginning. Lastly, thank you, Chris, for "keeping one foot on the ground" by providing terrestrial insight to sometimes oversimplified planetary problems. I am thankful to all of my committee members for their intellectual contributions and emotional support. I believe it's true that "many advisers bring success" (Proverbs 15:22).

Thank you to my colleagues from respective work places: faculty, postdocs, and graduate students in the Earth and Planetary Sciences (EPS) department, and CRISM team members at APL (Frank & Kim Seelos, Frank Morgan, Debra Buczkowski, Jen, Chris, Harri, and Andy), for their time, help, knowledge, patience, and encouragement. Thank you to Alexandra Lefort (and others) for the use of data of Fan #22.

Finally, thank you to all financial supporters of this project, including the EPS department, an anonymous supporter within the department, the Johns Hopkins University Applied Physics Lab, and the AGI MPP Scholarship.

ABSTRACT

Aqueous deposits are an essential key to understanding the geologic/climatic history of water on Mars. The Compact Reconnaissance Imaging Spectrometer for Mars (CRISM), High Resolution Imaging Science Experiment (HiRISE), and Thermal Emission Imaging System (THEMIS) have enabled studies of Martian fan deposits in unprecedented detail, including the identification of hydrated minerals (such as phyllosilicates, carbonates, and sulfates) and morphologies consistent with formation in an aqueous environment associated with Martian sedimentary deposits. In this study, twenty-six previously identified fan-shaped deposits (hypothesized as possible deltas) have been examined for hydrated minerals in the beds and distal regions of the deposits. Six deposits have newly been identified to bear phyllosilicates (primarily Fe/Mg-smectites) and are characterized herein with regards to mineralogy, morphology, and thermophysical properties. The results of these analyses suggest that at least four of these deposits are consistent with formation in a deltaic environment; though other possible formation environments, such as alluvial fans and alluvial fan-deltas, should not be altogether excluded, as some of the deposits also bear resemblances to terrestrial examples of such features. The results of this study are consistent with Mars once having hosted aqueous environments in which flowing and standing water was sustainable on the surface, allowing the formation of deltas on Mars.

TABLE OF CONTENTS

ACKNOWLEDGEMENTS iii

ABSTRACT iv

LIST OF TABLES vii

LIST OF FIGURES viii

MASTERS THESIS 1

1. Introduction 1
2. Geologic Background 1
    - 2.1. Significance of the Identification of Deltas on Mars 1
    - 2.2. Significance of Hydrated Minerals on Mars 1
    - 2.3. Previous Studies of Possible Deltaic Deposits on Mars 2
3. Data and Methods 2
    - 3.1. Data 2
    - 3.2. Data Analysis 4
4. Observations and Interpretations 7
    - 4.1. Fan #26 7
    - 4.2. Fan #2 11
    - 4.3. Fan #21 15
    - 4.4. Fan #25 16
    - 4.5. Identifications of Hydrated Minerals in Other Deposits 18
5. Discussion 22
    - 5.1. Implications for Depositional Environments and Evaluation of Delta Hypothesis 22
    - 5.2. Authigenic versus Allogenic Phyllosilicate Formation 24
    - 5.3. Post-Depositional Modification of Deposits 24
    - 5.4. Inter-deposit Correlations of Thermal Inertia 25
    - 5.5. Correlations between Thermal Inertia and Mineralogy 26
    - 5.6. Caveats to Scientific Analysis Approach 27
    - 5.7. Applications and Significance 28

6. Summary and Conclusions 28
LIST OF REFERENCES 29
APPENDIX 34
1. Tables 35
2. Figures 39
VITA 84

LIST OF TABLES

Table 1: Data from each primary dataset associated with the deposits 35

Table 2: Hypothesized deltaic deposits discussed in this study (modified from Table 1 by Irwin *et al.*, 2005) 36

Table 3: Measurable/Observable Characteristics of Multiple Possible Fan Formation Processes 37

LIST OF FIGURES

Figure 1: Global map of Mars showing the locations of the 33 deposits (gray dots) discussed by Irwin *et al*. (2005). Boxes and names show respective locations of deposits focused on in this study (MOLA elevation Base map). 39

Figure 2: Portion of HRSC image H5212_0000 _ND4 showing area of Fan #26 located in the Nepenthes Mensae region, as well as the inlet valley, superposed deposit ("Deposit 1"), and distal knobs. Curvilinear arrow shows the path of tributary channel. Asterisks and oval show the locations (respectively) of hypothesized fluvial terraces and an elongate feature hypothesized to be a fissural volcano by de Pablo and Pacifici (2008). Inset shows regional context with associated CRISM images overlain (Figure 3A and Figure 3B). 40

Figure 3: A) CRISM phyllosilicate summary parameters(R: DB2300, G: 2210, B: BD1900) of data on/near Fan #26 overlain on grayscale HRSC image H5212_0000 _ND4. Red/magenta regions represent locations containing Fe/Mg-phyllosilicates, and green regions represent locations containing Al-phyllosilicates. The colored arrows show locations of the normalizing spectra used in spectral ratios in Figure 4A (arrow colors correspond to respective spectra). CRISM images in this figure are (from left to right) FRT1D7F0, FRT16525, and FRT147E0. B) CRISM phyllosilicate summary parameters overlain on IRB grayscale of CRISM image FRT16026 showing watershed and inlet valley of Fan #26 (circle shows location of normalizing spectra in spectral ratio). C) RGB composite of visible-wavelength CRISM summary parameters highlighting locations of oxidized iron minerals (R: BD530, G: SH600, B: BDI1000); areas abundant in dust appear red/orange/yellow in color, green colors primarily represent rocks with coatings/rinds on the surface, and blue colors represent areas bearing iron minerals (*e.g.*, olivine and pyroxene). All visible-wavelength CRISM summary parameter figures in this manuscript are stretched the same (R: 0.0000 – 0.1700, G: 0.1000 – 0.1700, B: 0.0000 – 0.0250) for qualitative comparison. D) CRISM summary parameters highlighting diversity in mafic minerals (R: OLINDEX, G: LCPINDEX, B: HCPINDEX) for data over Fan #26; magenta areas in right two images correspond with pyroxene-bearing sand dunes. 41

Figure 4: A) CRISM ratio spectra of Fe/Mg and Al-phyllosilicates in lower beds of, and on elevated knob distal to Fan #26. Absorption features of Fe/Mg-phyllosilicates are indicative of Fe/Mg-smectite, perhaps saponite and/or nontronite; absorption features of Al-phyllosilicates are indicative of Al-smectite, perhaps montmorillonite. The broadened spectra of Al-phyllosilicates may be due to mixing with hydrated silica, such as opal. B) CRISM ratio spectra of the inlet valley within watershed upstream of Fan #26 (FRT16026), showing absorption features consistent with phyllosilicates and pyroxene. C) Library reflectance spectra of saponite, nontronite, montmorillonite, and opal (hydrated silica). D) Ratio spectrum of pyroxene-bearing sand dunes distal to fans, and E) library spectrum of pyroxene for comparison. 44

Figure 5: A) Portion of CTX image B16_015980_1821_XN_02N238W showing Fan #26, stratigraphically superposed deposit, and nearby region. Boxes show the locations of images

in Figure 6, and black arrow labeled 'RG' points to example of radially-oriented gullies on the fan surface. B) Topographic profile of Fan #26, superposed deposit, and elongate depression distal to deposits.. 45

Figure 6: Portions of HiRISE images showing morphologies on/near Fan #26, superposed deposit, and surrounding area. A), B), & C) show fine-scale layering in beds of the supposed deposit; D) polygonally fractured terrain distal to Fan #26; E) distal fan beds eroding boulder-sized clast inclusions (white arrows pointing to some); F) concentric rings on the surface of fan #26, with layering exposed between rings; G) layering in lower beds of Fan #26, cross-cut by radially-oriented gullies; H) Parallel linear features (possibly layering) exposed on fan scarp; I) parallel features that cross-cut southern fan scarp at a steep angle, and features of similar size/orientation on the southern side of a distal fan mound - likely aeolian in origin. HiRISE image numbers are shown in figures; north is toward the top of images.. 46

Figure 7: THEMIS thermal inertia of phyllosilicate-bearing deposits in this study (TI units are in J m^{-2} K^{-1} $s^{-1/2}$) overlain on HRSC grayscale images (Fans #2, #21, #25, and #26) or CTX data (Fans #22 and #19 Distal Deposit). Solid white circles show locations of deposits, dashed circle on Fan #19 Distal Deposit approximately outlines degraded rim of crater containing the deposit, and dashed outline over Fan #22 shows approximate distal boundaries of this deposit. North is toward the top, and the width of each scene is 32km. Scene numbers of THEMIS night IR images from which these maps were derived (as well as HRSC data) are provided in Table 1. 47

Figure 8: A) CRISM summary parameters (R: DB2300, G: HCPINDEX, B: BD1900) of multiple targeted scenes in Ismenius Cavus, crater containing Fan #2, overlain on HRSC image with 100m elevation contours. Magenta areas represent locations bearing phyllosilicates, and green regions bear pyroxene. Black box shows locations of Figure 10 and Figure 11A. B) Portion of HiRISE image PSP_010419_2140 showing horizontally layered, polygonally fractured phyllosilicate-bearing region in the center of Ismenius Cavus crater (north is toward the top of image). C) CRISM visible-wavelength summary parameters of oxidized iron minerals (R: BD530, G: SH600, B: BDI1000) for data in Ismenius Cavus crater (overlain on HRSC data); areas abundant in dust appear orange-yellow in color (data stretch same as Figure 3C).. 48

Figure 9: A) CRISM ratio spectrum of Fe/Mg-phyllosilicates in the center of Ismenius Cavus crater, basin containing Fan #2. Absorption features are consistent with an Fe/Mg-smectite, perhaps nontronite. B) Library reflectance spectra of nontronite, saponite, and vermiculite for comparison. 51

Figure 10: CRISM image FRT00019B14 of phyllosilicate summary parameters (R: DB2300, G: 2210, B: BD1900) overlain on grayscale image, showing locations of possible presence of phyllosilicates (red/magenta regions) that are consistent with geomorphology on the surface of, and distal to Fan #2.. 52

Figure 11: A) Portion of CTX image P20_008929_2143_XN_34N342W showing large-scale morphology of Fan #2. Boxes show locations of images in Figure 12; B) Topographic profile of inlet valley terminating in Fan #2 (location not shown in Figure 11A); C)

Topographic profile of Fan #2. 53

Figure 12: Small scale morphologies on/near Fan #2. A) Sinuous-ridge features on surface of deposit superposed deposit; B) sub-horizontal planar features exposed on fan scarp, and pitted terrain on fan surface; C) steeply dipping features on fan scarp; D) previously hypothesized glacial terrain in the fan inlet valley resembling terrestrial rock glacier morphologies, including lineated valley fills, lobate debris aprons, and pitted textures; E) curvilinear ridge features on the floor of Fan #2 inlet valley. 55

Figure 13: A) HRSC grayscale image of Fan #21 with CRISM phyllosilicate summary parameters (R: DB2300, G: 2210, B: BD1900) overlain showing locations of phyllosilicates. Red/magenta regions represent locations containing Fe/Mg-phyllosilicates; inset shows Fan #21 with no CRISM overlay. B) Regional context of Fan #21 (HRSC visible data on THEMIS day-time IR basemap) with CRISM data (showing phyllosilicate summary parameters) overlain; dashed line shows approximate boundaries of watershed and solid line traces out inlet valley from watershed to deposit. C) and D) Phyllosilicate summary parameters overlain on grayscale CRISM data (FRT17CCB and FRTB001, respectively) in the watershed. E) CRISM visible-wavelength summary parameters of oxidized iron minerals (R: BD530, G: SH600, B: BDI1000) for data on Fan #21; areas abundant in dust appear orange-yellow (data stretch same as Figure 3C). F) CRISM summary parameters highlighting diversity in mafic minerals (R: OLINDEX, G: LCPINDEX, B: HCPINDEX) for data over Fan #21; green and blue regions show differences between spatial locations of low- and high-calcium pyroxene, respectively. 56

Figure 14: A) CRISM ratio spectrum of Fe/Mg-phyllosilicates in the lower beds and upstream watershed of Fan #21. Absorption features are most consistent of an Fe/Mg-smectite, likely nontronite and/or saponite. B) Library reflectance spectra of nontronite and saponite for comparison. C) Spectra on and distal to Fan #21 displaying absorption features consistent with low- and high-calcium pyroxene. D) Library spectra of pyroxene for comparison. ... 60

Figure 15: A) Portion of HRSC image H1982_0000 over Fan #21 with 100m elevation contours. White line shows location of topographic profile in B). C) & D) are portions of HiRISE image ESP_19975_1750 showing exposed layered variations in tonality in high albedo phyllosilicate-bearing regions of the fan scarp. 61

Figure 16: A) CRISM phyllosilicate summary parameters (R: DB2300, G: 2210, B: BD1900) of images in crater containing Fan #25 overlain on HRSC image H4340_0009_ND4. Red/magenta regions in CRISM parameters represent locations containing Fe/Mg-phyllosilicates. White line shows location of topographic profile through crater from inlet valley to outlet valley, and yellow outlined CRISM image shows location of B). B) CRISM phyllosilicate summary parameters overlain on grayscale of image FRT944A showing phyllosilicate-bearing regions (red/magenta) on Fan #25 and in small elongate depression ("ED") superposed on southern fan surface. C) CRISM summary parameters highlighting diversity in mafic minerals (R: OLINDEX, G: LCPINDEX, B: HCPINDEX) for data in the crater. D) CRISM visible-wavelength summary parameters of oxidized iron minerals (R: BD530, G: SH600, B: BDI1000) for data in crater containing Fan #25 (data stretch same as Figure 3C). E) Topographic profile through crater containing Fan #25, showing a relatively

flat floored crater that has likely been filled in with sediment. 64

Figure 17: A) CRISM ratio spectrum of Fe/Mg-phyllosilicates on/near Fan #25. Absorption features are most consistent of an Fe/Mg-smectite, perhaps saponite and/or vermiculite. B) Library reflectance spectra of saponite and vermiculite for comparison. C)Spectra on Fan #25 displaying absorption features consistent with low- and high-calcium pyroxene (blue and green, respectively). D) Library spectra of pyroxene for comparison. 67

Figure 18: A) Portion of CTX image P15_006798_1405_XI_39S103W showing morphology of Fan #25. Boxes show locations of images in Figure 19. B) Topographic profile of Fan #25 showing relatively flat sloping top bottom regions, and a relatively steep scarp. 68

Figure 19: Portions of HiRISE image PSP_006798_1405 showing small scale morphologies on/near Fan #25. A) Possible layering on exposed fan scarp; B) polygonal fractured terrain (“PFT”) in distal fan region. 69

Figure 20: CTX mosaic showing large scale morphology of Fan #22. Green “bowtie” shape shows location of CRISM image associated with this feature; yellow boxes show zoomed in areas in Figure 21 (base image courtesy of Lefort *et al.*, 2011). 70

Figure 21: CTX images showing small scale features on/near Fan #22. A) Exposed layers in a small trough between sinuous ridge features (and N-S oriented yardangs between ridges); B) Layering exposed in distal portions of, and between sinuous ridge features, and C), D), & E) show close-up figures of areas yellow boxed in B). North is toward top for all images (images courtesy of Lefort *et al.*, 2011)... 71

Figure 22: CRISM image near Fan #22; A) Default RGB composite of FRT000063A8 (arrow points to sand dunes between knobs and black boxes show locations of HiRISE images in Figure 24), and B) Phyllosilicate summary parameters (R: DB2300, G: 2210, B: BD1900) overlain on grayscale CRISM image showing the presence of phyllosilicates (red/magenta regions) on and distal to two semi-parallel, curvilinear, elongate knobs ~60 km south of Fan #22. C) CRISM visible-wavelength summary parameters of oxidized iron minerals (R: BD530, G: SH600, B: BDI1000) for this image; areas abundant in dust appear orange-yellow (data stretch same as Figure 3C). D) CRISM summary parameters highlighting diversity in mafic minerals (R: OLINDEX, G: LCPINDEX, B: HCPINDEX) for this image. 74

Figure 23: Spectra of hydrated minerals identified in CRISM image FRT000063A8, near Fan #22. A) CRISM Ratio spectrum of Fe/Mg-phyllosilicate-bearing regions in image FRT 0006A38, ~60 Km south of Fan #22. B) Library reflectance spectra of nontronite, saponite, and vermiculite for comparison. 75

Figure 24: Portions of HiRISE image PSP_004125_1720 showing A) Layered, and B) fractured terrain associated with phyllosilicate-bearing regions in CRISM image FRT63A8 near Fan #22... 76

Figure 25: A) CTX mosaic of large unnamed crater (containing Fan #19) and smaller, superposing crater that contains Fan #19 Distal Deposit. White box shows location of Figure 26A. Blue bowtie-shaped outlines show CRISM footprints, and yellow bowtie-shaped outline shows footprint of CRISM image FRT1B8E1, where phyllosilicates were

identified (Figure 27). Cyan rectangular strip shows location of CRISM multispectral image MSP0000821E_03 in Figure 29. North is toward the top of figure. 77

Figure 26: A) CTX mosaic of small crater containing Fan #19 Distal Deposit. Solid red line shows location of topographic profile, and dashed white arrows show examples inferred flow features, pointing in direction of flow. B) MOLA 128 ppd topographic profile over deposit, revealing steep slopes near the apex and shallow slopes in the distal regions of the deposit; blue line shows location of kink in the profile line. C) Portion of HiRISE image PSP_001754_1520 showing small scale morphologies on the deposit surface, including blocky textures, curvilinear ridge features (R), smooth intra-ridge regions (S), and boulder-sized clast inclusions entrained within and eroding from ridges (*e.g.,* white arrows). North is toward top of figures. 78

Figure 27: A) Default RGB composite of portion of CRISM FRT 0001B8E1, and B) CRISM phyllosilicate summary parameters (R: DB2300, G: 2210, B: BD1900) overlain on grayscale image, showing locations of phyllosilicate detections (red/magenta). Shadows/sharp brightness boundaries associated with ridge features in this image may cause detector artifacts in phyllosilicate summary parameters, therefore phyllosilicate spectra were taken from relatively flat –lying areas in this image. C) CRISM visible-wavelength summary parameters of oxidized iron minerals (R: BD530, G: SH600, B: BDI1000) for this image (data stretch same as Figure 3C). 80

Figure 28: A) CRISM Ratio spectra of phyllosilicate-bearing region in image FRT 0001B8E1 on Fan #19 Distal Deposit. B) Library reflectance spectra of possible phyllosilicate mineral matches, saponite and vermiculite. 81

Figure 29: Portion of CRISM multispectral image MSP0000821E_03 over Fan #19 Distal Deposit, the containing crater, and larger adjacent crater (location shown in Figure 26A). A) Default RGB composite, B) Phyllosilicate summary parameter (R: DB2300, G: 2210, B: BD1900) overlain on grayscale image, showing widespread phyllosilicate detections (red/magenta colors) on the deposit and on the floors of both craters. 82

Figure 30: Simplified hypothetical block diagram of the internal structure of an intracrater Gilbert-type delta on Mars, based on terrestrial facies models and analogues (*e.g.,* White, 1992). Diagram shows a Gilbert-type delta that has built out over a subaqueous fan core (lobate deposits). The basal lobes accumulate vertically until reaching the mouth of the inlet valley, at which time delta formation and progradation begins. Internal structure of delta shows shallow-dipping topset beds, steeply-dipping foreset beds, and shallow-dipping bottomset beds. Grayscale surface image is HiRISE and CRISM data of Fan #26 overlain on HRSC DTM (2X vertical exaggeration). 83

MASTERS THESIS

1. Introduction

Aqueous deposits on Mars are of particular interest to studies interpreting the Martian paleo-environment. When identified as bearing hydrated minerals and morphologies associated with formation in an aqueous environment, these features suggest fluvio-lacustrine processes in these regions of Mars, which are not observed on Mars under current environmental conditions.

The purpose of this study is to build on previous morphology-based identifications of hypothesized deltas on Mars, in order to assess the hypothesis that the paleo-climate of Mars once fostered periods of aqueous activity that allowed for sustained standing and flowing water on the surface. This goal is accomplished by performing multiple case studies of numerous globally-distributed hypothesized deltaic environments and fan-shaped deposits on Mars, concurrently interpreting the mineralogy, morphology, and thermophysical properties of the deposits. Twenty-six deposits were included in this study, selected from a compilation of putative deltaic deposits by Irwin *et al.* (2005). Areas bearing hydrated minerals on or near the deposits were analyzed in further detail based on morphology and thermophysical properties. I have used these results to interpret local geologic histories and past environmental conditions at the time and location of formation the deposits.

2. Geologic Background

2.1. Significance of the Identification of Deltas on Mars

Deltas are sedimentary features that form when flowing water confined in a fluvial channel deposits sediment upon entering a standing body of water. Therefore, the identification of deltas on Mars would imply a climate and depositional environment that facilitated the presence of standing and flowing water on the Martian surface, providing insight into the climatic history of Mars at the time of formation. Additionally, because the hypothesized deltaic features analyzed in this study are believed to have formed during the late Noachian and/or early Hesperian time periods (Dohm *et al.*, 2001; Mangold and Ansan, 2005; Irwin *et al.*, 2005; Dehouk *et al*., 2010), and because the present Martian environment cannot support liquid surficial water (due to the low surface temperature and atmospheric pressure), the identification of past Martian environments capable of sustaining standing and flowing liquid water would tell of the evolution of the Martian climate over time.

2.2. Significance of Hydrated Minerals on Mars

Hydrated minerals, such as phyllosilicates, carbonates, and sulfates, are significant because they form in the presence of liquid water via chemical weathering, alteration, precipitation, and/or hydrothermal and diagenetic processes. Because of this, the identification of these minerals implies the presence of liquid water at the time and location of mineral formation (whether formed *in situ,* at the location of each deposit, or formed elsewhere and subsequently eroded, transported, and redeposited in the deposit beds). Additionally, the identification of hydrated minerals suggests a local and/or regional wet period at the time and location of mineral formation, and may suggest fluvio-lacustrine processes in the transport or formation of the minerals.

2.3. Previous Studies of Possible Deltaic Deposits on Mars

Even in low resolution Viking images, fan-shaped features are observable on the Martian surface (Grant and Schultz, 1993; Cabrol and Grin, 1999). Improved spatial and spectral resolutions of modern remote sensing instrumentation allow the Martian surface to be studied in more detail.

Multiple studies have investigated the morphology, distribution, age, and formation mechanisms of sedimentary deposits on Mars (*e.g*., Grant and Schultz, 1993; Cabrol and Grin, 1999; Ori et *al*., 2000; Moore and Howard, 2005). Irwin *et al.* (2005) compiled a list of 33 deposits hypothesized (mostly by previous authors) to have formed in open-basin lakes on Mars (*i.e.*, hypothesized to be deltas) (Figure 1). That study was primarily limited to positive relief, fan-shaped features with frontal scarps occurring at the terminal ends of valleys that incise crater walls. The deposits are divided into three categories based on the presence or absence of distributary channels and stepped scarps on the deposit toe. In an attempt to exclude hypothesized alluvial fans that do not suggest base level control by a lake in the receiving basin, Irwin *et al.* (2005) did not include deposits with distal toes concordant with their respective crater floors.

Many possible deltaic deposits have been further studied using new data from higher-resolution instruments such as the Compact Reconnaissance Imaging Spectrometer for Mars (CRISM) and the High Resolution Imaging Science Experiment (HiRISE) on the Mars Reconnaissance Orbiter (MRO) spacecraft. Specifically, some of the 33 deposits characterized by Irwin *et al.* (2005) have been studied in great morphologic and mineralogic detail, the most well studied of which are located in Holden, Eberswalde, Jezero, and Gale craters (Malin and Edgett, 2003; Milliken *et al*., 2007; Ehlmann *et al.*, 2008; Grant *et al.*, 2008; Murchie *et al.*, 2009a). These studies found that basal portions of the deposits display strong spectral signatures of Fe/Mg phyllosilicates and exhibit morphologies consistent with formation in an aqueous environment, such as sub-horizontal bedding and/or polygonal fracturing (Murchie *et al.*, 2009a; Grant *et al.*, 2008), suggesting aqueous processes in the formation of the deposits.

3. Data and Methods

3.1. Data

Three primary data sets were used to address the science goals of this study. Data from CRISM were used to determine the mineralogical composition of the surface, data from HiRISE were used to analyze the morphology of the deposits and to look for small scale morphologies, and data from the Thermal Emission Imaging System (THEMIS) were used to analyze thermophysical properties (*e.g.*, thermal inertia) of the studied deposits. These datasets, along with additional supplemental data, are discussed below, and information regarding specific data used for each deposit studied is provided in Table 1**.**

3.1.1. Compact Reconnaissance Imaging Spectrometer for Mars (CRISM)

CRISM is a visible-infrared imaging reflectance spectrometer onboard the MRO spacecraft, covering wavelengths from 0.362 to 3.92 microns (362 to 3920 nanometers). CRISM targeted data utilize 544 wavelengths at a spectral resolution of 6.55 nm/channel, and a spatial resolution of ~18-36 meters/pixel (Murchie *et al.*, 2007). CRISM multispectral data utilize 72 selected wavelengths at a spatial resolution of 100 or 200 meters/pixel. CRISM targeted data were primarily used in this study, but multispectral data were also used for one deposit. CRISM data were used to look for hydrated minerals, such as phyllosilicates, and to inventory other minerals present in phyllosilicate-bearing deposits. These data were processed and analyzed using IDL/ENVI© and the CRISM Analysis Toolkit (CAT) (Murchie et *al.,*2007).

3.1.2. High Resolution Imaging Science Experiment (HiRISE)

HiRISE is a narrow-angle, visible-wavelength imaging system onboard MRO. It provides images of the surface of Mars at resolutions as high as 25 cm/pixel (McEwen *et al.*, 2007). Data from HiRISE were used to analyze the morphology of the deposits and surrounding areas. Specifically, HiRISE data were used to identify small scale aqueous features, such as horizontal bedding and polygonal fracturing. HiRISE data were analyzed using IAS Viewer©, ArcGIS, and/or the Java Mission-planning and Analysis for Remote Sensing (JMars) software program.

3.1.3. Thermal Emission Imaging System (THEMIS)

The THEMIS instrument, onboard the Mars Odyssey spacecraft, has five visible/near-infrared bands (centered from 0.42 to 0.86 μm) and nine multispectral thermal infrared bands (centered from 6.8 to 14.9 μm) (Christensen *et al.*, 2004). THEMIS night-time thermal infrared images have a resolution of 100 m/pixel and were used to measure effective night-time surface temperatures, from which thermophysical properties (*e.g.,* thermal inertias) of the deposits and their proximal areas were inferred. These data were then used to speculate about variations in clast/sediment sizes, textures, and/or induration. THEMIS data were processed using Arizona State University's THEMIS Processing Web Interface (THMPROC), which radiometrically calibrated the data, removed systematic noise, stray light, and signal drift, geometrically projected the data, and finally, removed band correlated noise and corrected the radiance. Quantitative thermal inertia values of the resulting THEMIS image cubes were then calculated using jENVI, a THEMIS add-on program within the ENVI/IDL software package. A THEMIS day-time infrared base map (100 m/pixel resolution) was used for regional context in some regions.

3.1.4. Context Camera (CTX)

The Context Camera (CTX) on MRO provides grayscale visible-wavelength images of the Martian surface at a resolution of 6 m/pixel, with image swaths ~30 km wide (Malin *et al.*, 2007). Data from CTX provide large-scale contextual information of the morphologies of the deposits and their surrounding areas.

3.1.5. High Resolution Stereo Camera (HRSC)

High Resolution Stereo Camera (HRSC) visible and topographic data where available were used for context and elevation for deposits in this study (Table 1). HRSC is a multi-sensor push-broom scanner with nine CCD line sensors mounted in parallel, having 5,184 pixels/line. Five of the nine sensors are centered at 650±90 nm (full width at half-maximum): one nadir channel, two stereo channels (forward and backward looking at +/- 18.91˚), and two photometric channels. HRSC also has four color channels in the visible and near-infrared (NIR) wavelengths (blue, 440±45 nm; green, 530±45 nm; red, 750±45 nm; and NIR, 970±45 nm). Images from the instrument have a spatial resolution of 10 m/pixel and an image swath width of 53 km at the closest approach altitude of 250 km. Digital terrain models (DTMs) derived from HRSC stereo data were used to evaluate the topography of the deposits and surrounding areas, where available. The topographic information was used to determine slopes, and to create topographic profiles of deposits in this study. HRSC DTMs have grid sizes of up to 50 m, and a single pixel has vertical accuracy of up to 10 m. Analyses using HRSC data were done in ArcGIS©, a geographic information system (GIS) software product.

3.1.6. Mars Orbiter Laser Altimeter (MOLA)

Data from the Mars Orbiter Laser Altimeter (MOLA) (Smith *et al.*, 1999), on the Mars Global Surveyor (MGS) spacecraft were used to determine elevations of the deposits and surrounding areas where higher resolution topographic data were not available, and were specifically used to evaluate slopes and generate topographic profiles. Data from MOLA are available in two formats: individual "single track" MOLA data and gridded MOLA data, which are interpolated from the single track data. The vertical shot-to-shot precision of single track MOLA data is 37.5 centimeters and the absolute vertical accuracy is less than ten meters; the surface spot size is 130 meters, the along track spacing approximately 330 meters, and the cross track spacing is variable and dependent upon latitude (as large as several kilometers at lower latitudes, and generally decreasing with increasing latitude) (Smith et *al.*, 1999). MOLA gridded data have been produced at resolutions of 4, 16, 32, 64, and 128 pixels per degree, ranging between ~0.5 km/pixel (128 pixels/degree) and ~15 km/pixel (4 pixels/degree). Analyses of MOLA data were done using ArcGIS© and/or the Java Mission-planning and Analysis for Remote Sensing (JMARS) Program.

3.2. Data Analysis

3.2.1. Dataset Limitations and Data Availability

Due to availability of data, the limiting dataset in this study was CRISM. Because CRISM measures reflected radiance of only the top few microns of the Martian surface, the observed surface must be relatively free of any mantling of aeolian dust deposits that would obscure the spectral character of the underlying surface. The large amount of surface dust cover in many regions of Mars prevents CRISM from obtaining useful data for many of the deposits considered for inclusion in this study.

High resolution CRISM targeted data were available on or proximal to thirty-one of the thirty-three deposits of interest, and lower resolution CRISM multispectral data were available for remaining deposits of interest. Because of the opacity of atmospheric and/or surface dust, not all of the acquired CRISM targeted images provided significant mineralogic information.

3.2.2. Determination of Deposits to Include in this Study

As discussed in section 2.3., deposits located in Holden, Jezero, Eberswalde, and Gale craters have been studied previously in great morphologic and mineralogic detail (Malin and

Edgett, 2003; Milliken *et al*., 2007; Ehlmann *et al.*, 2008; Grant *et al.*, 2008; Murchie *et al.*, 2009a). Due to the extensive analyses of these deposits by others, sedimentary deposits located in Holden, Jezero, Eberswalde, and Gale craters were not included in this study (*i.e.*, Fans #9, 10, 12, 17, 18, 23, and 24, as named by Irwin *et al.*, 2005 were excluded).

My study focused on six deposits (five of which were in the original 33 discussed by Irwin *et al.* (2005)) in detail, based on the identification of hydrated minerals in association with these deposits. Information regarding the physical characteristics and locations of these deposits is provided in Table 2.

3.2.3. Analysis Techniques and Final Products

Work by Irwin *et al.* (2005) describing 33 hypothesized deltas was chosen as a basis for my study because it presents a detailed compilation of Martian deposits that were previously hypothesized as deltas. The data pool was then further reduced by using CRISM to search for hydrated minerals on/near these deposits. Deposits that were found to bear hydrated minerals were further characterized based on small-scale morphology and thermophysical properties (*e.g.*, thermal inertia). These characterizations were then used to interpret the geologic history and depositional environment at the time of formation the deposits.

There are multiple possible processes that could be responsible for the formation of the deposits, including deltaic, alluvial, glacial, mass wasting, and/or volcanic flow processes. In this study the deposits are referred to as “fans”, in keeping with the naming convention of Irwin *et al.* (2005); these names are descriptive of the shapes of the deposits and do not necessarily carry an environmental or formational connotation. To objectively test the deltaic hypothesis (as has been proposed for most of these deposits), multiple possible hypotheses for the formation of each of the deposits have been concurrently considered in the evaluation of formational processes. Table 3 shows multiple possible formational processes in comparison with observable/measureable characteristics.

CRISM data were used to search for hydrated minerals on and/or distal to the studied deposits within the possible lake basins. Initially, CRISM version TRR2 data were used to look for hydrated minerals in association with these deposits. When higher quality version TRR3 data were made available by the CRISM team (Seelos *et al.*, 2011), all new data and older data of deposits that were previously found to definitely (or possibly) bear phyllosilicates were processed (or re-processed) using the newer TRR3 data. The most significant change to this newer version of CRISM data is a correction for “slight shutter/mirror position non-repeatability when viewing an internal calibration reference (integrating sphere)” (Seelos *et al.*, 2011); among many other improvements, the results of this correction improve the agreement of CRISM VNIR (visible-near infrared) and IR (infrared) data at ~1.0 µm, as well as improving the “consistency of the recovered surface spectral reflectance for repeat observations” (Seelos *et al.*, 2011).

The raw CRISM data were processed by applying atmospheric and photometric corrections to remove these effects; the data were then “destriped” and “despiked” (TRR2 only) to remove instrument artifacts, thereby improving the quality of the data. Corrected CRISM data were then used to create spectral summary parameters (Pelkey *et al.*, 2007), which were useful in constraining the spatial locations to look for phyllosilicates, carbonates, and sulfates. Multiple regions of interest (ROIs) were created for each image using the ENVI ROI tool, and mean ROI spectra that displayed absorption features indicative of hydrated minerals were ratioed to a "spectrally bland" region within the same columns of the CRISM image. The mineralogically interesting and spectrally bland regions of interest contained approximately the same number of pixels. The purpose of doing spectral ratios is to cancel out systematic calibration artifacts to examine weaker spectral variations. Other minerals of interest were then inventoried near deposits found to bear hydrated minerals.

In addition to a mineralogic assessment of areas found to bear hydrated minerals, the deposits were characterized based on large and small scale morphology. One particular interest is the overall shape and slope of each deposit and inferred post depositional reworking, as this may be indicative of the dominant formation processes and depositional environment of the features. Also of interest is the presence or absence of small scale geologic features associated with formation in an aqueous environment (referred to in this study as "aqueous morphologies"). These features include, but are not limited to: vertical stratification of layers (*e.g.*, compositional and/or grain-size layering), sub-horizontal bedding, polygonal fracturing, large clast inclusions, and inlet valleys (Table 3). Some of these features (in particular, horizontal layering and polygonal fracturing) have been observed in phyllosilicate-bearing fan-shaped deposits elsewhere on Mars (Milliken *et al.*, 2007; Grant *et al.*, 2008; Murchie *et al.*, 2009a).

The importance of the presence of hydrated minerals and morphologies associated with aqueous processes is not restricted to the deposits themselves, but is also significant within the receiving basins and upstream watersheds. The presence of these morphologies and mineralogies in the basin may be indicative of a lacustrine environment at the time of fan deposition (suggesting deltaic processes), and the presence of hydrated minerals in an upstream watershed would suggest transport and redeposition (as opposed to *in situ* formation) of these minerals in the deposit.

Thermal inertia, which is a measure of the resistance of a material to changes in temperature, is estimated from diurnal temperature variations of a given surface, and is closely related to the physical nature of the surface (*e.g.* particle size and/ or induration). The thermal inertia of deposits found to bear hydrated minerals was estimated in order to infer possible variations in clast/sediment sizes, textures, and/or induration, and to compare these variations between deposits. THEMIS night-time thermal infrared data were used to estimate thermal inertia, as these data reduce the effects of albedo and topography associated with thermal inertia calculation using day-time IR data. Warm areas in night-time infrared imagery correspond with areas of higher thermal inertia, indicating a coarse-grained, blocky, or well-indurated surface; conversely, cool areas correspond to areas of low thermal inertias (*e.g.*, Kieffer *et al.*, 1977).

Lastly, topographic data were used to determine the three dimensional morphologies of deposits bearing hydrated minerals and their surrounding areas (*e.g.*, creating topographic profiles). The primary topographic data used were HRSC DTMs due to their availability and high spatial resolution. CRISM measurements of hydrated mineral-bearing deposits were overlain on HRSC DTMs to constrain the three dimensional locations of hydrated minerals with respect to the deposits. Gridded MOLA data were used in lieu of HRSC topographic data for some of deposits.

3.2.4. Possible Depositional/Formational Mechanisms for Hydrated Minerals

Hydrated minerals are formed by the alteration of rock in the presence of liquid water, or by the precipitation of chemicals from water solutions (*e.g.*, evaporites). The hydrated minerals identified in association with the deposits in this study may have formed authigenically (*i.e., in situ*) within the hypothesized paleolakes, or allogenically, having formed elsewhere on Mars and been later eroded, transported, and redeposited in the beds of the deposits. The presence of spectrally similar hydrated minerals in the beds of, and upstream of a deposit (*e.g.*, in the inlet valley and/or watershed) is highly suggestive of the latter depositional process.

McKeown *et al.* (2009) propose multiple alternatives for the formation/deposition of phyllosilicates (Al- and Fe/Mg-phyllosilicates) in the Mawrth Vallis region on Mars, including the alteration of basaltic ashfall (similar to terrestrial bentonites), sedimentary deposition in a marine or lacustrine environment, and pedogenesis (*i.e.*, soil formation) of basaltic rocks. McKeown *et al.* (2009) also address possible implications for the water sources and past Martian climates associated with each of these processes. For example, possible water sources for phyllosilicate formation via basaltic ashfall processes include groundwater, marine, and/or lacustrine sources, and would suggest a climate of active volcanism; sedimentary deposition into a marine/lacustrine basin could suggest a warm/wet climate with ongoing hydrolysis (and possible seasonal dry periods); and formation via pedogenesis is suggestive of precipitation and a warm/wet climate, as described above. These formational/depositional mechanisms of phyllosilicates and their likeliness in explaining the presence of phyllosilicates in association with these deposits are further discussed in section 4 (with particular emphasis in sections 4.1.2. and 5.2.).

4. Observations and Interpretations

Hydrated minerals (*e.g.,* phyllosilicates, carbonates, and sulfates) were sought in all of the deposits studied, and some of these minerals were positively identified in association with six of the deposits. Fe/Mg-phyllosilicates are the most prevalent type of mineral identified, present at all six of the hydrated mineral-bearing deposits. Al-phyllosilicates (possibly mixed with hydrated silica) are also present in the beds of at least one of the six deposits,. Small-scale morphologies consistent with formation via aqueous processes are also present in association with the deposits, and trends in thermal inertia (such as relatively high thermal inertia values, suggesting induration) are predominantly correlated with phyllosilicate-bearing regions.

4.1. Fan #26

4.1.1. Mineralogy and Morphology

Fan #26 is located in the Nepenthes Mensae region of Mars (Figure 1). In addition to this fan-shaped deposit described by Irwin *et al.* (2005), there is an older depositional feature that lies stratigraphically below Fan #26 (Figure 2); both deposits were previously hypothesized to be deltas by de Pablo and Pacifici (2008).

Fe/Mg-phyllosilicates were initially identified on an elevated knob distal to this deposit (Hughes *et al.*, 2010), and Al-phyllosilicates were later identified surrounding the Fe/Mg-phyllosilicate-bearing knob and in distal beds of the fan (Figure 3A) (Hughes *et al.*, 2011). From the top of the elevated knob to the bottom, the depth of the absorption feature associated specifically with Fe/Mg-phyllosilicates (~2.3 μm) decreases and the depth of the feature associated with Al-phyllosilicates (~2.2 μm) increases, suggesting a decrease in Fe/Mg phyllosilicates, and an increase in Al-phyllosilicates with decreasing elevation on the knob (Figure **4**A).

Spectrally similar Fe/Mg- and Al-phyllosilicates are present in the lower beds of Fan #26 and the older, superposed deposit that is stratigraphically below Fan #26. Fe/Mg-phyllosilicates in the lower fan beds, and on the distal knob display absorption features at ~1.4, ~1.9, and ~2.3 μm, indicative of an Fe/Mg-smectite, perhaps nontronite (an Fe-rich phyllosilicate with key absorptions at 1.42, 1.91, and 2.28-2.29 μm) and/or saponite (a Mg-rich phyllosilicate with key absorptions at 1.39, 1.91, and 2.30-2.31 μm). Because the ~2.3 μm feature of spectra of some Fe/Mg-phyllosilicates in this region has a double absorption at 2.29 μm and 2.30 μm (with a deeper absorption feature at 2.29 μm), it is possible that these phyllosilicates are composed of both nontronite and saponite, or nontronite with some Mg replacement (*e.g.*, McKeown *et al*., 2009). The latter possibility may be more likely, given the presence of additional absorption features near ~2.4 and ~2.5 μm (unique to some nontronites) in numerous ratioed CRISM spectra of Fe/Mg phyllosilicates in this area.

The Al-phyllosilicates in the lower beds of the superposed deposit display absorption features at ~1.4, ~1.9, and ~2.2 μm, indicative of an Al-smectite, most consistent with montmorillonite (Figure **4**A & C). The ~2.2 μm absorption feature is broader than the typically sharp Al-OH absorption at 2.21 μm observed in montmorillonite library spectra, suggesting that these phyllosilicates may be mixed with another mineral such as hydrated silica (*e.g.*, opal), which has a broad absorption feature at 2.21 μm (McKeown *et al.*, 2009) (Figure **4**C). The Al-phyllosilicates at the base of the elevated knob distal to the fan are spectrally similar to those identified near the fan toe. The Al-phyllosilicate unit near the fan toe of the older superposed deposit lies topographically between two other units which contain Fe/Mg-phyllosilicates.

Fe/Mg- and Al-smectites are also present (though spectra are more noisy and likely mixed with pyroxene) within the inlet valley and watershed upstream of these deposits (Figure 2 inset, Figure 3B, and Figure **4**B). Fe/Mg-smectites are also present within a large, elevated, elongate feature with a central depression near the fan toe (Figure 2 and Figure 3A), which has been previously hypothesized as an underwater fissure volcano (de Pablo and Pacifici, 2008) based on the morphology and location of the feature, as well as inferred tectonic influences in the region. Fe/Mg phyllosilicates are widespread in this region, present in CRISM targeted data as far away as 50 and 100 km from these deposits.

Visible-wavelength CRISM data reveal that the surface of Fan #26 is mantled with dust (Figure 3C), possibly muting underlying spectral absorption features on this deposit. Distal fan beds and portions of the elevated knobs that display spectral features consistent with phyllosilicates are not mantled with dust. Pyroxene-rich sand dunes (which postdate the formation of the deposits) mantle portions of the lower beds of the deposits (Figure 3D and Figure 4D & E). A ~1.9 μm absorption feature (associated with hydration) is present in some ratio spectra of sand dunes covering distal portions of the deposits near phyllosilicate identifications (Figure 4D & E), suggesting that the dunes mantle a more extensive phyllosilicate-bearing lithology than what is currently observable.

Both Fan #26 and the superposed deposit exhibit vertically stratified layers in their lower beds, inferred from layered albedo variations, and apparent variations in material strength of the rock layers (possibly indicating compositional layering or differences in grain sizes) (Figure 6A, B, & C). Additionally, polygonal fractured terrain is observable near the fan toe (Figure 6D), and large (HiRISE- resolvable) boulder-sized clast inclusions are apparent in lower beds of the fan (Figure 6E); these respectively suggest desiccation processes, and a high sediment and/or water flux in the formation of the fans (which would have transported boulder-sized clasts to distal fan regions). Many concentric ring features are present on the top surface of the fan, with fine-scale layering exposed between concentric features (Figure 6F), suggesting that the features represent layered beds created by the consecutive deposition of sediment during fan formation. These observable layers, as well as degraded craters on the top surface of the fan suggest that post-depositional erosion of the fan surface has occurred. Heavily eroded, radially oriented gullies are also present on the top surface of, and distal to Fan #26, possibly representing eroded fan distributary channels (Figure 5 and Figure 6G).

Parallel linear features perpendicularly cross-cut the slope direction of the scarp of Fan #26; they are observable in many distal regions of Fan #26 and the superposed deposit (Figure 6G), with a particularly large exposure on the southeast scarp of Fan #26 (Figure 6H). Based on the observations that these features are parallel with each other, and located perpendicular to the slope direction on the fan scarp, it is inferred that these features represent depositional layers exposed by preferential erosion of the scarp; these features are interpreted as being formationally linked with each other, based on geomorphic similarities and their exposure on the scarp and in lower beds of the deposits.

Another region of lineated features is present on the southern scarp of Fan #26 (Figure 6I). These features are oriented in a similar direction as the aforementioned linear features, but the larger size, differing morphology, and diagonally cross-cutting relationship with the fan scarp suggest that these features on the southern fan scarp are not genetically linked to other observed lineated features associated with the deposits. The features on the southern scarp may have been formed by slope failures, aeolian deposition, or other processes.

The main inlet valley terminating in these deposits is at least 40km long, with a sinuosity (*i.e.*, ratio of actual path length over shortest path length) of 1.15 and an overall gradient of 1.6˚. The valley carves out a steep-walled canyon before forming the deposits at the valley mouth (Figure 2). De Pablo and Pacifici (2008) interpret multiple flat-topped stepped deposits within the valley as fluvial terraces (Figure 2). A smaller tributary channel (~33km long) feeds into the main valley near the apex of the deposits (Figure 2). The main inlet channel of the deposits cannot be traced with certainty more than 40 km upstream of the fan apex, where multiple channels converge in a relatively flat-lying, degraded tributary system.

The top-most beds of Fan #26 are shallow sloping, with slopes between 0.9-1.5˚, and the frontal scarp of this deposit has a relatively steep slope ranging between 11-19˚ (Figure 5B). The slopes of this scarp appear to have been reworked by aeolian processes and post-depositional and/or mass wasting events, suggesting that the average slope determined is likely less steep than that of the original scarp. The characteristic of shallow sloping "topset" beds (*i.e.*, the top-most surface) and relatively steeply sloping "foreset" beds (*i.e.*, the fan scarp) is consistent with morphologies of many terrestrial deltaic deposits, such as Gilbert-type deltas (Leeder, 1999).

Shallowly sloping "bottomset" beds (*i.e.*, beds distal to the fan scarp) are also consistent with terrestrial deltaic deposits. However, it is difficult to quantify the slopes of the lower beds of Fan #26 because they superpose another deposit. The slopes of the lower deposit are much less steep than those of Fan #26, ranging between 6.5-9˚.

4.1.2. Possible Depositional/Formational Mechanisms for Phyllosilicates

It is likely that a combination of authigenic (*i.e.*, *in situ*) and allogenic (*e.g.*, erosion, transport, and re-deposition) formation is responsible for the presence and mineralogic diversity of phyllosilicates in/near these deposits. The identification of Fe/Mg- and Al-phyllosilicates in the drainage basin upstream of the deposits (Figure 2 inset and Figure 3B) suggests transport and redeposition of at least some of the phyllosilicates. Fe/Mg– and Al-phyllosilicates may have formed via the alteration of two distinct parent lithologies with differing compositions, or by the successive alteration of Fe/Mg-phyllosilicates to Al-phyllosilicates in the sustained presence of liquid water. Due to the distinct spatial, stratigraphic, and topographic locations of Fe/Mg- and Al-phyllosilicates in the beds of, and distal to the fan deposits, it is inferred that these phyllosilicates were formed at different times and/or by different processes.

The detection of Fe/Mg phyllosilicates on the top of the distal elevated knob, and Al-phyllosilicates at the base of the knob could imply either authigenic formation or transport and deposition of phyllosilicates via fluvial, aeolian and/or volcanic processes (perhaps transported down-slope from the outcrop of Al-phyllosilicates in the lower beds of the deposits). Authigenic formation or sub-aqueous sedimentary deposition are possible origins of Fe/Mg phyllosilicates on the elevated knob, based on the location of these phyllosilicates concentrated on the top and sides of the knob, and a lack of Fe/Mg-phyllosilicates directly surrounding the knob. Alternatively, the knob could represent an eroded portion of an originally more extensive sedimentary deposit.

If Fe/Mg-phyllosilicates on the knob were formed sub-aqueously *in situ*, this would suggest a minimum water depth of 800m and a minimum water surface elevation of -1950m in this area at the time of the formation (the relief and elevation of the knob, respectively). This elevation is in agreement with the elevation of the top surface of Fan #26, and therefore, may be consistent with a deltaic hypothesis if the formation of the fan occurred concurrently with the possible *in situ* formation of phyllosilicates on the knob.

Alternatively, phyllosilicates could have been transported and deposited on the knob post-formation of the sedimentary deposits. The location of Fe/Mg-phyllosilicates on the top of the knob suggests sub-aerial transport and redeposition, perhaps in a lacustrine/marine environment where the knob was partially submerged underwater and phyllosilicate deposition may have occurred on only exposed portions of the knob. However, aeolian transport of phyllosilicates would have also likely transported large amounts of dust and/or sand, and a large aeolian mantling is not apparent on the top of knob. For this reason, phyllosilicate deposition via aeolian transport is unlikely.

The identification of Fe/Mg-phyllosilicates in other areas in this region, and the presence of phyllosilicates in the center of an elongate fissure feature (previously hypothesized as a sub-aqueous volcano by de Pablo and Pacifici, 2008) distal to the deposits suggests that phyllosilicate-bearing volcanic ash may have been deposited in this area. The sub-aerial deposition of phyllosilicate-bearing volcanic ashfall on the top of the knob (without subsequent sub-aqueous alteration) is unlikely due to an abundance of phyllosilicates and lack of a volcanic ash mantling on the top of the knob. However, the deposition of volcanic ashfall into a lacustrine/marine environment (or sub-aerial deposition that was later submerged) could have subsequently altered into Al-phyllosilicates (similar to terrestrial bentonites) (McKeown *et al.*, 2009). Fe/Mg-phyllosilicates could also have formed from the alteration of an ashfall of a different composition, or volcanic glass entrained in ashfall or pyroclastics (McKeown *et al.*, 2009).

Any one (or combinations) of these depositional/formational mechanisms could be responsible for the presence of phyllosilicates in this area, but the data presently available do not uniquely constrain of the origin of phyllosilicates in this region.

4.1.3. Thermal Inertia

The thermal inertia on the top surface of Fan #26 is relatively low, ranging from ~200-300 J m^{-2} K^{-1} $s^{-1/2}$ (these units are assumed for all subsequent thermal inertia values provided) (Figure 7), likely due to a mantling of dust on the surface of this deposit (Figure 3C). A smaller fan-shaped lobe radiating to the north on the surface of the fan has a relatively higher thermal inertia, and may represent the most recently active depositional lobe of the fan that has not been covered by as much dust as other areas of the fan surface. Although the fan scarp has a consistent thermal inertia, this may include many errors because its slope (Fergason *et al.*, 2006). Phyllosilicate-bearing areas (both Fe/Mg- and Al-phyllosilicates) distal to the deposits display high thermal inertia values (~450-850) that are inferred to be caused by induration of fine-grained clay materials. This interpretation is consistent with previous interpretations by Jakosky (1986), who suggests that high thermal inertias (*e.g.*, greater than 400) may be due to induration. The inference of fine-grained materials in topographically lower areas and in distal regions of the deposits is consistent with the grain-size sorting typical of a lacustrine/deltaic environment (*e.g.*, Boggs, 1995). This pattern of higher thermal inertias that is concordant with many phyllosilicate-bearing areas may further suggest that Fan #26 (and/or the superposed deposit) was deposited in a standing body of water.

4.1.4. Interpretation of Depositional Environment

In summary, the abundance of morphologies associated with formation in an aqueous environment and the presence of phyllosilicates in the lower beds and distal areas of these deposits are consistent with deltaic processes in the formation of Fan #26, and of the older, superposed deposit. Although Fan #26 may resemble an alluvial fan in plan-view, the morphology of this deposit (particularly the slopes) is most consistent with that of a Gilbert-type delta, and a lack of distinct morphologic regions or breaks in slope on the top surface of the fan make it unlikely that Fan #26 is an alluvial fan-delta.

4.2. Fan #2

4.2.1. Background

Ismenius Cavus crater, the basin containing Fan #2, has been hypothesized to have hosted multiple different geologic environments, including fluvial, lacustrine, and glacial (Dehouck *et al*., 2010). Phyllosilicates were initially identified in the center of Ismenius Cavus crater by the OMEGA (Observatoire pour la Minéralogie, l'Eau, les Glaces et l'Activité) instrument team (Poulet *et al.*, 2005), in addition to an extensive pyroxene-bearing unit proximal to the phyllosilicate unit (Figure 8A).

Fan #2 was previously hypothesized to be a Gilbert-type delta (Dehouck *et al*., 2010) based on the presence of a steep sloping region interpreted as foreset beds (10-12˚) and a gently sloping region interpreted as topset beds (<1˚). The crater containing Fan #2 also contains two additional deposits that were not previously identified in lower resolution THEMIS and Viking data. One of the deposits (a large deposit at the mouth of Mamers Vallis in the southern portion of the crater) is hypothesized as a delta, and the other (a small deposit on the eastern rim of the crater) as an alluvial fan or alluvial fan-delta (Dehouck *et al*., 2010). All three of the deposits in this crater have a plateau surface at the same elevation (roughly -3100m), suggesting the simultaneous deltaic formation of these deposits in a lacustrine environment with a water level at this elevation (Dehouck *et al*., 2010).

The valley floor of Fan #2, and floors of other terminal valleys into this crater display lineated valley fills, lobate debris aprons, and pitted textures interpreted as glacial landforms by Dehouck *et al*. (2010) (*e.g.*, Squyres, 1978; Mustard *et al.*, 2001). Through crater counting and stratigraphic relationships, Dehouck *et al.* (2010) determine a Hesperian age (though with a significant amount of uncertainty) for the fluvial and lacustrine activity in Ismenius Cavus. They furthermore determine a late Amazonian (50-300 My) age for glacial landforms in the crater, establishing the formation of the fan deposits significantly before the superposition of glacial/periglacial landforms in inlet valleys and distal fan regions.

4.2.2. Mineralogy and Morphology

The phyllosilicate unit in the center of Ismenius Cavus crater displays extensive sub-horizontal layering and polygonal fractured terrain (Figure 8B) (Dehouck *et al*., 2010; Hughes *et al.*, 2010). These phyllosilicates, indicative of an Fe/Mg-smectite, display absorption features at ~1.4, ~1.9, and ~2.3 μm, consistent with nontronite, and/or saponite or vermiculite (Figure 9). CRISM data on/near Fan #2 display much lower signal-to-noise ratios than data in the center of the crater (Figure 10), but consistencies between locations of possible phyllosilicate detections in CRISM summary parameters and observable morphologic units suggest that phyllosilicates may also be present on and/or distal to Fan #2 (Figure 10).

The lack of overlap between locations of phyllosilicate and pyroxene detections in the center of the crater (Figure 8A) implies that these minerals exist in two separate lithologic units. Apart from these detections of phyllosilicate- and pyroxene-bearing units, no other unique spectral signatures are apparent on Fan #2 or within Ismenius Cavus crater. CRISM visible-wavelength spectral summary parameters show an extensive mantling of dust on the surface of Fan #2 and on the floor of Ismenius Cavus crater, with the exception of phyllosilicate and pyroxene outcrops in the center of the crater (Figure 8C). A mantling of surface dust would mute underlying spectral signatures, therefore suggesting that the units in the center of the crater are more extensive than what is presently observable.

Fan #2 is situated stratigraphically on top (and somewhat south) of another deposit that has previously been mapped as the same depositional feature (Figure 11A) (Irwin *et al.*, 2005; Dehouck *et al*., 2010). Superposition relationships and a less extensively eroded surface suggest that Fan #2 was formed in a separate depositional event after the formation of the northern, underlying deposit. A variety of curvilinear features of negative and positive relief are present on both of the fan surfaces, including a wide, radially oriented inlet valley (Figure 11A), and sinuous ridges on the surface of the superposed deposit (Figure 12A). The negative relief features extending from the inlet valley are inferred to be incised channels of the deposits and sinuous ridges are inferred to be inverted channels that may be eroded fan distributary channels (*e.g.*, Moore and Howard, 2005; Bhattacharya *et al.*, 2005).

These multiple episodes of deposition, as implied by the superposition of these two deposits may have either 1) been produced by a hiatus during which sediment was not being deposited, or 2) the younger deposit (Fan #2) may have formed as a result of a channel switching event (*i.e.,* channel avulsion), creating a second depositional lobe. The relatively wide and deeply incised inlet channel of Fan #2 suggests that sediment was deposited over a longer period of time, or that there was an increased amount of sediment deposited in this fan. The lack of sinuous features (of negative or positive relief) on the surface of Fan #2 suggests either differing flow regimes in the formation of these two deposits or different post-formation erosional environments.

Sub-horizontal layers of alternating tonality and varying resistance are exposed and traceable around the scarp (Figure 12B). These layers are interpreted as planar bedding exposed by post-formational erosion of the fan scarp. On the southern scarp of this fan, there is another region of parallel, linear features, but unlike the before-mentioned features, those on the southern scarp are steeply-dipping toward the center of the crater (Figure 12C). Although these features may display similarities to the steeply-dipping foreset beds of a delta (*e.g.* a Gilbert-type delta), it is unlikely that these features are associated with the depositional beds of the fan because they appear to cross-cut the before-mentioned sub-horizontal fan beds in some locations on the fan scarp, suggesting that these steeply-dipping features were formed by another process (*e.g.,* aeolian deposition) after formation of the fan.

A pitted terrain is visible on the surface of Fan #2 in HiRISE imagery (Figure 12D), and may represent a latitude-dependant texture that has been observed in mid- to high-latitudes on Mars (Mustard *et al.*, 2001; Dehouck *et al*., 2010). This terrain has been interpreted as a young (< 1 million years old), thin (<10 m) mantling of dust and ice, forming a pitted texture due to the sublimation of ice (Mustard *et al.*, 2001). The thickness of this terrain and spectrally bland nature of dust would obscure underlying mineralogies, possibly muting spectral signatures of phyllosilicates on the surface and in basal portions of Fan #2. The presence of this pitted terrain, which forms in terrestrial periglacial regions, is consistent with periglacial processes in this area.

The inlet valley of this fan originates from within a smaller crater east of Ismenius Cavus crater (Figure 8). A topographic profile of the inlet valley (Figure 11B) (location of profile not shown) shows a relatively steep gradient and an increase in elevation toward the crater rim followed by a decrease in elevation before entering Ismenius Cav

us crater. The valley, V-shaped in cross-section, excavates sediment within the smaller, relatively flat floored crater, suggesting infilling of this crater prior to valley formation. The amphitheater-shaped headwall and indistinct origin of the valley from within an upstream crater may be consistent with valley formation via groundwater sapping. Lineated valley fills within the inlet valley (Figure 12D) suggest post-formational creep commonly associated with rock glaciers (*i.e.*, viscous flowing rock fragments with interstitial ice) in terrestrial settings (Ritter *et al.*, 2002), and curvilinear features on the valley floor (Figure 12E) may be associated with fluvial and/or periglacial processes. The lack of an accumulation zone up-valley of these features suggests that the features may have been formed by a rock glacier, rather than a glacier.

A topographic profile of Fan #2 shows a relatively steep gradient at the apex of this deposit (Figure 11C), which is inconsistent with the morphology of terrestrial deltas (Blair and McPherson, 1994). This may suggest that this deposit is an alluvial fan-delta, having a subaerially formed alluvial fan upper portion and a subaqueously formed deltaic lower portion (*e.g.*, Blair and McPherson, 1994). Alternatively, as this deposit appears to have been modified by post-formational glacial/periglacial processes and gravity slope failures, the steep gradient near the apex may represent reworking of the fan surface. This latter possibility is considered more likely due to the apparent breaks in slope and distinguishable superposed units on the fan surface (Figure 11A).

Topographic contours and the location of phyllosilicates distal to the largest deposit in this crater suggest that the phyllosilicate-rich unit in the center of Ismenius Cavus crater may coincide with the lower beds of this deposit (consistent with the selective sorting of fine-grained sediment in the distal portions of a deltaic environment). Alternatively (or additionally), the phyllosilicate unit in the center of the crater could represent the selective sorting of fine-grained sediment in a lacustrine environment. Both of these hypotheses for the origin of phyllosilicates in the crater infer fluvial transport of sediment into a lacustrine environment, and hence, likely deltaic processes.

4.2.3. Thermal Inertia

The surface of Fan #2 and portions of the floor of Ismenius Cavus crater have relatively low thermal inertia values (between 150-220 on the fan surface) (Figure 7), consistent with a mantling of surface dust which is also observed in CRISM data (Figure 8C). The fan toe has slightly higher thermal inertia values between 200-250, but these numbers may be associated with errors in thermal inertia due to the slope of the scarp. As was the case with Fan 26, very high thermal inertias (400-850) are present in the center of the crater, coinciding with phyllosilicate-bearing units. This area may represent the distal portion of a larger deposit or lacustrine fines that were concentrated and later indurated in the center of the crater.

High thermal inertias in linear flow patterns radiating away from a larger inlet valley forming a deposit in the crater suggest that these materials may also bear phyllosilicates (though dusty CRISM data made it difficult to identify phyllosilicates in this area). This connection of high thermal inertia with indurated material (in this case, phyllosilicates), and the pattern of high thermal inertia values linearly radiating from a large inlet valley suggest that some (or all) phyllosilicates in this crater may have been transported, but does not preclude the possibility that some phyllosilicates may have formed *in situ*. The longevity of standing water in this crater would be difficult to constrain if the origin of phyllosilicates is strictly allogenic (transported).

4.2.4. Interpretation of Depositional Environment

The polygonal fracturing, horizontal bedding, and concentrations of phyllosilicates in the center of this crater support the previously proposed hypothesis that Ismenius Cavus Crater once contained standing liquid water, in which a delta might have formed (Irwin *et al.*, 2005; Dehouck *et al.*, 2010; Hughes *et al.*, 2010). The possible presence of phyllosilicates in association with Fan #2, slopes resembling those of a terrestrial Gilbert-type delta (*e.g.* a steep sloping foreset region and shallow sloping topset and bottomset beds), observed layering in beds of the fan scarp, and negative/positive relief inferred fluvial features on the deposit surfaces are all consistent with deltaic depositional processes in the formation of Fan #2, which was subsequently modified by glacial/periglacial processes (*e.g.*, a rock glacier) after the formation of the deposit. While these observations are most consistent with fan formation via deltaic processes, they do not preclude the possibility of concurrent alluvial fan and deltaic formational processes (*i.e.*, an alluvial fan-delta).

4.3. Fan #21

4.3.1. Mineralogy and Morphology

Phyllosilicates are exposed in high albedo regions on and distal to the scarp of this deposit (Figure 13A). CRISM spectra of these phyllosilicates are characteristic of an Fe/Mg-smectite (displaying absorption features at ~1.4, ~1.9, and ~2.3 μm), most consistent with nontronite (perhaps mixed with saponite) (Figure 14A & B). Strong signatures of spectrally similar Fe/Mg-phyllosilicates are also present in the watershed feeding the fan, and on the floor and walls of the inlet valley connecting the watershed and the deposit (Figure 13B, C, & D, and Figure 14A & B). The presence of Fe/Mg-phyllosilicates in both the lower beds of the deposit and in the drainage basin suggests that phyllosilicates have been transported and redeposited in the fan beds.

A relatively minimal mantling of dust on the surface of this deposit (Figure 13E) allows a thorough analysis of mineralogy. In addition to phyllosilicates exposed in the distal beds of Fan #21, both high- and low-calcium pyroxene are present on the surface of and distal to this deposit (Figure 13F and Figure 14C & D). Low-calcium pyroxene is concentrated on the surface of the deposit and high-calcium pyroxene is located on the surface of and distal to the deposit (Figure 13F). The unique spatial locations of these two types of pyroxene suggest multiple episodes of deposition, or modification of the fan surface after its formation (*e.g.*, aeolian transport and deposition). Because low-calcium pyroxene is commonly associated with terrain in the southern highlands (Mustard *et al.*, 2005), the identification of this mineral in this deposit may be further evidence for erosion, transport, and redeposition.

This deposit is a large, low-relief, fan-shaped feature with a frontal scarp (Figure 15A & B). Alternating layers of differing tonality are exposed on the scarp of the fan toe (Figure 15C & D) suggesting variations in layering. The apparently segregated concentrations of phyllosilicates (and therefore, inferred smaller grain-sizes at the time of deposition, - based on the size of clay particles) near the fan toe are consistent with fan formation via deltaic processes, but could also be created by a fluvially-dominated alluvial fan (Blair and McPherson, 1994). Alternatively, the relatively constant and shallow (average ~2˚) slope of the top surface of the fan (Figure 15B) is consistent with deltaic deposition, and inconsistent with alluvial fan depositional processes, which allow steeper angles of sediment deposition (Blair and McPherson, 1994). The slope of the scarp of this deposit is also relatively shallow, between 4-5˚, and a trench distal to the fan toe (Figure 15B) may be due to post-formational erosion of the fan scarp.

4.3.2. Thermal Inertia

The surface of Fan #21 has thermal inertia values that are higher than those of any of the other deposits observed, ranging between ~300-400 (Figure 7); this may be a result of the minimal amounts of dust cover on the fan surface (Figure 13E). A phyllosilicate-bearing region near the toe of the fan surface has elevated thermal inertia vales between 400-475, suggesting induration. The toe of this fan has low thermal inertia values between ~200-300, which may be due to the slope of the scarp. Finally, regions in the inlet valley and distal to the fan contain areas of very high thermal inertia (500-850), possibly suggesting induration. Large areas of high thermal inertia distal to the fan correspond with topographic lows, suggesting possible induration of fine-grained sediment (perhaps phyllosilicates) in these regions, though CRISM targeted data in this area are not available and the area was therefore not analyzed mineralogically.

4.3.3. Interpretation of Depositional Environment

In summary, the hydrated minerals and morphologies associated with this deposit are consistent with formation in either a fluvially dominated alluvial fan environment (Blair and McPherson, 1994), or a deltaic environment, and high thermal inertia values coinciding with phyllosilicate-bearing regions may suggest induration. However, the shallow slopes of the top surface of the deposit are most consistent with fan formation in a deltaic environment.

4.4. Fan #25

4.4.1. Mineralogy and Morphology

Phyllosilicates are present in the center of the crater containing this deposit, and in the outlet valley on the opposite side of the crater (Figure 16A). The strongest phyllosilicate signatures are present on the fan surface and in a small, elongate depression located on a deposit superposing the southern edge of this fan (Figure 16B). Spectra on/near this deposit are consistent with a Fe/Mg-smectite, perhaps saponite and/or vermiculite, having distinct absorption features at ~1.9 and ~2.3 µm, but lacking a strong 1.4 µm feature in reflectance and ratioed reflectance data (Figure 17) (although this feature is present in continuum-removed data). The lack of a 1.4 µm absorption feature in ratioed CRISM data may be due to the presence of mafic minerals, such as pyroxene on the deposit (Figure 16C), possibly masking the 1.4 µm absorption feature in spectra. Both high- and low-calcium pyroxene are present on the surface of Fan #25 (Figure 16C and Figure 17C & D). Low-calcium pyroxene is common in the highlands, where this deposit is located (Mustard *et al.*, 2005). The surface of Fan #25 is relatively dusty (Figure 16D), and mineralogically unique spectra of phyllosilicates and/or pyroxene are observable on the few areas of the deposit with little dust cover. Relatively high amounts of dust on the surface of Fan #25 and in the outlet valley (Figure 16D) suggest that the locations of phyllosilicates and other minerals are more extensive than what is presently observable.

Fan #25 is a lobate deposit (Figure 18A), inferred to be Hesperian in age based on crater counting and superposition relationships with surrounding terrain (Dohm *et al.,* 2001; Mangold and Ansan, 2005). Another deposit superposes Fan #25 on the southern edge (Figure 18A), and may have formed by a mass wasting event (perhaps slope failure of the crater wall) inferred by its location, morphology, and apparent stratigraphic relationships. Layering is present in the lower beds of this fan (Figure 19A). Small scale polygonal fracturing is apparent in HiRISE images on/near multiple small mesas distal to the fan toe (Figure 19B), and boulder-sized clast inclusions are present in the fan scarp.

Variations in material strength of layers suggest vertical stratification in distal fan regions, and possibly in the lower beds of the fan. Large clast inclusions in the lower fan beds and a deeply incised inlet valley suggest that this deposit was created by long-lived flow with a high sediment and/or water flux.

This deposit was previously hypothesized as a delta based on morphologic and topographic similarities to terrestrial Gilbert-type deltas (Mangold and Ansan, 2005), including shallow sloping inferred topset and bottomset beds (~1˚ and <1˚, respectively), and relatively steeply sloping foreset beds (~9˚) (Figure 18B). The breaks in slope and topographic profile of this fan are consistent with a delta, and inconsistent with that of an alluvial fan, which would show a slope break at the crater wall (rather than multiple kilometers within the crater), and a concave topographic profile (Mangold and Ansan, 2005). A similar average slope in the inferred foreset beds of the deposit and a small step between slopes suggests that part of this slope has been eroded back (Figure 18B). Additionally, a small trench is apparent distal to the fan scarp in the topographic profile. These morphologies may have formed as a result of preferential erosion (*e.g.*, fluvial, lacustrine, and/or aeolian) after formation of the fan.

A topographic profile through the crater (Figure 16E) reveals a relatively flat-floored crater, suggesting that the crater has been filled in with significant amount sediment. The elevation of the inlet valley before entering this crater is ~2765 m, and the elevation of the top-most portions of this deposit near the inlet valley is ~2730 m. Additionally, the outlet valley elevation is ~2750 m, suggesting that water in the crater must have ponded to at least this elevation, which is higher than that of the top surface of the deposit. If a minimal amount of post-depositional deflation has occurred on the top-most fan surface near the inlet valley (as may be suggested by a lack of morphologies consistent with aeolian deflation - such as sinuous ridges - and a relatively constant, shallow sloping topographic profile of the top-most fan surface, consistent with that of the inlet valley), and if the fan depositional period was concurrent with the formation of the outlet valley (as is suggested by Mangold and Ansan, 2005), these similarities in elevation would be consistent with the sub-aqueous formation of this deposit, implying deltaic formational processes.

4.4.2. Thermal Inertia

Thermal inertias associated with Fan #25 are relatively low (Figure 7), likely due to a mantling of surface dust on the deposit (Figure 16D). An elongate distal-fan depression and areas of the fan surface found to bear phyllosilicates have relatively high thermal inertia values between ~180-250. Additionally, portions of the inlet valley of this deposit (where phyllosilicates were not identified) have relatively high thermal inertia values from, ~180-280. The highest thermal inertia values associated with this deposit (up to ~360) are located in the center of the crater, where phyllosilicates were also identified. This correlation of phyllosilicates with the highest thermal inertias in the center of the crater may be suggestive of selective grain-size sorting in a lacustrine environment, which later underwent induration (causing relatively high thermal inertia values). One inconsistency between the thermal inertia values of this and other deposits is that although phyllosilicate-bearing regions do exhibit relatively high thermal inertia values (suggesting induration), thermal inertia values associated with this fan and its receiving basin are less than those associated with other deposits - all less than 400, which is a minimum hypothesized thermal inertia for indurated materials (Jakosky, 1986). The reason for relatively lower thermal inertia values of phyllosilicate-bearing regions in this crater is uncertain, but possible explanations could be due to mixed sediment sizes, or an extensive mantling of dust on the surface.

4.4.3. Interpretation of Depositional Environment

In summary, the presence of hydrated minerals and morphologies associated with this deposit suggest aqueous processes in this area. Furthermore, the slopes and slope breaks associated with this deposit are most consistent with those associated with terrestrial deltas. The location of phyllosilicates, and coinciding relatively high thermal inertias (possibly suggesting induration of clay minerals) in the center of the crater suggest the presence of water and preferential sorting of fine-grained clay sediment in a lacustrine environment. Additionally, the relative elevations of the fan surface and the outlet valley suggest the sub-aqueous formation of this deposit.

4.5. Identifications of Hydrated Minerals in Other Deposits

In addition to the four fans described above, two other deposits were identified during this work that displayed hydrated minerals: Fan #22 and Fan #19 Distal Deposit.

4.5.1. Fan #22

4.5.1.1. Background

This fan-shaped feature is located in the western Medusa Fossae Formation (MFF) near the global dichotomy boundary. It is a relatively large feature with many positive relief radially-oriented sinuous ridge features on its surface (Figure 20), hypothesized to have formed by induration of fluvial sediments (likely due to chemical cementation) and subsequent aeolian abrasion of the surrounding terrain (Burr *et al*., 2009; Burr *et al*., 2010). These inverted ridges have the plan-view appearance of fan distributary channels based on their sinuosity and radial patterns that diverge away from the fan apex.

Although this deposit was previously proposed to have formed via fluvial processes based on its fan-shaped morphology, frontal scarp, and apparently divergent fluvial pattern (Williams and Edgett, 2005; Irwin *et al.*, 2005), Lefort *et al.* (2011) show that the fan-shaped feature is part of a larger network of sinuous ridge features that were previously not resolvable in lower resolution THEMIS and MOC (Mars Orbital Camera) images initially used to identify this feature. Furthermore, Lefort *et al.* (2011) demonstrate using high resolution CTX DEMs that the sinuous ridges of this deposit slope down to the south-west, *toward* the hypothesized apex of the deposit, suggesting convergent flow. If these ridges are indeed convergent, rather than divergent, this feature would not have formed by deltaic (or alluvial-deltaic) processes. However, the surface of this feature has been significantly eroded and covered by aeolian sediment (as evidenced by the presence of inverted ridges and many yardangs), so that the inconsistent slope patterns on the surface of this deposit may not be original slopes, but post-depositional surfaces. This allows for the possibility that the original slopes of the sinuous ridges were to the north-east, and that the flow may indeed have been divergent.

4.5.1.2. Mineralogy and Morphology

In addition to the apparently divergent sinuous ridges on the fan surface, many north-south oriented linear ridges, interpreted as yardangs (*e.g.,* Ward, 1979), cross-cut the sinuous ridges (Figure 21A & B). Multiple locations in the distal fan portions of the eastern side of the fan display layering in the rock at a scale within the limits of CTX resolution (*i.e.,* tens of meters) (Figure 21). There is also at least one large trench between sinuous ridges on the fan surface where the trench walls have been eroded back to expose layering (Figure 21A).

This deposit is much larger than any other deposit in this study, having an estimated area of approximately 600 km^2 (Table 2). This area is nearly eight times larger than the average estimated area of all 33 Irwin *et al.* (2005) fans (76 km^2), and twice as large as the second largest fan (Fan #12, ~300km^2), which is located in Holden crater.

The MFF is mantled with dust, making it difficult to obtain useful spectral information of underlying compositions from CRISM data of this area. However, Fe/Mg-phyllosilicates were identified in a region of relatively less dust cover in CRISM image FRT000063A8, located south of this deposit (Figure 20 and Figure 22A, B, & C). Spectra of phyllosilicates in this image are most consistent with Fe/Mg-smectites (perhaps nontronite and/or saponite), with absorption features at ~1.4, 1.9, and 2.3 µm (Figure **23**). Because this CRISM image is ~60 km away from the fan apex, and located in a large, topographically lower trough (with as much as 850 m of relief between the fan surface and trough floor in this image), it is difficult to directly connect this identification of phyllosilicates with the deposit itself. Phyllosilicates in this image are located on the tops of, and at the base of two semi-parallel, curvilinear, elongate knobs where dust cover is relatively low (Figure 22B & C). Layering has been exposed by erosion on many small mounds surrounding the knobs. Phyllosilicates in this CRISM image are present in light toned areas that display sub-horizontally layered and polygonally fractured terrain in HiRISE imagery (Figure 24). Darker toned sediment, bearing spectral signatures of pyroxene (specifically high-calcium pyroxene), is observable in areas having relatively little dust cover (Figure 22C & D) in topographic lows between the knobs, forming sand dunes (Figure 22A) (Burr *et al.*, 2011).

4.5.1.3. Thermal Inertia

The values of thermal inertia on this deposit are very low relative to those observed in other deposits (all less than 400, but predominantly between 100-150) (Figure 7). These low thermal inertias are likely indicative of a dust-mantled surface, consistent with the rest of the MFF region. Thermal inertia on this fan display linear radiating patterns coinciding with the sinuous ridges. An area of relatively high thermal inertia (between 180-300) on the fan surface is morphologically consistent with a small trench between sinuous ridges that is filled with aeolian sediment (as evidenced by dunes on the trench floor) and displays sub-horizontal layers in the eroded walls of the trench (Figure 21A). The northern distal portions of the deposit, where CRISM image FRT00009708 is located, display relatively high thermal inertia values of ~190-290. These relatively high (though absolutely low) thermal inertia values may indicate an area with less dust cover or more induration, or could represent a unit of a distinct grain size that has been preferentially sorted into the distal regions of the deposit. A region south-east of the fan displays the highest thermal inertia values near the fan (up to ~380), but does not appear to be morphologically associated with Fan #22, and is therefore, not discussed in this study.

4.5.1.4. Interpretation of Depositional Environment

Because phyllosilicates identified in assciation with this fan are a significant distance south of and topographically below the deposit, it is difficult to confidently link them with the deposit itself (either having been transported and deposited, or formed *in situ*). Furthermore, this deposit is significantly larger than any of the other features in this study, and the inconsistencies of slopes of sinuous ridges may suggest that apparent divergent flow patterns are in fact convergent patterns (Lefort *et al.*, 2011). Though it is evident that hydrated minerals and aqueous morphologies are present in the region of this deposit, a conclusive interpretation of the formational processes is elusive.

4.5.2. Fan #19 Distal Deposit

4.5.2.1. Mineralogy and Morphology

Fan #19 Distal Deposit is located distal to Fan #19. This deposit is not one of the 33 deposits described by Irwin *et al*. (2005) that were the premise of this study, but was previously hypothesized to be multiple superposed alluvial fans by Moore and Howard (2005). Unlike other deposits in this study, this deposit is not fan-shaped, and fills a small unnamed crater that is situated within/on the edge of a larger unnamed crater containing Fan #19 (making it difficult to constrain the boundaries and size of this deposit) (Figure 25). The small crater containing this deposit appears to have been filled with sediment (perhaps due to a combination of fluvial and mass wasting processes); the northwest rim of the crater has been almost entirely eroded, opening up to the center of the larger crater (Figure 26A).

The relief of the deposit is at least 650m from inlet valleys at the crater rim to the estimated toe. The average slope of the deposit (from the apex) is ~2.1-2.2˚, with decreasing slopes away from apex, where slopes as large as 4.5-6˚ exist in the first few kilometers near the apex (Figure 26B). The overall high relief, steep slopes near the apex, and decreasing slopes in distal portions of the deposit are consistent with a fluvially-dominated alluvial fan but may also be consistent with an alluvial fan-delta (consisting of a distinct sub-aerial and sub-aqueous region) (Blair and McPherson, 1994). The lack of a unique fan shape could be due to the large size of the deposit compared to the relatively small containing crater, or post-depositional gravity failures of the crater wall mantling the original shape of the deposit.

Multiple converging inlet channels, ranging from 10-18km in length, entrench the crater rim to the south, implying multiple depositional events in the formation of this deposit. Flow features, primarily oriented radial from inlet valleys, are traceable down-slope of the deposit (Figure 26A), forming prominent, curvilinear ridges, with smooth inter-ridge regions (Figure 26C). These ridges may be inverted flow features or fluvial channels on the deposit. Small impact craters are present on the deposit, though the rims of most of the small craters have been heavily eroded. The surface of this deposit has a rough, blocky texture, with boulder-sized clast inclusions well-distributed throughout - especially visible eroding from curvilinear ridge features (Figure 26C), suggesting a high stream competence that distributed the clasts, and post-depositional modification of the ridges, exposing the clasts.

Gullies on the eastern crater wall appear to be mass wasting scarps that have contributed to sediment deposition in the crater (perhaps post-formation of the deposit) (Figure 26A). Sand dunes, oriented E-W (perpendicular to inferred fluvial flow direction), are present within the crater, on the floors of the inlet valleys, and on smooth surfaces between ridge features on the surface of the deposit.

Phyllosilicates in this deposit were identified in CRISM targeted data in a smooth, inter-ridge region (Figure 27A & B), but locations of phyllosilicates were difficult to map due to the low signal to noise ratio in the data, likely resulting from the presence of many ridge features and CRISM data artifacts in shadows/strong brightness boundaries of the D2300 CRISM spectral summary parameter. This deposit has relatively less dust cover than some other deposits in this study (Figure 27C), but no other unique spectral signatures were identifiable on the surface of the deposit. Spectra of phyllosilicates on the deposit are most consistent with an Fe/Mg-phyllosilicates such as saponite and/or vermiculite (Figure 28). A ~1.4 µm absorption feature is not prominent in these spectra, but distinct absorption features are present at ~1.9 and ~2.3 µm (Figure 28).

Although the lower spatial and spectral resolution of CRISM multispectral data does not provide as detailed morphologic constraints of phyllosilicates as the targeted CRISM targeted data, the larger spatial coverage of multispectral data shows that phyllosilicates are widespread on this deposit (*i.e.,* abundant within the small crater containing the deposit), and are also present on the floor of the larger crater that contains the small crater in which the deposit is located (Figure 29).

The presence of phyllosilicates on the deposit itself and within the larger adjacent crater, in addition to the eroded northwest crater wall leading into the larger crater (Figure 26A) suggest that both the large crater, and the small crater in which deposit #19 Distal is located contained water at one time. Phyllosilicates may have altered in place in a lacustrine environment, or may have been transported into the area via fluvial processes. The presence of phyllosilicates in an inlet valley on the northeast rim of the larger crater (in CRISM image FRT16F2B) suggests that phyllosilicates may have been transported to these craters.

4.5.2.2. Thermal Inertia

The surface of the deposit has relatively high thermal inertias, with the highest values predominantly located on smooth regions on and distal to the deposit (Figure 7). These high thermal inertias range from ~325-625, perhaps due to indurated materials such as phyllosilicates. Inlet valleys display relatively low thermal inertia values (less than 200), with some moderately high thermal inertia values on steep sloping walls of the valleys.

4.5.2.3. Interpretation of Depositional Environment

Due to the presence of multiple inlet valleys, and the combined identifications of hydrated minerals and unique fluvial/alluvial morphologies (*e.g.*, curvilinear ridge features interpreted as inverted channels, and a high stream competency inferred from the well-distributed presence of boulder-sized clasts throughout the deposit), the formational mechanisms of this deposit are interpreted as being due to multiple alluvial fans and/or alluvial fan-deltas that filled that crater and degraded that northwest crater rim. Uncertainties regarding the time of formation of the deposit with regards to the time of a possible lacustrine environment in the crater make it difficult to constrain the formational mechanisms of this deposit. However, well preserved flow features in the upper portions of the deposit (having steeper slopes) and predominantly smooth regions in the lower portions of the deposit (having relatively flat slopes) (Figure 26A & B) argue a case for two distinct regions in the deposit – perhaps a subaerially- and a subaqueously-formed region, which would suggest that this deposit is an alluvial fan-delta, the lower portion having formed in a lacustrine environment. A further determination of formational processes of this deposit is difficult to constrain without more knowledge of the relative time periods of fluvial and possible lacustrine environments in this crater.

4.5.3. Other Possible Detections of Hydrated Minerals

In addition to the six phyllosilicate-bearing deposits presented in detail in this study, other deposits discussed by Irwin *et al.* (2005) were found to possibly bear phyllosilicates, carbonates, and/or sulfates on the fans themselves, and/or in the receiving basin. Because these detections are not certain (*i.e.,* the spectra are noisy but may display absorption features consistent with hydrated minerals), these deposits are not addressed in further detail here, but the possibility of the presence of hydrated minerals in these deposits suggests that there are more deposits bearing hydrated minerals than these presented in this study.

5. Discussion

Of the 26 deposits initially examined in this study, five fans discussed by Irwin *et al.* (2005) were found to bear hydrated minerals in or near the deposits, representing ~20% of the fans (this statistic excludes deposit #19 Distal, as it was not one of the original deposits in the previous study). Furthermore, of all of the 33 deposits described by Irwin *et al.* (2005) (including the seven deposits located in Holden, Eberswalde, Jezero, and Gale craters that were previously identified to bear phyllosilicates), a total or 13 deposits, ~40%, either bear phyllosilicates or are contained in (or very near) basins that bear phyllosilicates and/or other phyllosilicate-rich deposits.

This large percentage of hypothesized aqueous landforms that are positively associated with hydrated minerals, in addition to multiple other deposits with the possible presence of phyllosilicates (*e.g.*, Section 4.5.3.), strongly suggests that the early Martian climate facilitated formation of phyllosilicates, either *in situ* or formed elsewhere and subsequently eroded, transported, and redeposited in the beds of deposits.

5.1. Implications for Depositional Environments and Evaluation of Delta Hypothesis

Five of the six deposits discussed in detail in this study were found to bear phyllosilicates on, and distal to, the deposits themselves (phyllosilicates being positively identified only distal to Fan #22, and possibly identified in the hypothesized fan beds). Morphologies in four of the six deposits (Fans #2, 21, 25, & 26) are consistent with deposition in an aqueous environment, and morphologies of the two additional deposits (Fan #22, and 19 Distal Deposit) are consistent with formation via fluvial processes. Finally, the depositional basins of at least three of these deposits (Fans #2, 25, & 19 Distal) display morphologies and/or mineralogies that are consistent with the presence of standing water within the basin.

Of these six deposits, Fans #2, 21, 25, & 26 are the most likely candidates for having formed via deltaic processes, based on the combined identifications of hydrated minerals and aqueous morphologies in beds of the fan deposits and in distal fan regions, suggestive of aqueous processes in the formation of these deposits. Furthermore, the topographic and morphologic resemblance of these deposits to terrestrial deltas, and the identification of morphologies associated with aqueous processes and/or hydrated minerals in some of the depositional basins suggest the presence of standing water in the basins, further suggesting that these fans may have been deposited in standing water, which would confirm this delta hypothesis.

It should, however, be considered that a history of flowing and standing water in a basin does not necessarily imply deltaic formation of a sedimentary deposit in such basin, as the fluvial and lacustrine environments may not have co-existed. Additionally, the limited two dimensional observations of these three dimensional landforms - which have been modified by post-depositional processes and (as with many areas of Mars) are mantled by a spectrally bland dust cover - hinders the ability to interpret the formational processes of these landforms with absolute certainty.

Three of the deposits in this study (Fans #2, 25, & 26) bear morphologic resemblances to terrestrial Gilbert-type deltas. Figure 30 displays a simplified hypothetical diagram of the internal structure of a Martian intracrater Gilbert-type delta. This diagram shows an internal Gilbert delta structure with shallow-dipping topset beds, steeply-dipping foreset beds, and shallow-dipping bottomset beds (Leeder, 1999). In terrestrial settings, these deltas are commonly coarse-grained (sand- to gravel/boulder-sized clasts) (*e.g.*, White, 1992) with the finest-grained sediment concentrated in the distal regions (*e.g.*, bottomset beds) of the deposit; they form in lacustrine environments where the density of the river water is the same as the water in the basin (*e.g.*, Colella *et al.*, 1987).

The abundance and well-distributed locations of phyllosilicates in the crater containing Fan #19 Distal Deposit also suggests that this crater may have contained standing water, though the steep slopes of this deposit (and slope break at the crater wall) are most consistent with an alluvial fan rather than a delta(*e.g.*, Blair and McPherson, 1994). This contrasting evidence could suggest that the formation/deposition of the deposit and phyllosilicates are not genetically linked. Alternatively, this evidence, as well as differences in the apparent preservation of flow features in upper and lower regions of the deposit, could suggest that this deposit is an alluvial fan-delta (containing distinct sub-aerially and sub-aqueously formed portions) (Blair and McPherson, 1994). A lack of knowledge regarding the relative time periods of fluvial and possible lacustrine activity in the crater prevent any further unique identification of the formational processes of this deposit.

While apparent distributary patterns suggest fluvial processes in the formation of Fan #22, morphologic evidence for deposition of this fan in an aqueous environment is lacking and inconsistent with deltaic depositional processes. Heavy dust cover and post-depositional aeolian erosion of this fan and nearby areas may have obscured observations of original minerals and morphologies.

In this study, I focused on testing the delta hypothesis for these deposits, and in doing so, I also considered other possible formational mechanisms, including alluvial fan, mass wasting, glacial, and volcanic processes (Table 3). Some of the deposits in this study displayed characteristics that may be consistent with these alternative formational mechanisms. For example, Fan #21 displays morphologies that are consistent with possible formation via both deltaic and (fluvially-dominated) alluvial fan processes (Blair and McPherson, 1994). However, deltaic formational processes are favored for this deposit, primarily due to the shallow slope (~2˚) of the surface, consistent with deltaic formation. Some morphologies in the inlet valley and on the surface of Fan #2 suggest modification by periglacial processes, such as a rock glacier (*e.g.*, Ritter *et al.*, 2002), although the superposition of these morphologies on the fan surface, and the inferred younger age of glacial activity in this crater (Dehouck *et al.*, 2010) suggests that periglacial/glacial processes contributed to post-formational modification, rather than the original formation of this deposit. Lastly, inferred mass wasting morphologies are also observable in association with many of these deposits (*e.g.*, Fan #19 Distal Deposit and Fan #25), however the superposition of these morphologies on the deposits, the presence of long inlet valleys (suggesting fluvial processes), and the lack of conclusive evidence suggesting fan formation via mass wasting processes (Table 3) precludes this as a primary formation mechanism for all of the deposits. A possible exception to this is Fan #19 Distal Deposit, which appears to have been heavily modified by mass wasting processes from the containing crater wall; however, multiple inlet valleys and possible surface flow features (inferred to be fluvial in origin) suggest that the primary (and/or dominant) formation mechanisms of this deposit were fluvial (perhaps fluvio-lacustrine). None of my observations of these deposits support possible formation via volcanic processes.

5.2. Authigenic versus Allogenic Phyllosilicate Formation

The fact that most of the deposits discussed are located on the global dichotomy boundary (Figure 1) and have inlet valleys leading from the south suggests that sediment transport from the southern highlands and redeposition is a possible source (though not necessarily an exclusive source) of phyllosilicates in many of the deposits. Additionally, the presence of phyllosilicates in many upstream watersheds (*e.g.*, Fans #26 & #21) suggests that phyllosilicates may have formed or ponded in watersheds before deposition in fan beds.

Alternatively, concentrations of relatively high thermal inertia phyllosilicates in the center, or topographic lows of basins (such as Fans #2, 26, & 25) may suggest that water ponded in these basins, perhaps for an extended enough amount of time to facilitate the *in situ* alteration and induration of hydrated minerals. A lack of information regarding the duration of lacustrine activity in the basins (*e.g.,* perennial versus ephemeral lakes) causes difficulties in the positive identification of authigenic phyllosilicates.

A combination of authigenic and allogenic phyllosilicate formation is also plausible for many fans in this study. Thus, the results of this study do not necessarily allow the conclusive interpretation of the origin of all phyllosilicates present in these deposits.

Lastly, all formational/depositional mechanisms for phyllosilicates discussed thus far have strictly involved surface water processes; it should also be considered that groundwater may have played a role in the formation/deposition of phyllosilicates in these deposits – either by authigenic subsurface formation (and later exhumation) of phyllosilicates, and/or by allogenic phyllosilicate formation, followed by subsurface transport through a porous medium and subsequent surface deposition where the groundwater table intersects the surface topography. While the presence of inlet valleys suggest fluvial processes in the formation of these deposits (and transport of phyllosilicates), it is possible that some of the valleys originated via groundwater sapping (*e.g.*, Fan #2, discussed in Section 4.2.2.).

5.3. Post-Depositional Modification of Deposits

Most of the deposits analyzed in this study are interpreted as having formed during the late Noachian to early Hesperian time periods (Dohm *et al.*, 2001; Mangold and Ansan, 2005; Irwin *et al.*, 2005; Dehouk *et al*., 2010). Considering these inferred ages of the deposits, it is likely that some post-depositional modification of the fan surfaces has occurred since the time of formation, and that many corresponding morphologies of the deposits have been modified, eroded, and/or mantled by aeolian processes. Therefore, discrepancies likely exist between present day observations and original morphologies of the deposits.

Based on observations of relative degradations of surface features, some fans appear to have undergone more modification than others. For example, the scarp of Fan #2 has likely undergone extensive headward erosion, based on the large areal extent of the fan slope observable in the topographic profile, compared to the relatively small areal extent of the fan scarp observed in visible imagery (Figure 11C).

The sinuous ridge features on the surface of Fan #2 are of a comparable size and sinuosity to the main trough of the distributary network on the surface of Fan #21, suggesting that the formation processes of these features may have been the same. Erosion of areas surrounding negative relief troughs on the surface of Fan #2 could have caused the subsequent formation of positive relief sinuous ridge features presently observed on the fan surface. It is likely that these sinuous ridge features formed by aeolian deflation, considering the back-wasting that appears to have occurred on the frontal slope of Fan #2. The negative relief of troughs on Fan #21 may suggest that this deposit is less degraded than Fan #2; though factors other than age (*e.g.,* differences in sediment size or resistance to erosion) may also be responsible for the differences in surface morphologies observed on these fans.

A number of different factors, including variations in age, sediment size/composition, and regional variations in wind regime, could have led to the wide variety of post-depositional degradation that appears to have occurred on the surfaces of different fans (*e.g.*, Ritter, 2002; Prothero & Schwab, 2004). It is likely that the more degraded deposits are older than other less degraded deposits, allowing for more time in the erosion process of these fans. Variations in the size and composition of sediment comprising the fans would lead to differences in the erosion of the deposits and their distributary channels. Larger grain sizes and more resistant material in the interfluves would hinder erosion of regions surrounding channels, and the subsequent formation of sinuous ridges (Burr *et al.*, 2009; Burr *et al.*, 2010), such as the less eroded troughs of Fan #21 in comparison to the sinuous ridge features of Fan #2. Lastly, differences in the amount of, and/or exposure to aeolian (and/or subsequent fluvio-lacustrine) erosion would cause variations in the modifications which each fan undergoes. Higher wind regimes in a region, or waves from a lacustrine environment post-fan deposition would increase the amount of erosion on a deposit (Prothero & Schwab, 2004). Additionally, a relatively high relief between a fan surface and crater wall (as is the case with Fan #21 relative to Fan #2) could shelter the deposit from significant aeolian erosion after formation.

Because of the possible discrepancies between original and present day morphologies, present day observations must be interpreted with great care, as these observed morphologies may not accurately reflect those of the original fans. Nevertheless, the well preserved nature of the overall morphology of these deposits over such an extended amount of time suggests that the amount of post-depositional modification to the deposits is minimal enough such that accurate interpretations can be drawn from present day observations.

5.4. Inter-deposit Correlations of Thermal Inertia

The range of thermal inertia values varies between deposits. Fans # 2, 21, & 26 all display a wide range of thermal inertias (between 0-850) on the fan surfaces and in their associated basins. The highest thermal inertia values on/near these fans correspond to phyllosilicate-bearing regions. These thermal inertia values are consistent with previously hypothesized values for indurated surfaces (*i.e.,* >400) (Jakosky, 1986). Alternatively, Fans # 22 & 25, which are both located in globally dusty regions, have thermal inertia values that are all less than 400, although morphology (e.g., yardangs, inverted fluvial features) very strongly indicates an indurated lithology for at least Fan #22. An extensive mantling of surface dust may be responsible for the relatively low thermal inertias associated with the latter-mentioned deposits.

The calculation of thermal inertias also revealed that the highest thermal inertia regions (and mostly all phyllosilicate-bearing regions) of many deposits coincide with topographically low areas and/or in the center of their basins. This concentration of fine grained, indurated sediment (as inferred from grain sizes of clays and high thermal inertias) in the topographic lows is consistent with differential sorting of sediment in a lacustrine environment, suggesting that these regions of high (and/or relatively high) thermal inertia may represent locations where water ponded and differentially sorted grain sizes.

Most phyllosilicate-bearing surfaces described in this coincide with high (or relatively high) thermal inertia values which suggest induration of the phyllosilicates. Additionally, the toes of all of the fan-shaped deposits except Fan #19 Distal Deposit, which is not fan-shaped, display well-defined differences in thermal inertias from the top surfaces of their associated fans. Although the actual thermal inertias of the fan toes may be inaccurate due to errors in calculating thermal inertia on slopes, these values can be compared between fans to try to determine variations in physical characteristics of the surface. Some of the fans display higher thermal inertia values (relative to the top surface) on the frontal fan scarp (Fans #2 & #26), while others display lower thermal inertia values on the scarp (Fans #21 & lower slope of Fan #25). This variation in thermophysical trends may be due to the less steep slopes of the latter two deposits (see Figures Figure 11C, Figure 5B, Figure 15B, and Figure 18B, respectively, for comparison). However, it should also be considered that both the fan slopes and corresponding thermal inertia values may be controlled by an external factor; for example, the steep-sloped, higher thermal inertia scarps may represent surfaces that have undergone more post-formational erosion, stripping away finer-grained particles associated with the slopes and exposing larger-grained (and perhaps more indurated) sediment further up-fan (*i.e.,* closer toward apex).

5.5. Correlations between Thermal Inertia and Mineralogy

Because CRISM observes the mineralogy of the top few microns of the Martian surface, a veneer of surface dust would obscure the underlying geology. By contrast, THEMIS thermal inertia measures diurnal changes in the temperature in the top few centimeters of a surface. Thus, if a surface is found to bear phyllosilicates, surfaces that don't display phyllosilicates in CRISM data, but have similar thermal inertias to a nearby phyllosilicate-bearing surface may contain phyllosilicates that are covered by a thin (more than a few microns, but less than a few centimeters) mantling of dust. While thermal inertia by itself cannot be used to identify the mineralogy of a surface, similarities in thermal inertia on surfaces in the same vicinity of a THEMIS image indicate similar thermophysical properties and may suggest similar mineralogic compositions.

For example, Fan #26 displays high thermal inertia values (*i.e.*, red regions in Figure 7) in the locations of phyllosilicate detections (both Al and Fe/Mg) on and distal to an elevated knob near the toe of the fan, and in one location in the lower beds of a superposed deposit (compare Figure 3A and Figure 7). Weak phyllosilicates signatures identified within an elongate depression and distal to this depression (on the north scarp of the superposed deposit) also display high thermal inertia values. Many areas in the lower beds of the superposed deposit, and surrounding the elevated knob were suspected to contain phyllosilicates based on consistencies between morphologies and CRISM phyllosilicate summary parameters, but positive CRISM detections of phyllosilicates were not possible in these locations due to dust cover obscuring the underlying minerals. THEMIS data show similar thermal inertia values in all of these described regions, suggesting a thermophysical/compositional correlation between the areas.

Another example of this correlation between thermal inertia and mineralogy is in Ismenius Cavus crater, the basin containing Fan #2. A phyllosilicate unit displaying high thermal inertia values is located in the center of the crater (Figure 8). The extent of phyllosilicates observable in CRISM data does not appear to be nearly as large as the red-colored unit displaying high thermal inertia values in the center of the crater (Figure 7). The morphologic consistencies and similar thermal inertias in this large, red thermal inertia-colored region in the center of the crater suggest compositional similarities. Furthermore, this large region of high thermal inertias is consistent with thermal inertias of the smaller phyllosilicate-bearing region, suggesting that the extent of phyllosilicates in this crater may be larger than what is presently observable in CRISM data.

Based on comparisons of mineralogic and thermal inertia observations of phyllosilicate-bearing deposits, this correlation would suggest that the extent of phyllosilicates in the areas surrounding the fans is more widespread than what is observable in CRISM data. This combined analysis of shorter wavelength mineralogic data with longer wavelength thermal inertia data can be a useful method in inferring the extent of mineralogic units in areas that are partially/thinly mantled with dust, making it otherwise difficult or impossible to determine the underlying mineralogy via the use of shorter wavelength spectral data alone.

5.6. Caveats to Scientific Analysis Approach

Multiple caveats should be considered in evaluating the results of this study. First, the unavailability of high-quality CRISM data for some fans could have biased my interpretations by putting more emphasis on those areas that happened to have good coverage. It should also be considered that the detection of hydrated minerals on/near the deposits (or lack thereof) in and of itself is not necessarily diagnostic of the presence or absence of aqueous processes in the formation of these fan deposits. As such, it is important to concurrently consider multiple datasets in the examination of the formational processes of the deposits.

While the combined presence of hydrated minerals and aqueous morphologies on or near a deposit is indicative of aqueous processes responsible for the formation of the minerals and perhaps the formation of the fan deposits, the *absence* of hydrated minerals and/or aqueous morphologies does not preclude the possibility of aqueous processes having formed the deposit. This absence could occur if phyllosilicates were not present in the drainage basin and therefore, could not have been transported and deposited in the fan. Or, liquid water could have been present in the drainage basin (and/or the containing paleolake basin), but may not have persisted long enough to alter the source rock to phyllosilicates. Alternatively, liquid water could have existed for long enough periods to foster the alteration of the source rock to hydrated minerals, but perhaps the composition of the source rock was resistant to aqueous alteration, or the chemistry of the water was not conducive to the formation of hydrated minerals. If, on the other hand, the source rock did alter to phyllosilicates that were subsequently deposited in the fan, these minerals could have been later covered or eroded by secondary surficial reworking of the fan surface.

In locations where phyllosilicates are present, the processes responsible for the formation of these minerals may be different than the processes responsible for the formation of phyllosilicate-bearing deposits. This situation could occur if the aqueous environment in which the phyllosilicates were formed pre-dated the erosional and depositional processes that created the deposit, or if the formation of the deposit pre-dated the authigenic formation of the phyllosilicates in a post-depositional lacustrine environment within the receiving paleolake basin (perhaps evidenced by the presence of phyllosilicates in the deposit or receiving basin, and their absence in the drainage basin and in nearby regions).

5.7. Applications and Significance

The presence and extent of hydrated minerals on Mars helps identify locations where aqueous processes were once prevalent on the Martian surface (*e.g.*, Murchie *et al*., 2009a). Identifying morphologic features that are consistent with terrestrial analogues of such features (*e.g.*, river deltas) provides a constraint on the processes responsible for forming these features, and therefore, the geologic and climatic conditions in which the morphologies formed.

Testing the delta hypothesis is useful in identifying locations that may have once been Martian lakes – *i.e.*, contained standing surface water (*e.g.*, Irwin *et al.*, 2005). The presence of flowing and standing surface water on Mars tells of a dynamic Martian climate that may have once hosted an environment capable of fostering the evolution of living organisms. Overall, the results of this project contribute to the understanding of the history of water on Mars, and therefore, the history of the evolution of planetary bodies in the solar system, and of life therein.

Due to the ability of clays to entomb organic material (Farmer and DesMarais, 1999), phyllosilicate-bearing fan deposits identified in this study are of particular interest to exobiology. Identifying phyllosilicate-rich deposits may uncover records of environments with the high water activity and moderate pH levels necessary to support life on Mars. Because of this, the sites identified in this study are good candidates for future landed missions to Mars. For example, Ismenius Cavus, the crater containing Fan #2, is currently being considered as one of seven candidate landing sites for the ExoMars (Exobiology on Mars) rover, a European-lead robotic mission to Mars, scheduled to launch in the year 2018.

6. Summary and Conclusions

Multiple possible formation mechanisms for these deposits were considered in conjunction with the delta hypothesis, such as alluvial fan, mass wasting, glacial, and volcanic processes (Table 3). Most of the deposits that were found to bear hydrated minerals display morphologic/sedimentologic characteristics that could be attributed to deltas, alluvial fans, and/or alluvial fan-deltas, implying that the delta hypothesis is feasible for many of these deposits. This study emphasizes the importance of utilizing multiple working hypotheses in the analysis of putative features on Mars, such as deltas.

While no single line of evidence is diagnostic in the interpretation of depositional environments, the amalgamation of mineralogic, morphologic, and thermophysical data allow a detailed analysis of the geologic history of a formational environment. Four of the six deposits discussed in this study display characteristics that are consistent with formation in a deltaic environment; but resemblances to other sedimentary features (*e.g.*, alluvial fan and alluvial fan-delta) suggest that more than one process may be responsible for the formation of some of the deposits. The results of this study are consistent with an early Martian climate that was capable of sustaining aqueous environments in which persistent flowing and standing water was stable on the Martian surface (either ephemerally or perennially), allowing the formation of deltas on Mars and a providing further evidence for a changing Martian climate through time.

LIST OF REFERENCES

Bhattacharya, J. P., T. H. D. Payenberg, S. C. Lang, and M. Bourke (2005), Dynamic river channels suggest a long-lived Noachian crater lake on Mars, *Geophys. Res. Lett*., 32, L10201, doi:10.1029/2005GL022747.

Blair, T., and McPherson, J., 1994. Alluvial fan processes and forms. *Geomorphology of desert environments*, 354-402.

Boggs, S., Jr., 1995. *Principles of Sedimentology and Stratigraphy* (2nd ed.). Upper Saddle River, NJ: Pearson Prentice Hall.

Burr, D.M., *et al.*, 2009. Pervasive aqueous paleoflow features in the Aeolis/Zephyria Plana region, Mars. *Icarus*, *200*, 52-76.

Burr, D.M., R.M.E. Williams, K.D. Wendell, M. Chojnacki, J.P. Emery, 2010. Inverted fluvial features in the Aeolis/Zephyria Plana region, Mars: Formation mechanism and initial paleodischarge estimates. *J. Geophys. Res*. 115, E07011, doi:10.1029/2009JE003496.

Cabrol, N.A., and Grin, E.A., 1999. Distribution, classification, and ages of Martian impact crater lakes. *Icarus* 142, 160-172.

Christensen, P.R., *et al.*, 2004. The Thermal Emission Imaging System (THEMIS) for the Mars 2001 Odyssey Mission. *Space Science Reviews* 110, 85-130.

Colella, A., De boer, P.L., and Nio, S.D., 1987. Sedimentology of a marine intermontane Pleistocene Gilbert-type fan-delta complex in the Crati Basin, Calabria, southern Italy. *Sedimentology*, 34, 721–736.

Dehouck, E., *et al*., 2010. Ismenius Cavus, Mars: A deep paleolake with phyllosilicate deposits. *Planet. Space Sci.*, doi:10.1016/j.pss.2010.02.005.

de Pablo, M.A., and Pacifici, A., 2008. Geomorphological evidence of water level changes in Nepenthes Mensae, Mars. *Icarus*, *196*, 667-671.

Dohm, J.M., Tanaka, K.L., Hare, T.M., 2001. Geologic map of the Thaumasia region of Mars. U.S. Geological Survey Map I-2650.

Ehlmann, B.L., Mustard, J.F., Fassett, C.I., Schon, S.C., Head, J.W., Des Marais, D.J., Grant, J.A., Murchie, S.L., 2008. Clay mineralogy and organic preservation potential of lacustrine sediments from a Martian delta environment, Jezzero Crater, Nili Fossae, Mars. *Nat. Geosci.* 1, 355-358.

Farmer, J.D., and Des Marais, D.J., 1999. Exploring for a record of ancient Martian life. *J. Geophys. Res*. 104, 26977-26995.

Fergason, R. L., P. R. Christensen, and H. H. Kieffer, 2006. High-resolution thermal inertia derived from the Thermal Emission Imaging System (THEMIS): Thermal model and applications. *J. Geophys. Res.*, 111, E12004, doi:10.1029/2006JE002735.

Gilbert, G.K., 1885. The topographic features of lake shores, *U.S. Geol. Surv. Annu. Rep.*, 5, 75–123.

Gorelick, N.S., and Christensen, P.R., 2005. THEMIS Global Mosaics. American Geophysical Union, Fall Meeting 2005, abstract #P21C-0161.

Grant, J.A., *et al.*, 2008. HiRISE imaging of impact megabreccia and sub-meter aqueous strata in Holden crater, Mars. *Geology* 36 (3), 195-198.

Grant, J.A., and Schultz, P.H., 1993. Degradation of selected terrestrial and Martian impact craters, *J. Geophys. Res.*, 98, 11, 025-11,042.

Hughes, A.C.G., *et al.*, 2010. CRISM and HiRISE observations of two new phyllosilicate-bearing fan deposits on Mars. *41st Lunar and Planetary Science Conference, March 1-5, 2010, The Woodlands, Texas*, abstract #2096.

Hughes, A.C.G., *et al.*, 2011. A mineralogic and morphologic analysis of four new phyllosilicate-bearing Martian fan deposits. *42nd Lunar and Planetary Science Conference, abstract #2301.*

Irwin, R. P., III, T. R. Watters, A. D. Howard, and J. R. Zimbelman, 2004. Sedimentary resurfacing and fretted terrain development along the crustal dichotomy boundary, Aeolis Mensae, Mars. *J. Geophys. Res.*, 109, E09011, doi:10.1029/2004JE002248.

Irwin III, R.P., Howard, A. D., Craddock, R.A., and Moore, J. M., 2005. An intense terminal epoch of widespread fluvial activity on early Mars: 2. Increased runoff and paleolake development. *J. Geophys. Res.* 110, E12S15.

Jakosky, B. M., 1986. On the thermal properties of Martian fines. *Icarus*, 66, 117–124.

Jauman, R., *et al*., 2007. The high-resolution stereo camera (HRSC) experiment on Mars Express: instrument aspects and experiment conduct from interplanetary cruise through the nominal mission. *Planet. Space Sci.* 55 (7–8), 928–952.

Kieffer, H.H., *et al.*, 1977. Thermal and albedo mapping of Mars during the Viking primary mission. J. *Geophys. Res*., 82, 28, 4249-4290.

Leeder, M., 1999. Sedimentology and sedimentary basins. Blackwell Science, Oxford, 592 pp.

Lefort, A. Burr, D. M., Beyer, R. A., Howard, A. D., 2011. Inverted fluvial features in the Aeolis–Zephyria Plana, western Medusae Fossae Formation, Mars: evidence for post-formation modification, submitted to JGR.

Malin, M.C., and K.S. Edgett, 2003. Evidence for persistent flow and aqueous sedimentation on early Mars. *Science*, 302, 1931-1934.

Malin, M.C., *et al.*, 2007. Context Camera investigation on board the Mars Reconnaissance Orbiter. *J. Geophys. Res.* 112, E05S04.

Mangold, N., and V. Ansan, 2005. Detailed study of an hydrological system of valleys, a delta and lakes in the Southwest Thaumasia region, Mars. *Icarus*, 180, 75–87.

McEwen, A.S., *et al.*, 2007. Mars Reconnaissance Orbiter's High Resolution Imaging Science Experiment. *J. Geophys. Res.* 112, E05S02.

McKeown, N. K., *et al.*, 2009. Characterization of phyllosilicates observed in the central Mawrth Vallis region, Mars, their potential formational processes, and implications for past climate. *J. Geophys. Res*., 114, E00D10, doi:10.1029/2008JE003301.

Mellon, M. T., B. M. Jakosky, H. H. Kieffer, and P. R. Christensen, 2000. High- resolution thermal inertia mapping from the Mars Global Surveyor Thermal Emission Spectrometer. *Icarus*, 148, 437–455.

Milliken, R.E., *et al.*, 2007. Clay minerals in Holden Crater as observed by MRO CRISM. *Seventh Int. Conf. on Mars, July 9-13, 2007, Pasadena, California*, abstract #3282.

Moore, J. M., and A. D. Howard, 2005. Large alluvial fans on Mars. *J. Geophys. Res.*, *110*, E04005, doi:10.1029/2004JE002352.

Murchie, S.L., *et al.*, 2007. Compact Imaging Spectrometer for Mars (CRISM) on Mars Reconnaissance Orbiter (MRO). *J. Geophys. Res.* 112, E05S03.

Murchie, S.L., *et al.*, 2009a. A synthesis of Martian aqueous mineralogy after 1 Mars year of observations from the Mars Reconnaissance Orbiter. *J. Geophys. Res.* 114, E00D06.

Murchie, S.L., *et al.*, 2009b. Compact Reconnaissance Imaging Spectrometer for Mars investigation and data set from the Mars Reconnaissance Orbiter's primary science phase. *J. Geophys. Res.* 114, E00D07.

Mustard, J.F., Cooper, C.D., Rifkin, M.K., 2001. Evidence for recent climate change on Mars from the identification of youthful near-surface ground ice. *Nature*, 412, 411–413.

Mustard, J.F., *et al.*, 2005. Olivine and Pyroxene Diversity in the Crust of Mars. *Science* 307, 1594-97.

Ori, G. G., L. Marinangeli, and A. Baliva, 2000. Terraces and Gilbert-type deltas in crater lakes in Ismenius Lacus and Memnonia (Mars), *J. Geophys. Res*., 105, 17,629–17,641.

Pelkey, S. M., J. F. Mustard, S. Murchie, R. T. Clancy, M. Wolff, M. Smith, R. Milliken, J.-P. Bibring, A. Gendrin, F. Poulet, Y. Langevin, and B. Gondet, 2007. CRISM multispectral summary products: Parameterizing mineral diversity on Mars from reflectance, *J. Geophys. Res.*, 112, E08S14.

Poulet, F., *et al.*, 2005. Phyllosilicates on Mars and implications for early martian climate. *Nature*, 438 (7068), 623-627.

Presley, M. A., and P. R. Christesen, 1997a. Thermal conductivity measurements of particulate materials: 1. A review. *J. Geophys. Res*., 102 (E3), 6535– 6549.

Presley, M. A., and P. R. Christensen, 1997b. Thermal conductivity measurements of particulate materials: 2. Results. *J. Geophys. Res*., 102 (E3), 6551–6566.

Prothero, D. R. & F. Schwab, 2004. *Sedimentary Geology* (2nd ed.). W. H. Freeman and Company.

Ritter, D.F., R.C. Kochel, J.R. Miller, 2002. *Process Geomorphology* (4th ed.). Boston : McGraw-Hill.

Seelos, F. P., S. L. Murchie, D. C. Humm, O. S. Barnouin, F. Morgan, H. W. Taylor, C. Hash, and The CRISM Team, 2011. Crism data processing and analysis products update – calibration, correction, and visualization. *42nd Lunar and Planetary Science Conference, abstract #1438.*

Smith, D.E., *et al.*, 1999. The global topography of Mars and implications for surface evolution. *Science* 284, 1495-1503.

Ward, A.W., 1979. Yardangs on Mars: Evidence of recent wind erosion. *J. Geophys. Res.*, 84 (B14), 814–816.

White, J.D.L., 1992. Pliocene subaqueous fans and Gilbert-type deltas in maar crater lakes, Hoppi Buttes, Navajo Nation (Arizona), USA. *Sedimentology,*39, 931-946.

Williams, R. M. E., and K. S. Edgett, 2005. Valleys in the Martian rock record. *36th Lunar and Planetary Science Conference*, *abstract* #1099.

APPENDIX

1. Tables

Table 1: Data from each primary dataset associated with the deposits

	CRISM (Phyllosilicate-bearing)	HiRISE	CTX	Topography	THEMIS (Night IR)
Fan #26	FRT16525, FRT17610, FRT1D7F0, FRT147E0, & FRT16026	ESP_020160_1820, ESP_015980_1820, & ESP_014358_1820	B16_015980_1821_XN_02N238W	HRSC H5212_0000_DA4	I05445011
Fan #2	FRT19B14, HRL853D, HRSCD2D, & FRT190AE	ESP_013531_2140, PSP_010419_2140 (Crater center), & PSP_006134_2145 (Inlet valley)	P20_008929_2143_XN_34N342W & P16_007202_2146_XN_34N342W	HRSC H2192_0009_DA4	I06160010
Fan #21	FRT64CE, FRT1963E, FRTA332, FRTB001, & FRT17CCB	PSP_001884_1750 & ESP_19975_1750	P08_004218_1748_XI_05S227W	HRSC H1982_0000_DA4	I10375006
Fan #25	FRT944A, FRT1BA41, FRT16D5E, & FRT16F5D	PSP_006798_1405	P15_006798_1405_XI_39S103W	HRSC H4340_0009_DA4	I14589005
Fan #22	*FRT63A8	*PSP_004125_1720	(CTX mosaic)	CTX Mosaic DEM	I17962007
Fan #19 Distal Deposit	FRT1B8E1 & MSP0000821e_03	PSP_001754_1520	B17_016298_1531_XN_26S276W, & B22_018355_1520_XN_28S276W	MOLA	I26201016

*Note: Many more HiRISE and CRISM targeted images are associated with Fan#22, but due to its large size only those discussed herein are included in the table.

Table 2: Hypothesized deltaic deposits discussed in this study (modified from Table 1 by Irwin *et al.*, 2005)

Deposit Name	Basin Name, Diameter	Location (N, E) Quadrangle	Width X Length (km)	Estimated Fan Area (km^2)	Associated Figures	First Reported by
Fan #2	Ismenius Cavus, 62 km	33.9, 17.5 Ismenius Lacus	9.0 X 5.3	12.5	Figure 11	Cabrol and Grin (1999), #19
Fan #19 Distal Deposit	Unnamed (small crater within larger crater)	-27.8, 83.8 Iapygia	~18.0 X 20.0	282.7	Figure 25 & Figure 26	This study
Fan #21	Aeolis Mensae	-5.15, 132.85 Mare Tyrrhenum	17.2 X 10.0	135.1	Figure 13 & Figure 15	Irwin *et al.* (2004)
Fan #22	Aeolis Mensae	-6.75, 151.1 Aeolis	35.7 X 21.5	602.8	Figure 20	Williams and Edgett (2005)
Fan #25	Unnamed, 23 km	-39.2, -103.4 Thaumasia	7.6 X 6.0	35.8	Figure 18	Mangold and Ansan (2005)
Fan #26	Nepenthes Mensae	2.1, 121.6 Amenthes	8.0 X 4.6	28.9	Figure 2& Figure 5	Irwin *et al.* (2005)

*Note: fan areas were estimated by calculating area of ellipse (using fan width and length) and dividing in half.

Table 3: Measurable/Observable Characteristics of Multiple Possible Fan Formation Processes

		Mass Wasting					
	Delta (lacustrine deposition)	**Rock Fall**	**Land Slide**	**Sediment Flow**	**Alluvial Fan (Fluvially or Debris Flow Dominated [a])**	**Glacial Kame Delta/Fan**	**Volcanic Flow**
Composition or grain- size layering	Present: coarsening-upward sequence, finest-grained sediment (*e.g.* clays) in basal & distal regions [b,c]	Not present [d]	Not present	Not present	Present: coarsening-upward sequences (sometimes fining-upward sequence forms during fan decay) [b,c]	Likely present: similar to alluvial fan characteristics	Possibly present as differing lava compositions or interbedded dust
Sub-horizontal layering	Present: sub-horizontal layering due to low energy deposition of fine grained sediment (primarily in distal and/or topset beds) [b,c,d]	Not present due to high energy deposition [d]	Not likely present (unless multiple slides) [d]	Not likely present (unless multiple flows) [d]	Possibly present in distal regions (horizontal layering not likely present in fan due to steep slopes and high energy)	Possibly present in distal regions (similar to alluvial fan characteristics)	Possibly present due to sequences of lava flow
Inlet valley	Present: transports sediment into basin	Not necessarily present	Not necessarily present	Not necessarily present	Present: transports sediment into basin	Possibly Present: transports glacial runoff into basin; incised valley of runoff may not be extensively traceable [d]	Possibly Present: as collapsed lava tubes, or meandering lava channels with lava levee walls
Large clast inclusions (poor sorting and high energy)	Not likely present (can be present in coarse-grained deltas) [e,f]	Present: high energy deposition of very poorly sorted clasts[b,c]	Likely present (may not be exposed in rotational slide)[b,c]	Present: high energy deposition of poorly sorted clasts [b,c]	Likely present: possibly concentrated near proximal apex region of fan [a]	Possibly present: glacially transported sediment; possibly concentrated near apex of fan [d]	Not present
Polygonal fracturing (on fan and distal regions)	Possibly present: formed during playa phase	Not present	Not present	Possibly present (due to entrained water) [b,c]	Possibly present in distributary channels, distal regions or slopes of fans dominated by fluvial processes	Possibly present in periglacial regions (*e.g.*, ice-wedge polygons) or in areas having high glacial water runoff [d]	Possibly present: columnar jointing may resemble this feature

Table 3 - continued

	Delta (lacustrine deposition)	Mass Wasting: Rock Fall	Mass Wasting: Land Slide	Mass Wasting: Sediment Flow	Alluvial Fan (Fluvially or Debris Flow Dominated [a])	Glacial Kame Delta/Fan	Volcanic Flow
Fan distributary channels	Present: delta created by distributary channels transporting sediment into lacustrine environment [b,c,d]	Not likely present (unless later incised)	Not likely present (unless later incised)	Not likely present (unless later incised)	Possibly present: distributary channels may have incised fan surface (common in fluvial process dominated fans, uncommon in debris flow process dominated fans [a])	Possibly present: distributary channels may have incised fan due to glacial runoff [d]	Not present
Surface zonation of grain-sizes/ mineralogy	Present: coarser grained sediment concentrated near mouth of delta, sediment fining away from mouth into prodelta clays/silts [b,c] Lacustrine zonation: very fine grained sediment concentrated in center of basin, coarsening outward radially toward basin margins [c]	Possibly present: possible coarsening of clasts downslope [d]	Not likely present	Possibly present: boulder accumulation at head of flow [d]	Possibly present: relatively coarse-grained sediment concentrated near apex, decreasing clast size downfan (common feature in fluvial process dominated fans, uncommon in debris flow process dominated fans [a])	Possibly present: coarse grained sediment concentrated near apex, sediment fining down-fan	Not present
Hypothesis-specific mineralogy	Phyllosilicates possibly present in bottom/distal layers; perhaps sulfates and carbonates also present if in lake [b]	Mineralogy likely similar to upslope terrain	Mineralogy likely similar to upslope terrain	Mineralogy likely similar to upslope terrain	Phyllosilicates likely concentrated in bottom layers (maybe also present on fan surface) [a]	Phyllosilicates likely concentrated in bottom layers	Ultra-mafic and mafic minerals such as pyroxene and olivine
Additional diagnostic features	Cross bedding in distributary channels [b,c] Presence of natural levees and distributary mouth bars [b,c,d]	Talus cones/debris scars on basin wall (due to slope failure) [b,c,d]	Talus cones/debris scars on basin wall [b,c,d]	Talus cones/debris scars, boulder levees lining channels [b,c,d]	Possible presence of distal fan sandskirt [a]	Presence of proximal glacial landforms: kame/kettles, eskers, moraines, etc. [d]	Presence of proximal volcanic flows/landforms

References: *a:* Blair and McPherson, 1994; *b:* Prothero and Schwab, 2004; *c:* Boggs, 1995; *d:* Ritter *et al.*, 2002; *e:* Colella *et al.*, 1987; *f:* White, 1992

2. Figures

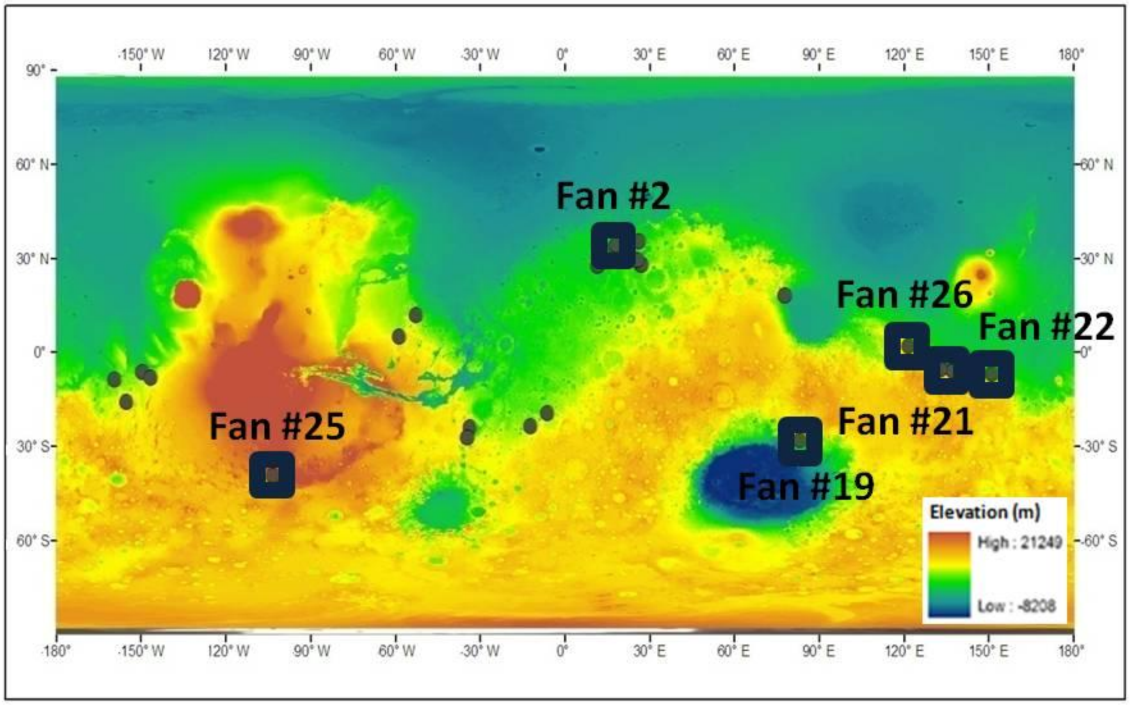

Figure 1: Global map of Mars showing the locations of the 33 deposits (gray dots) discussed by Irwin *et al.* (2005). Boxes and names show respective locations of deposits focused on in this study (MOLA elevation Base map).

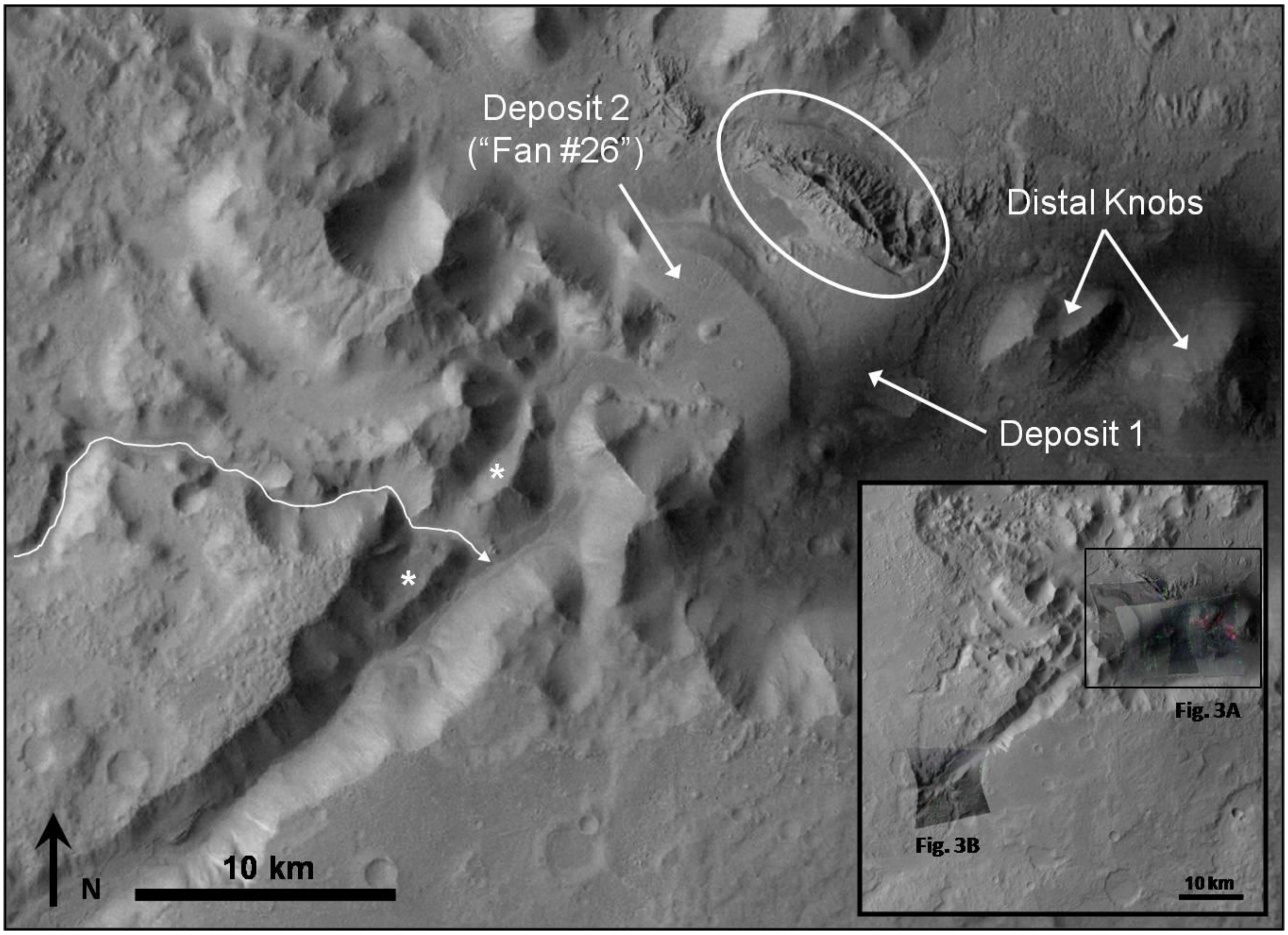

Figure 2: Portion of HRSC image H5212_0000 _ND4 showing area of Fan #26 located in the Nepenthes Mensae region, as well as the inlet valley, superposed deposit ("Deposit 1"), and distal knobs. Curvilinear arrow shows the path of tributary channel. Asterisks and oval show the locations (respectively) of hypothesized fluvial terraces and an elongate feature hypothesized to be a fissural volcano by de Pablo and Pacifici (2008). Inset shows regional context with associated CRISM images overlain (Figure 3A and Figure 3B).

Figure 3: A) CRISM phyllosilicate summary parameters(R: DB2300, G: 2210, B: BD1900) of data on/near Fan #26 overlain on grayscale HRSC image H5212_0000 _ND4. Red/magenta regions represent locations containing Fe/Mg-phyllosilicates, and green regions represent locations containing Al-phyllosilicates. The colored arrows show locations of the normalizing spectra used in spectral ratios in Figure 4A (arrow colors correspond to respective spectra). CRISM images in this figure are (from left to right) FRT1D7F0, FRT16525, and FRT147E0. B) CRISM phyllosilicate summary parameters overlain on IRB grayscale of CRISM image FRT16026 showing watershed and inlet valley of Fan #26 (circle shows location of normalizing spectra in spectral ratio). C) RGB composite of visible-wavelength CRISM summary parameters highlighting locations of oxidized iron minerals (R: BD530, G: SH600, B: BDI1000); areas abundant in dust appear red/orange/yellow in color, green colors primarily represent rocks with coatings/rinds on the surface, and blue colors represent areas bearing iron minerals (*e.g.*, olivine and pyroxene). All visible-wavelength CRISM summary parameter figures in this manuscript are stretched the same (R: 0.0000 – 0.1700, G: 0.1000 – 0.1700, B: 0.0000 – 0.0250) for qualitative comparison. D) CRISM summary parameters highlighting diversity in mafic minerals (R: OLINDEX, G: LCPINDEX, B: HCPINDEX) for data over Fan #26; magenta areas in right two images correspond with pyroxene-bearing sand dunes.

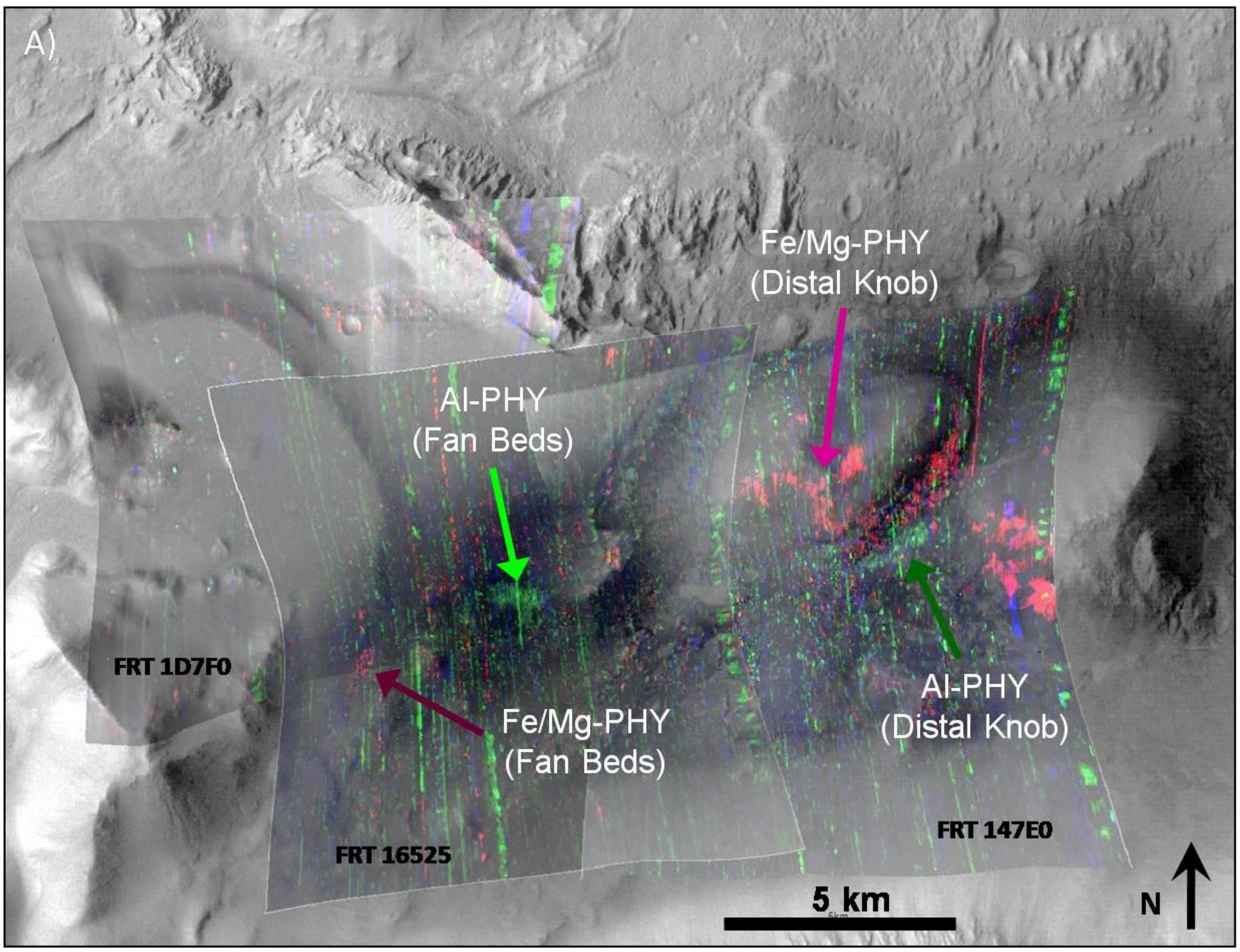

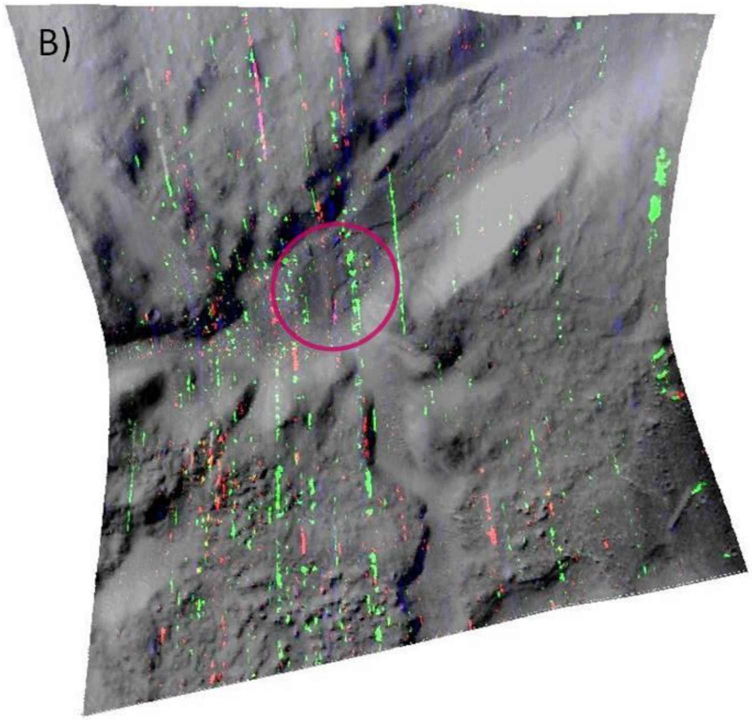

Figure 3B

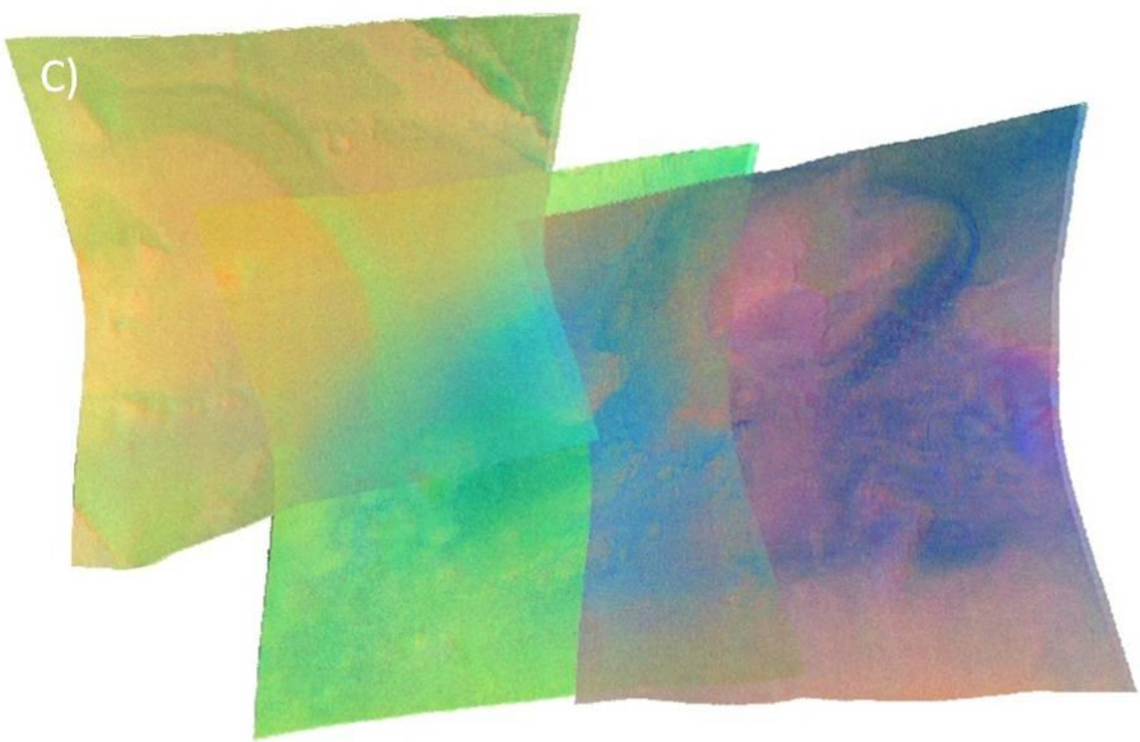

Figure 3C

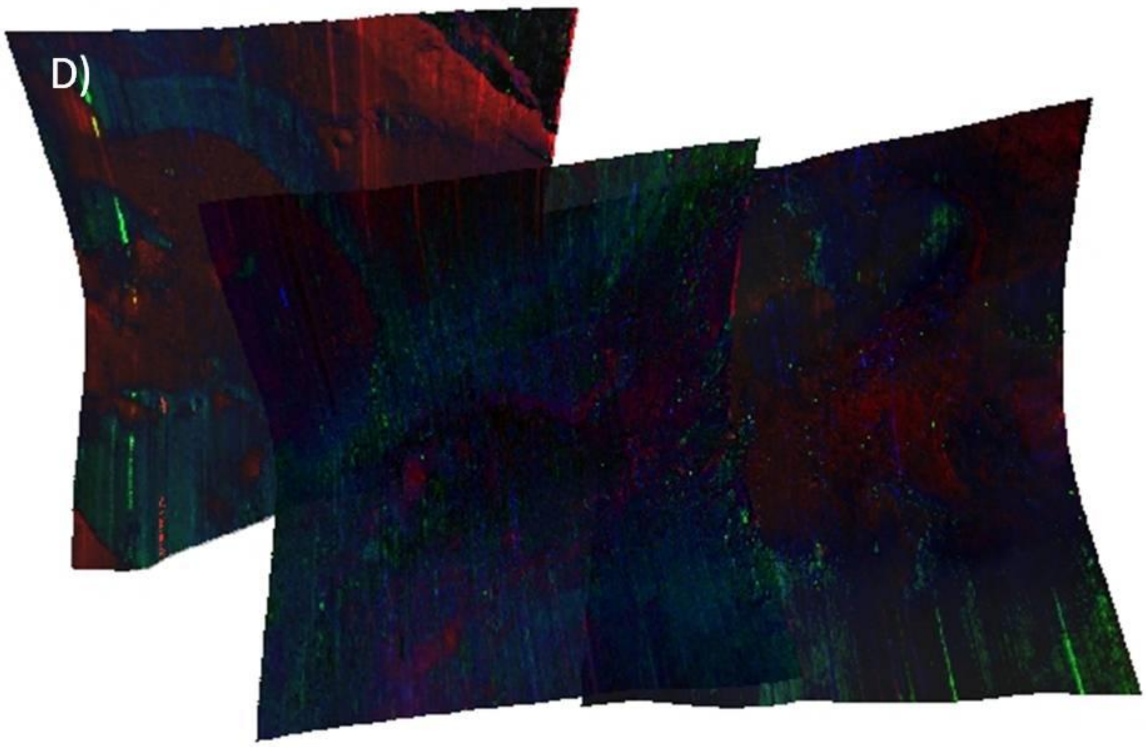

Figure 3D

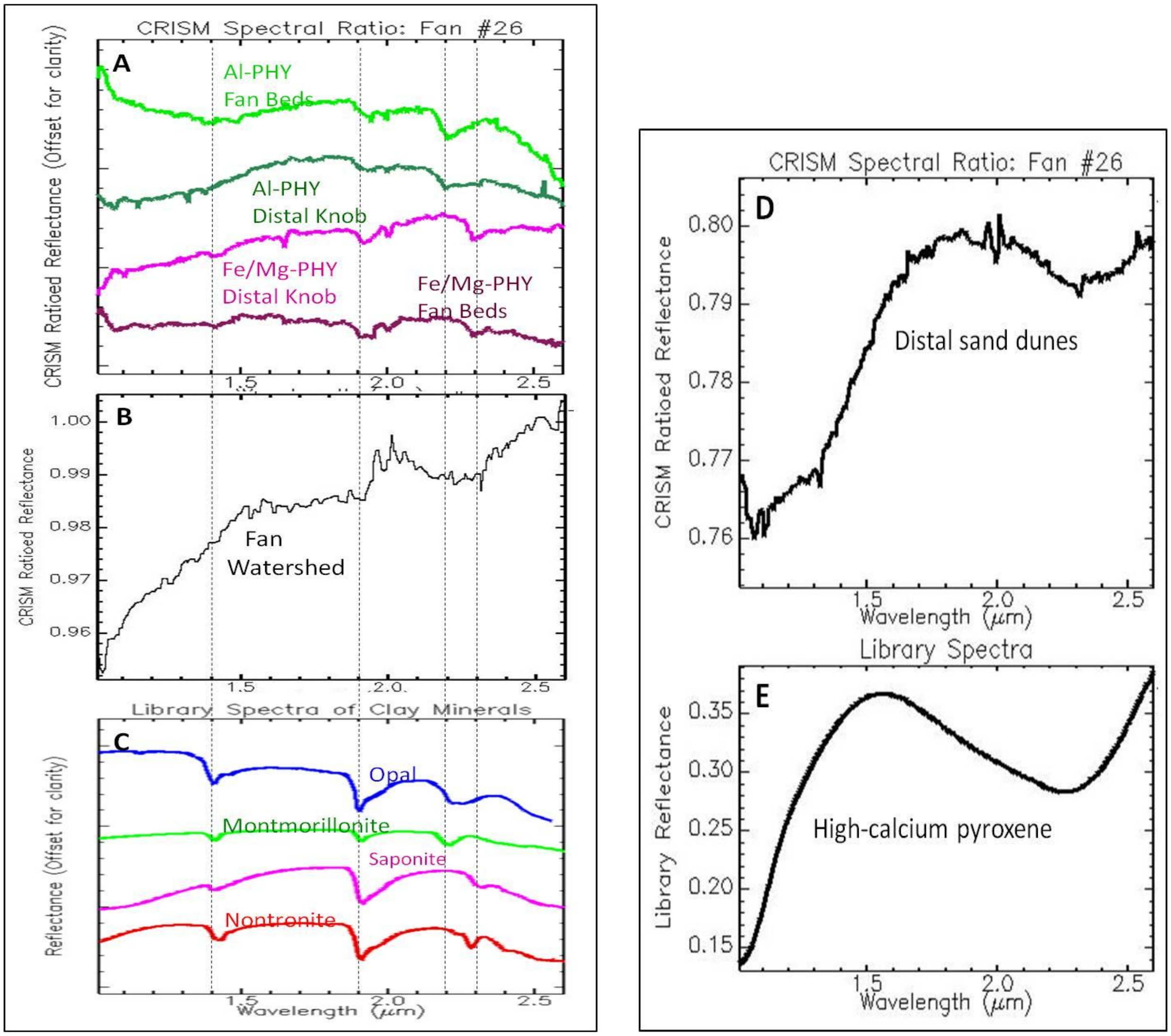

Figure 4: A) CRISM ratio spectra of Fe/Mg and Al-phyllosilicates in lower beds of, and on elevated knob distal to Fan #26. Absorption features of Fe/Mg-phyllosilicates are indicative of Fe/Mg-smectite, perhaps saponite and/or nontronite; absorption features of Al-phyllosilicates are indicative of Al-smectite, perhaps montmorillonite. The broadened spectra of Al-phyllosilicates may be due to mixing with hydrated silica, such as opal. B) CRISM ratio spectra of the inlet valley within watershed upstream of Fan #26 (FRT16026), showing absorption features consistent with phyllosilicates and pyroxene. C) Library reflectance spectra of saponite, nontronite, montmorillonite, and opal (hydrated silica). D) Ratio spectrum of pyroxene-bearing sand dunes distal to fans, and E) library spectrum of pyroxene for comparison.

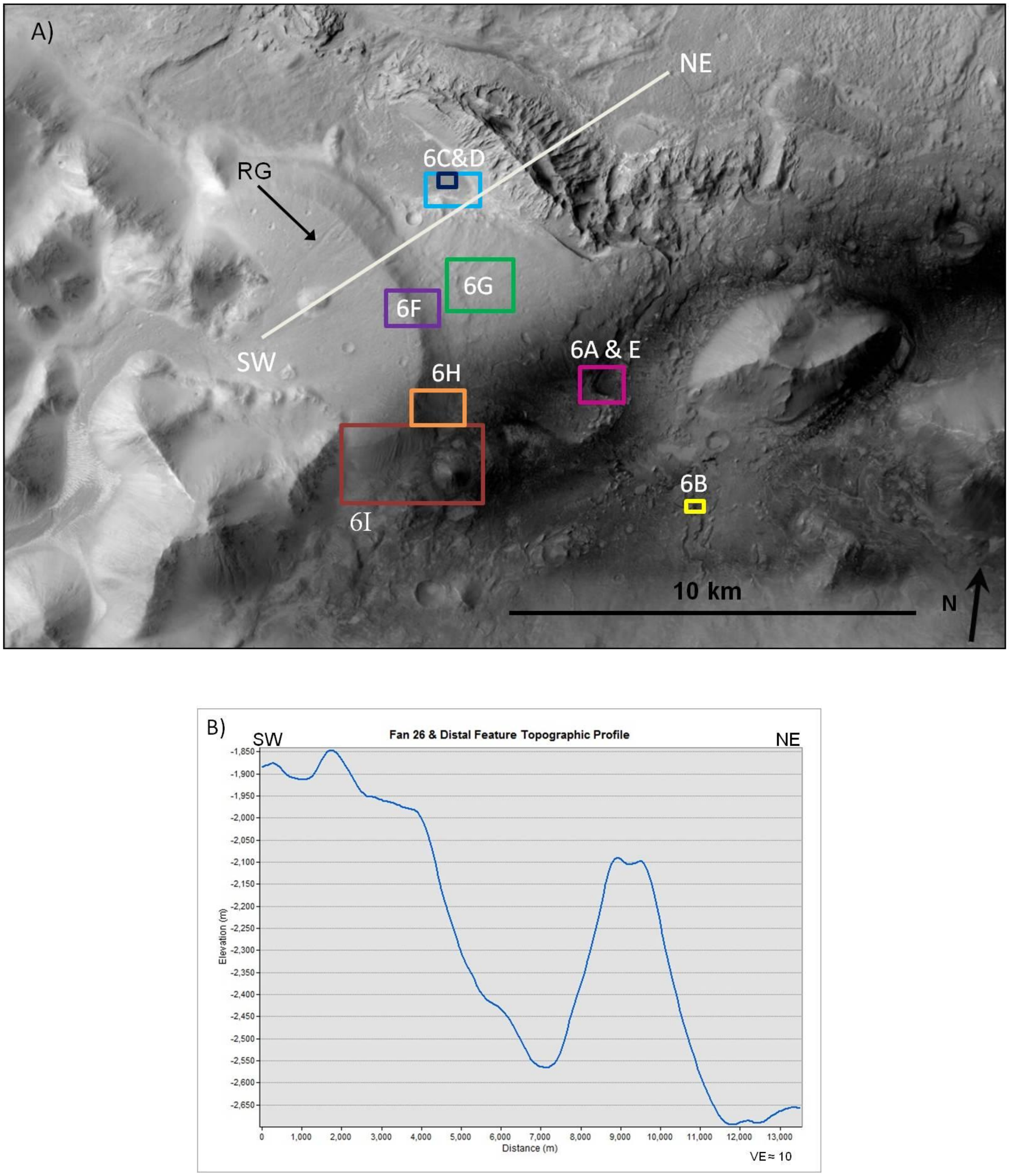

Figure 5: A) Portion of CTX image B16_015980_1821_XN_02N238W showing Fan #26, stratigraphically superposed deposit, and nearby region. Boxes show the locations of images in Figure 6, and black arrow labeled 'RG' points to example of radially-oriented gullies on the fan surface. B) Topographic profile of Fan #26, superposed deposit, and elongate depression distal to deposits.

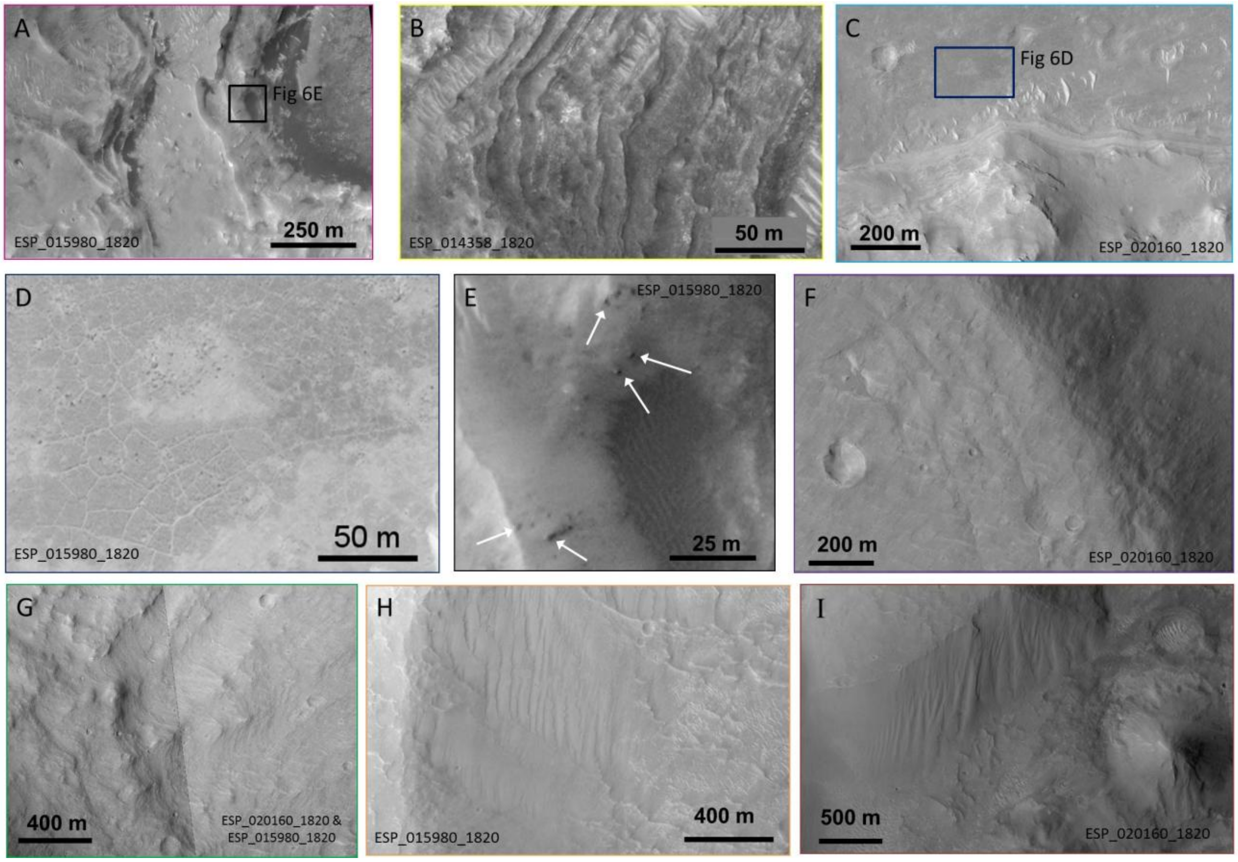

Figure 6: Portions of HiRISE images showing morphologies on/near Fan #26, superposed deposit, and surrounding area. A), B), & C) show fine-scale layering in beds of the supposed deposit; D) polygonally fractured terrain distal to Fan #26; E) distal fan beds eroding boulder-sized clast inclusions (white arrows pointing to some); F) concentric rings on the surface of fan #26, with layering exposed between rings; G) layering in lower beds of Fan #26, cross-cut by radially-oriented gullies; H) Parallel linear features (possibly layering) exposed on fan scarp; I) parallel features that cross-cut southern fan scarp at a steep angle, and features of similar size/orientation on the southern side of a distal fan mound - likely aeolian in origin. HiRISE image numbers are shown in figures; north is toward the top of images.

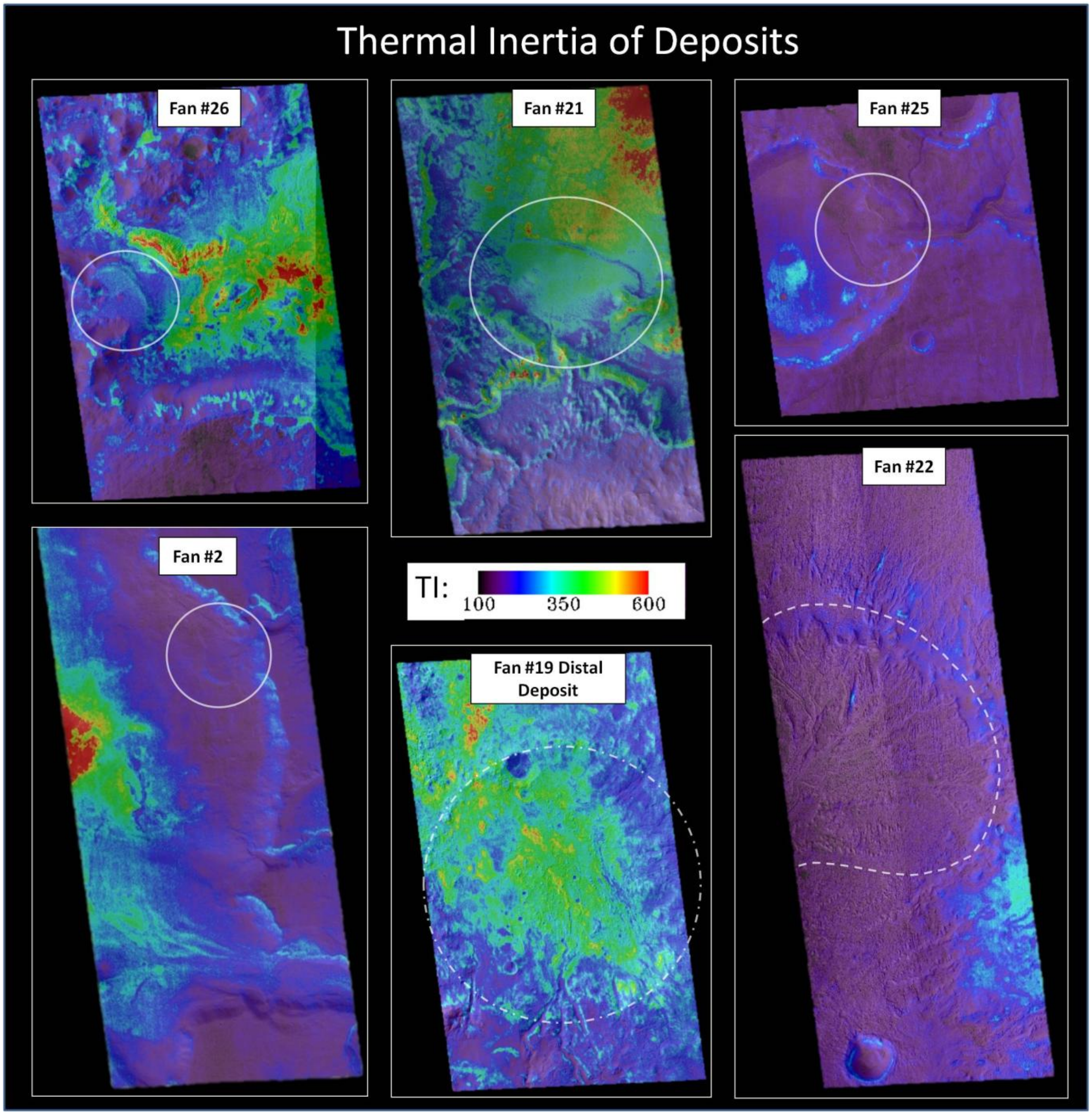

Figure 7: THEMIS thermal inertia of phyllosilicate-bearing deposits in this study (TI units are in J m^{-2} K^{-1} $s^{-1/2}$) overlain on HRSC grayscale images (Fans #2, #21, #25, and #26) or CTX data (Fans #22 and #19 Distal Deposit). Solid white circles show locations of deposits, dashed circle on Fan #19 Distal Deposit approximately outlines degraded rim of crater containing the deposit, and dashed outline over Fan #22 shows approximate distal boundaries of this deposit. North is toward the top, and the width of each scene is 32km. Scene numbers of THEMIS night IR images from which these maps were derived (as well as HRSC data) are provided in Table 1.

Figure 8: A) CRISM summary parameters (R: DB2300, G: HCPINDEX, B: BD1900) of multiple targeted scenes in Ismenius Cavus, crater containing Fan #2, overlain on HRSC image with 100m elevation contours. Magenta areas represent locations bearing phyllosilicates, and green regions bear pyroxene. Black box shows locations of Figure 10 and Figure 11A. B) Portion of HiRISE image PSP_010419_2140 showing horizontally layered, polygonally fractured phyllosilicate-bearing region in the center of Ismenius Cavus crater (north is toward the top of image). C) CRISM visible-wavelength summary parameters of oxidized iron minerals (R: BD530, G: SH600, B: BDI1000) for data in Ismenius Cavus crater (overlain on HRSC data); areas abundant in dust appear orange-yellow in color (data stretch same as Figure 3C).

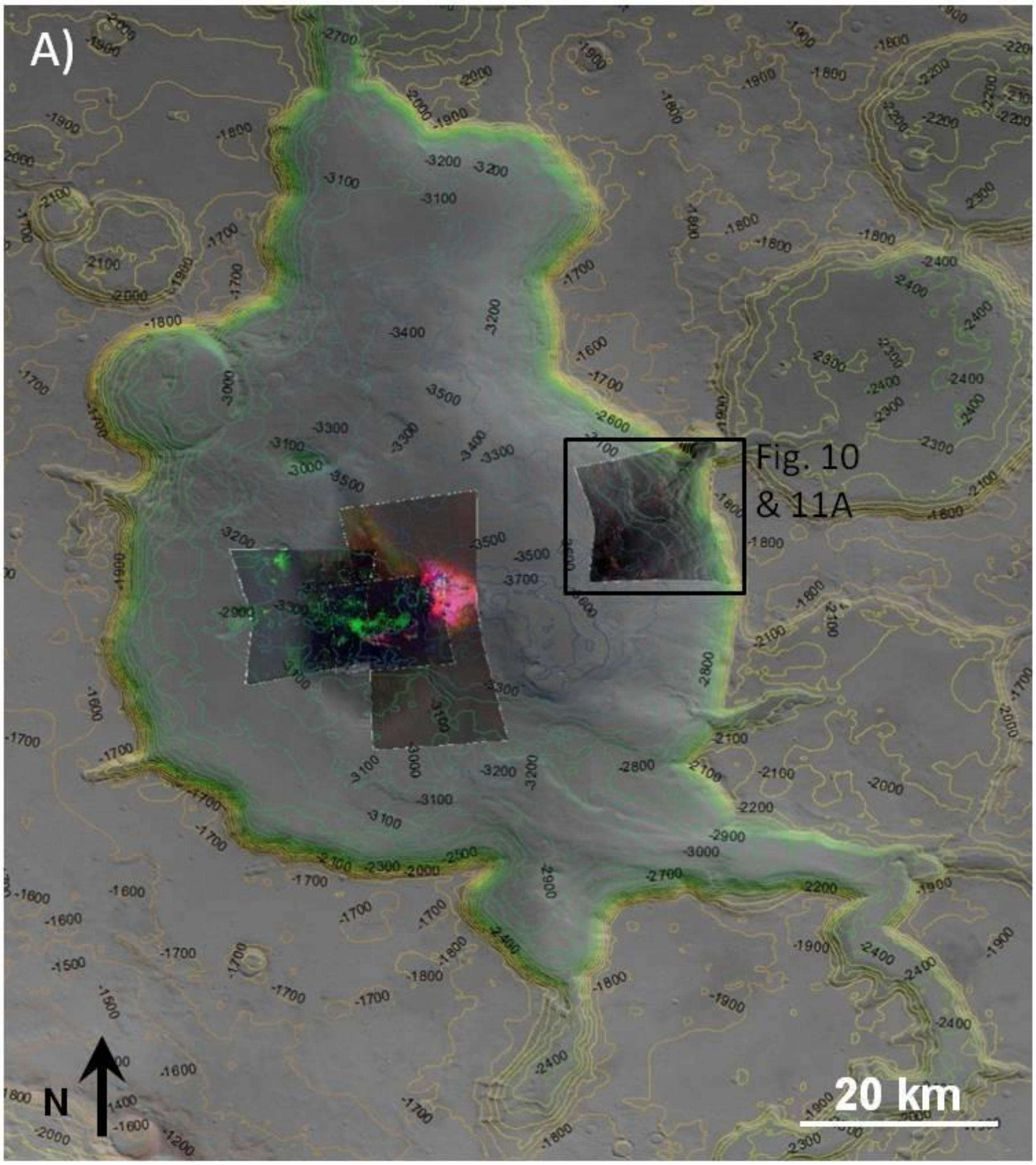

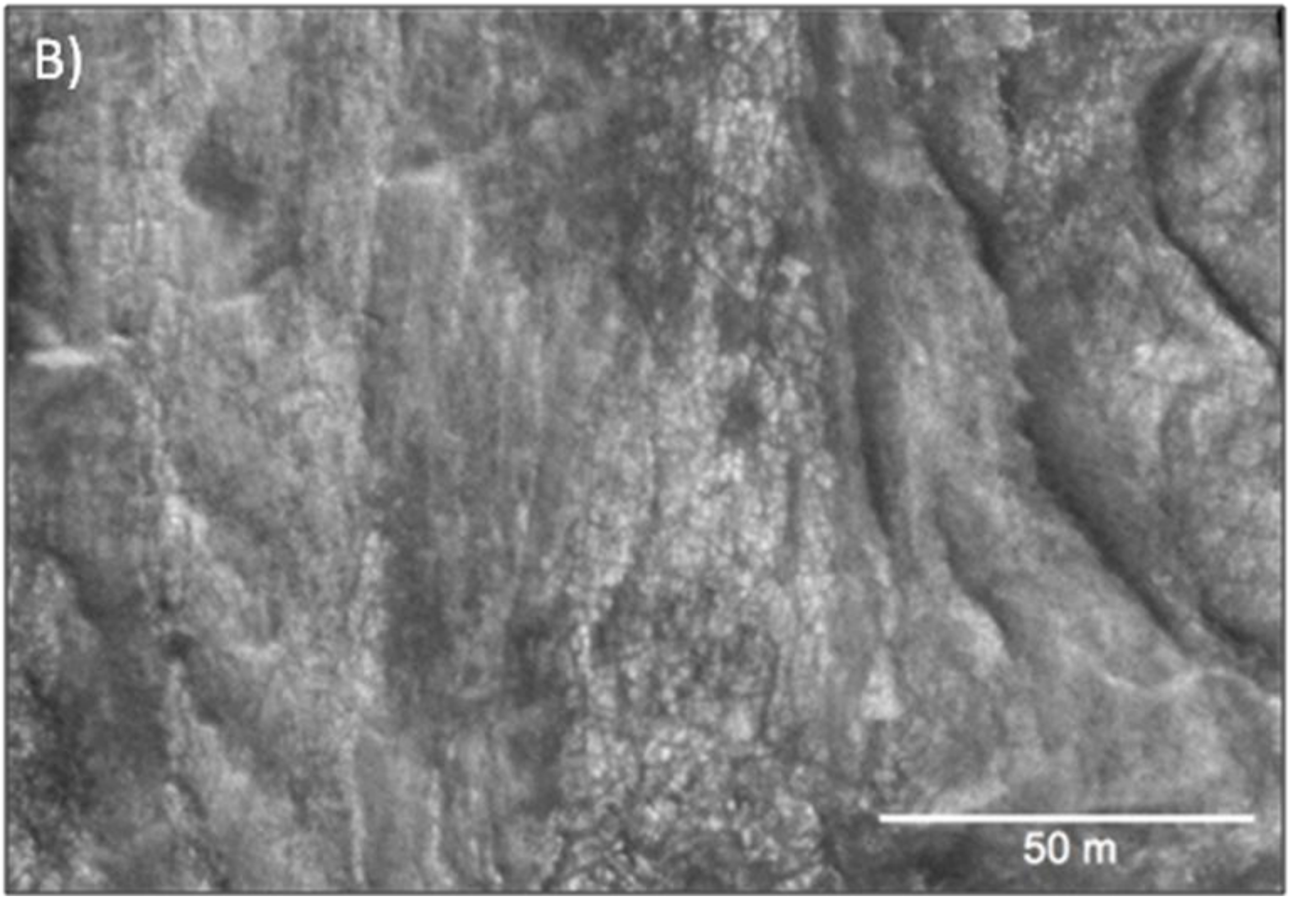

Figure 8B

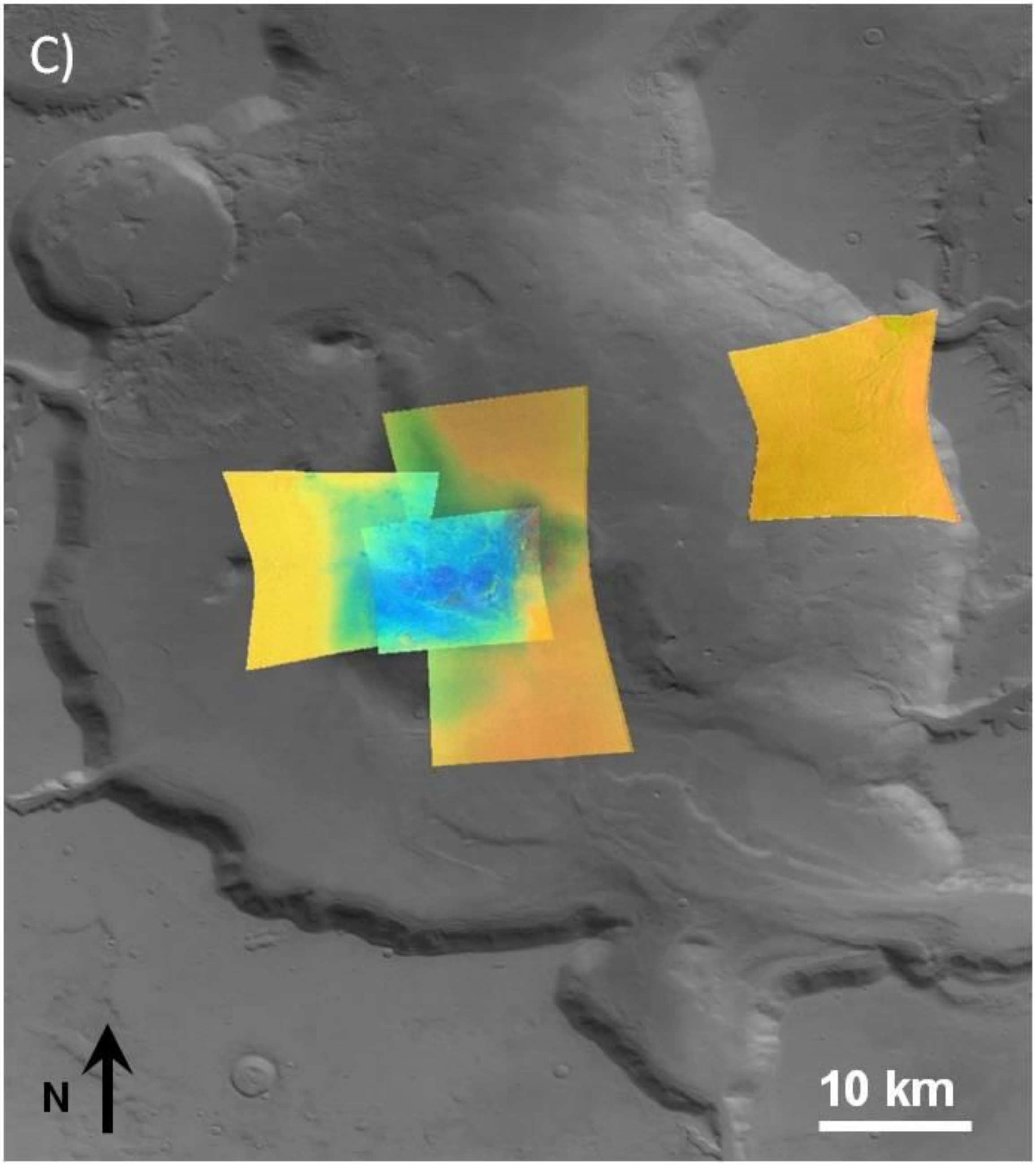

Figure 8C

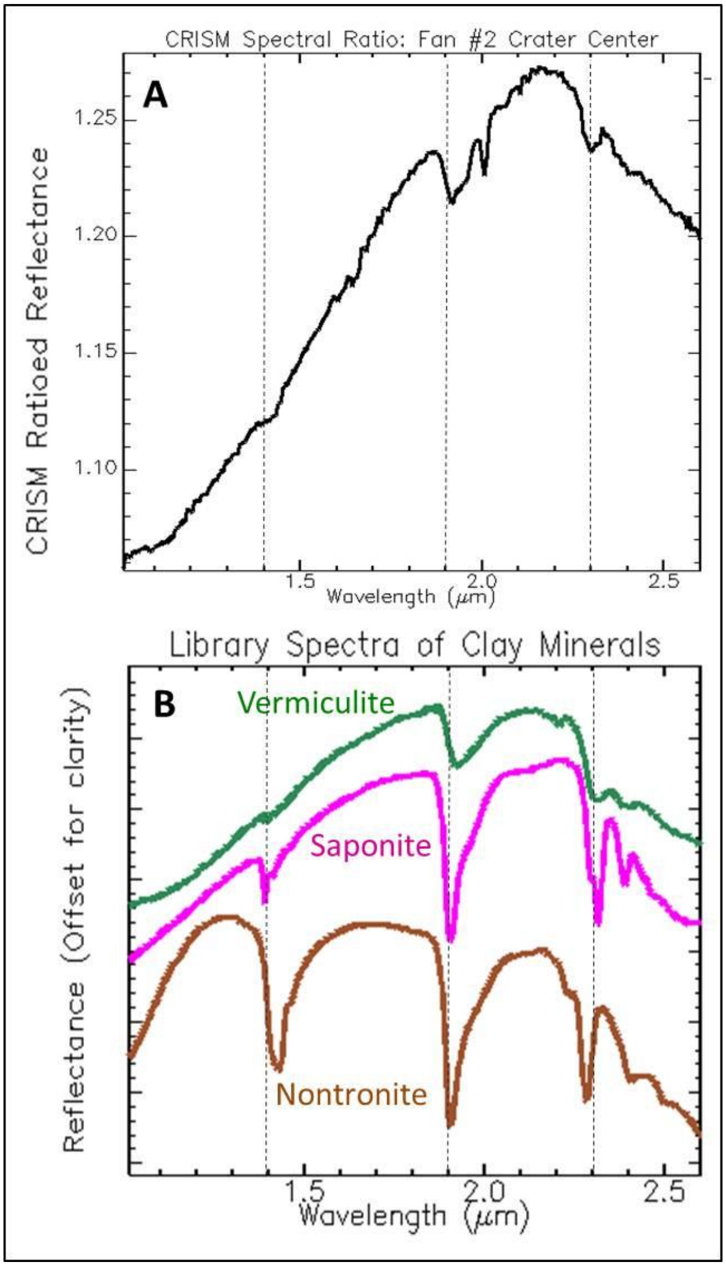

Figure 9: A) CRISM ratio spectrum of Fe/Mg-phyllosilicates in the center of Ismenius Cavus crater, basin containing Fan #2. Absorption features are consistent with an Fe/Mg-smectite, perhaps nontronite. B) Library reflectance spectra of nontronite, saponite, and vermiculite for comparison.

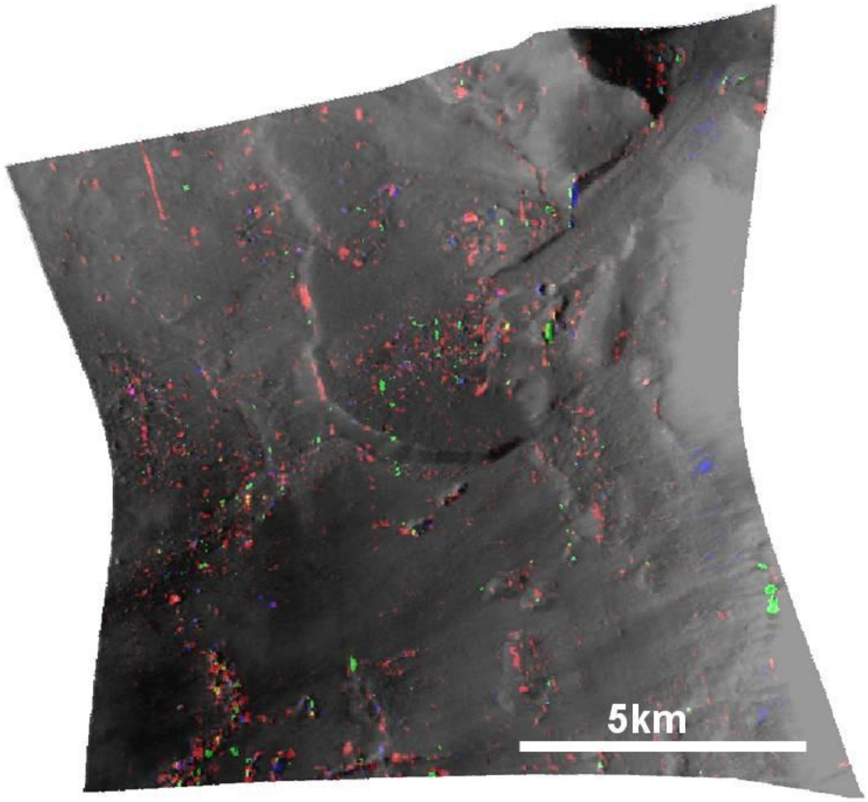

Figure 10: CRISM image FRT00019B14 of phyllosilicate summary parameters (R: DB2300, G: 2210, B: BD1900) overlain on grayscale image, showing locations of possible presence of phyllosilicates (red/magenta regions) that are consistent with geomorphology on the surface of, and distal to Fan #2.

Figure 11: A) Portion of CTX image P20_008929_2143_XN_34N342W showing large-scale morphology of Fan #2. Boxes show locations of images in Figure 12; B) Topographic profile of inlet valley terminating in Fan #2 (location not shown in Figure 11A); C) Topographic profile of Fan #2.

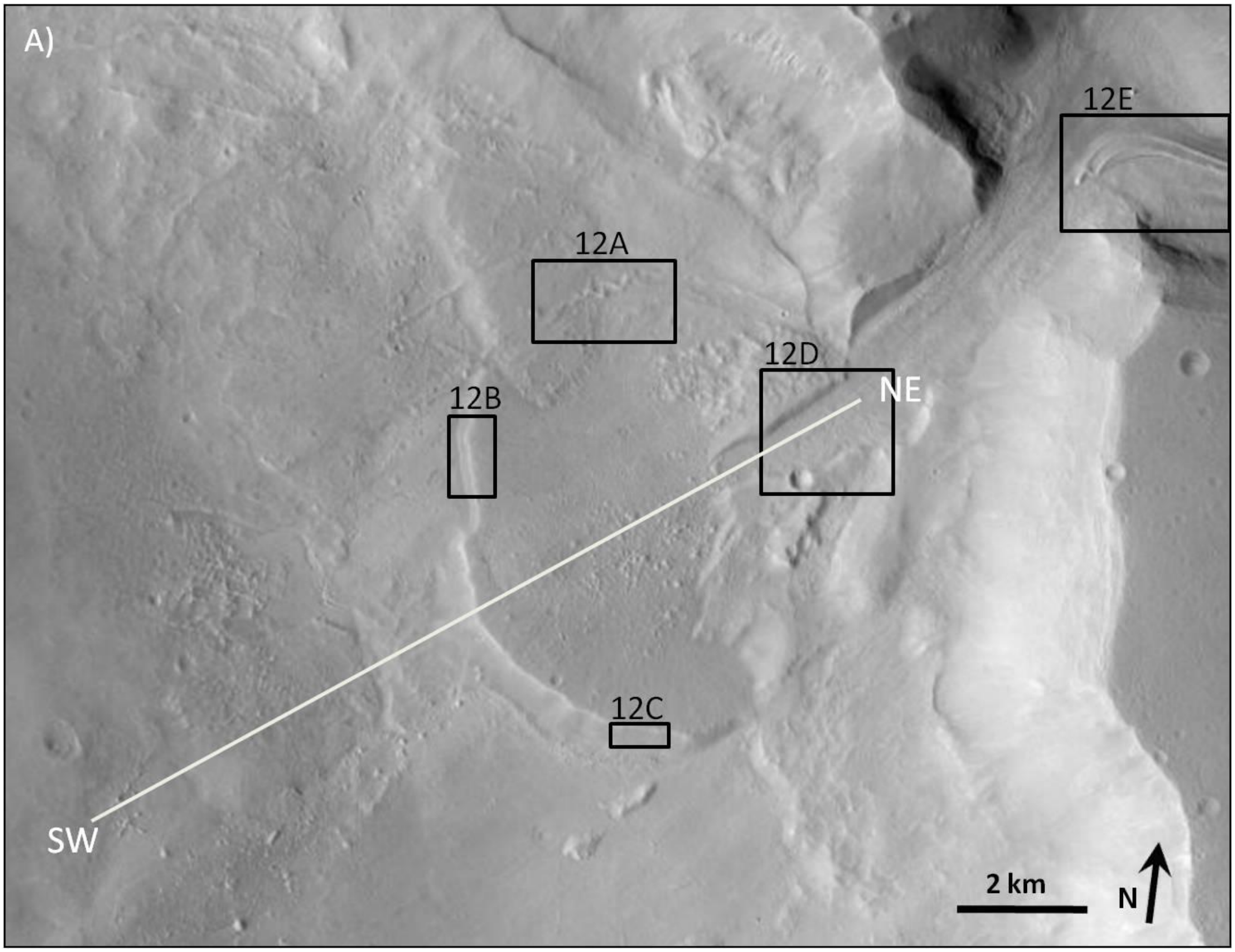

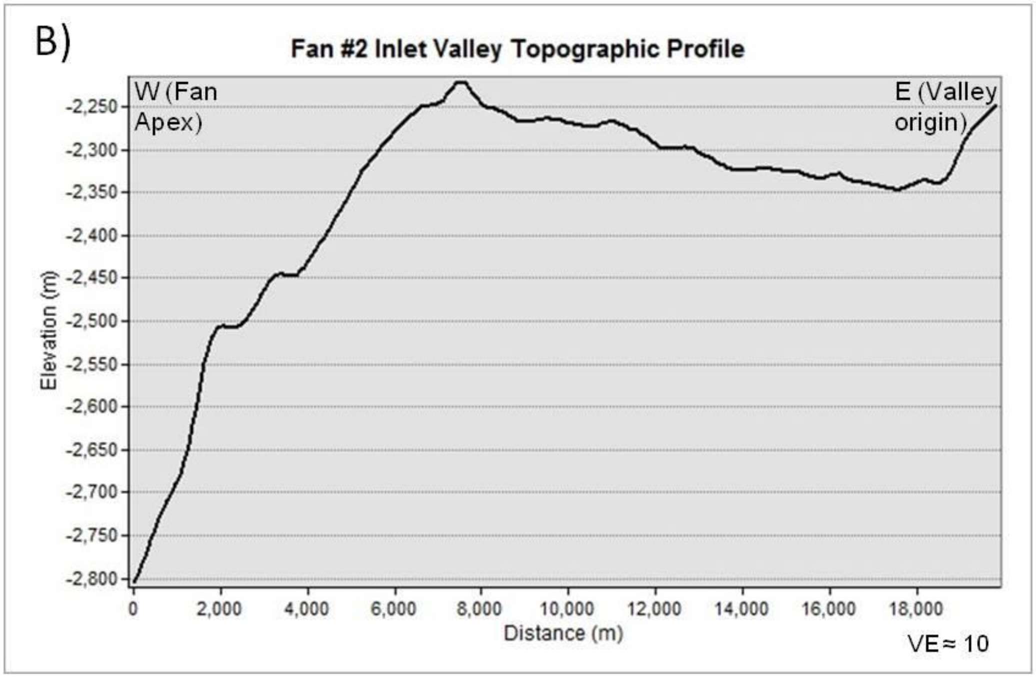

Figure 11B

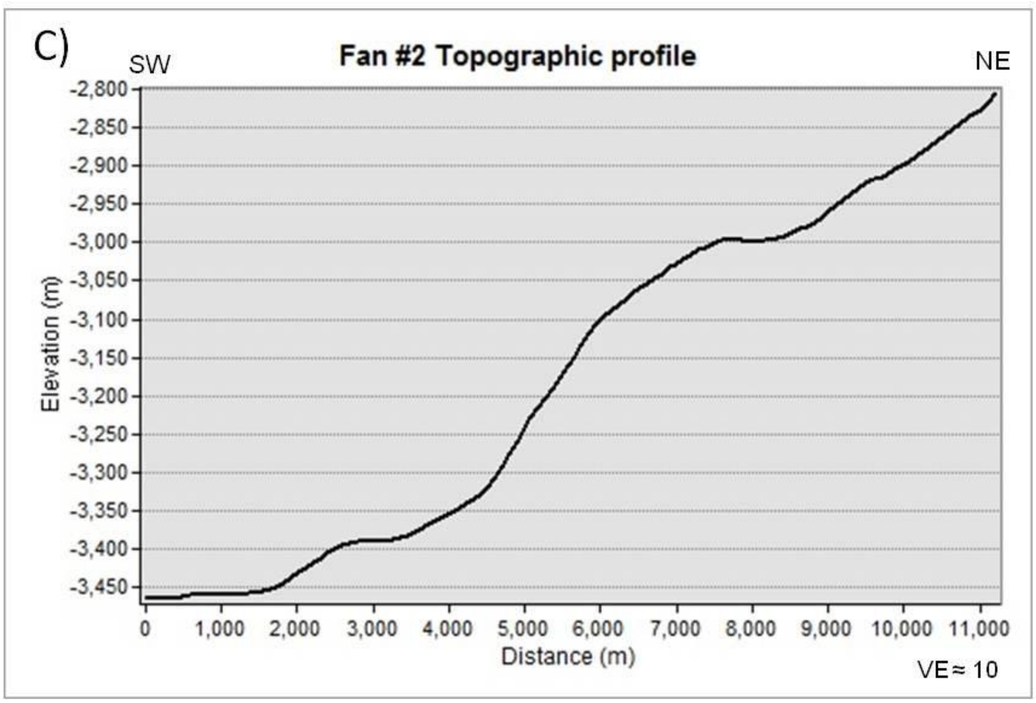

Figure 11C

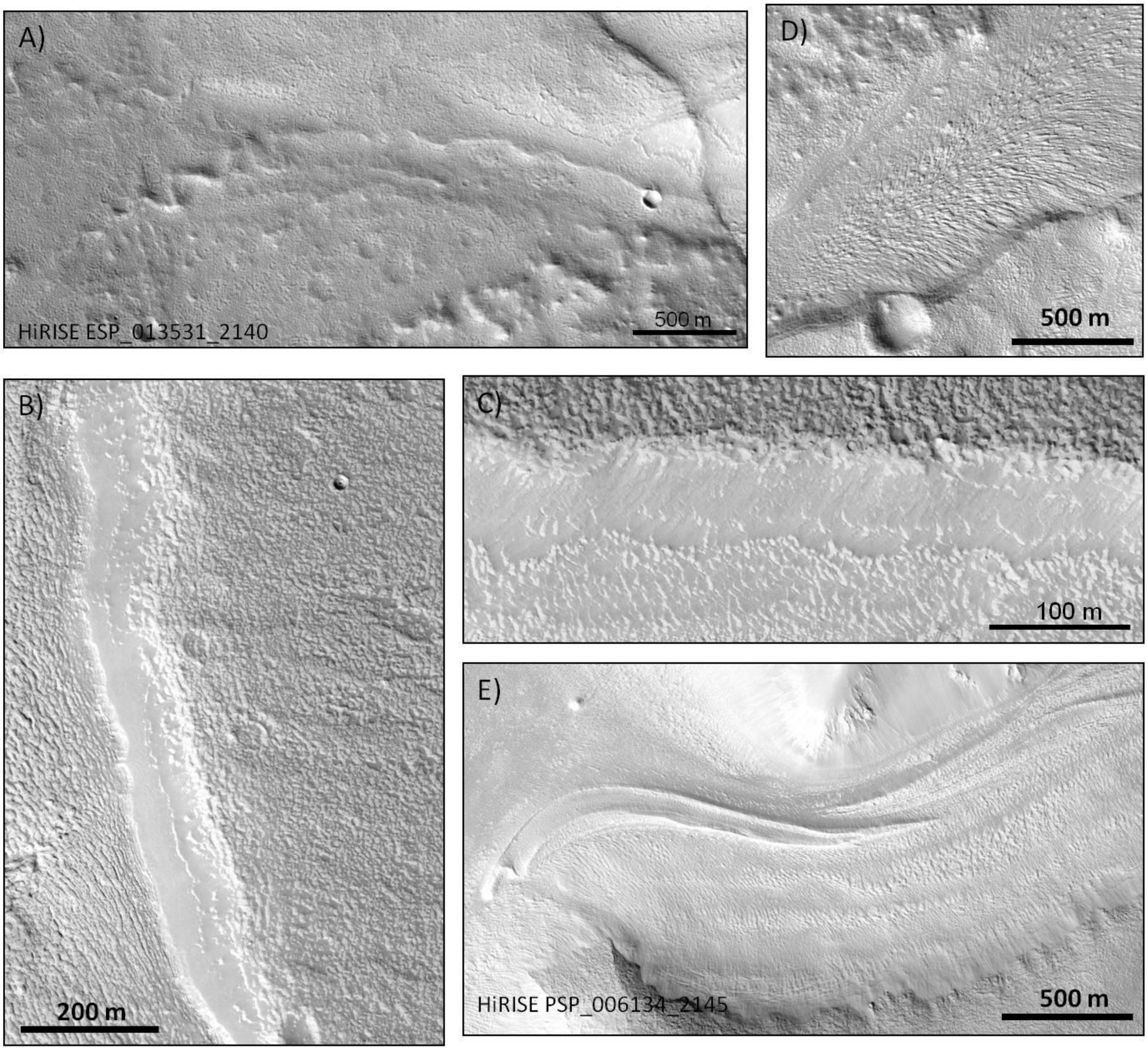

Figure 12: Small scale morphologies on/near Fan #2. A) Sinuous-ridge features on surface of deposit superposed deposit; B) sub-horizontal planar features exposed on fan scarp, and pitted terrain on fan surface; C) steeply dipping features on fan scarp; D) previously hypothesized glacial terrain in the fan inlet valley resembling terrestrial rock glacier morphologies, including lineated valley fills, lobate debris aprons, and pitted textures; E) curvilinear ridge features on the floor of Fan #2 inlet valley.

Figure 13: A) HRSC grayscale image of Fan #21 with CRISM phyllosilicate summary parameters (R: DB2300, G: 2210, B: BD1900) overlain showing locations of phyllosilicates. Red/magenta regions represent locations containing Fe/Mg-phyllosilicates; inset shows Fan #21 with no CRISM overlay. B) Regional context of Fan #21 (HRSC visible data on THEMIS day-time IR basemap) with CRISM data (showing phyllosilicate summary parameters) overlain; dashed line shows approximate boundaries of watershed and solid line traces out inlet valley from watershed to deposit. C) and D) Phyllosilicate summary parameters overlain on grayscale CRISM data (FRT17CCB and FRTB001, respectively) in the watershed. E) CRISM visible-wavelength summary parameters of oxidized iron minerals (R: BD530, G: SH600, B: BDI1000) for data on Fan #21; areas abundant in dust appear orange-yellow (data stretch same as Figure 3C). F) CRISM summary parameters highlighting diversity in mafic minerals (R: OLINDEX, G: LCPINDEX, B: HCPINDEX) for data over Fan #21; green and blue regions show differences between spatial locations of low- and high-calcium pyroxene, respectively.

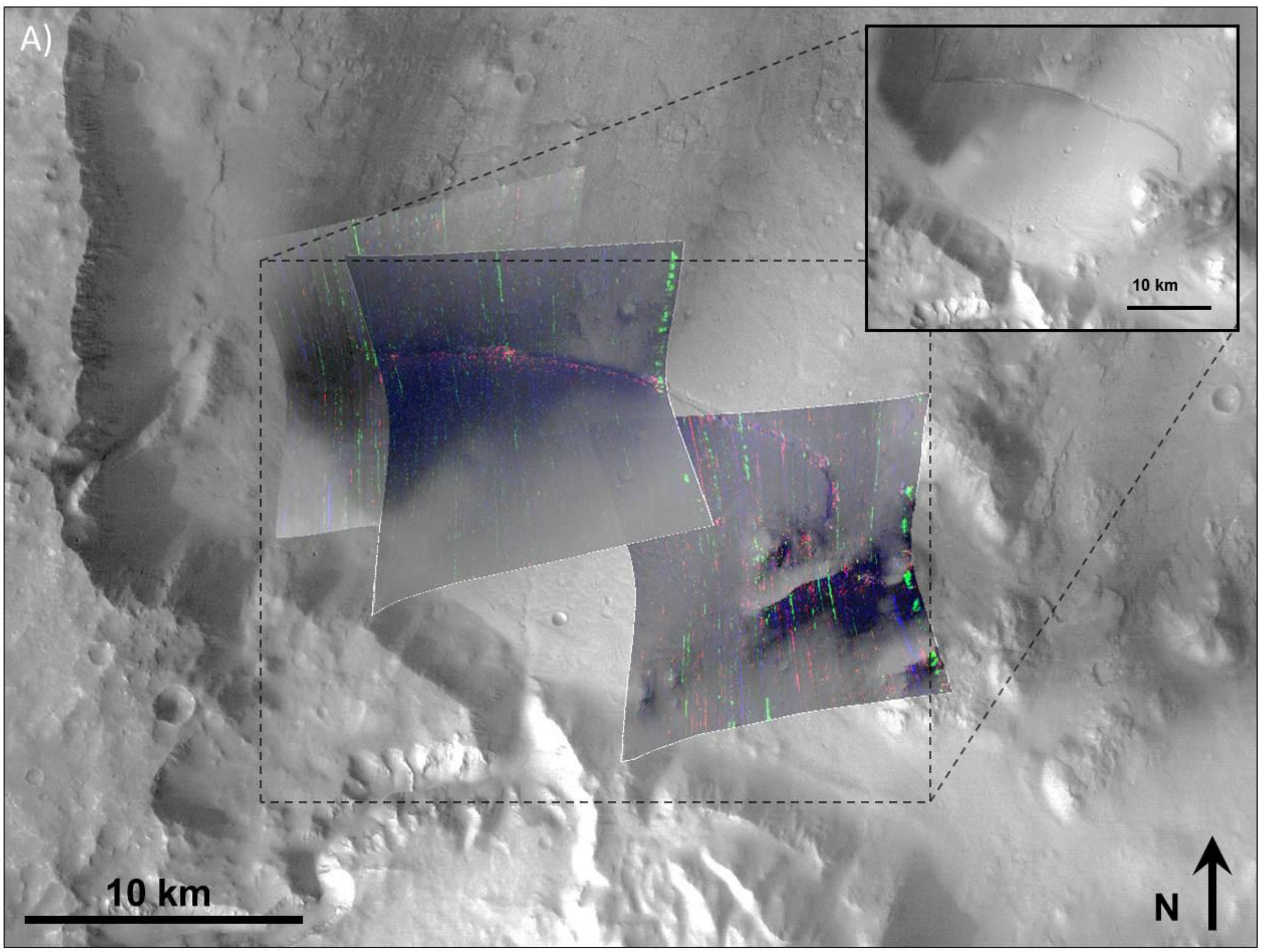

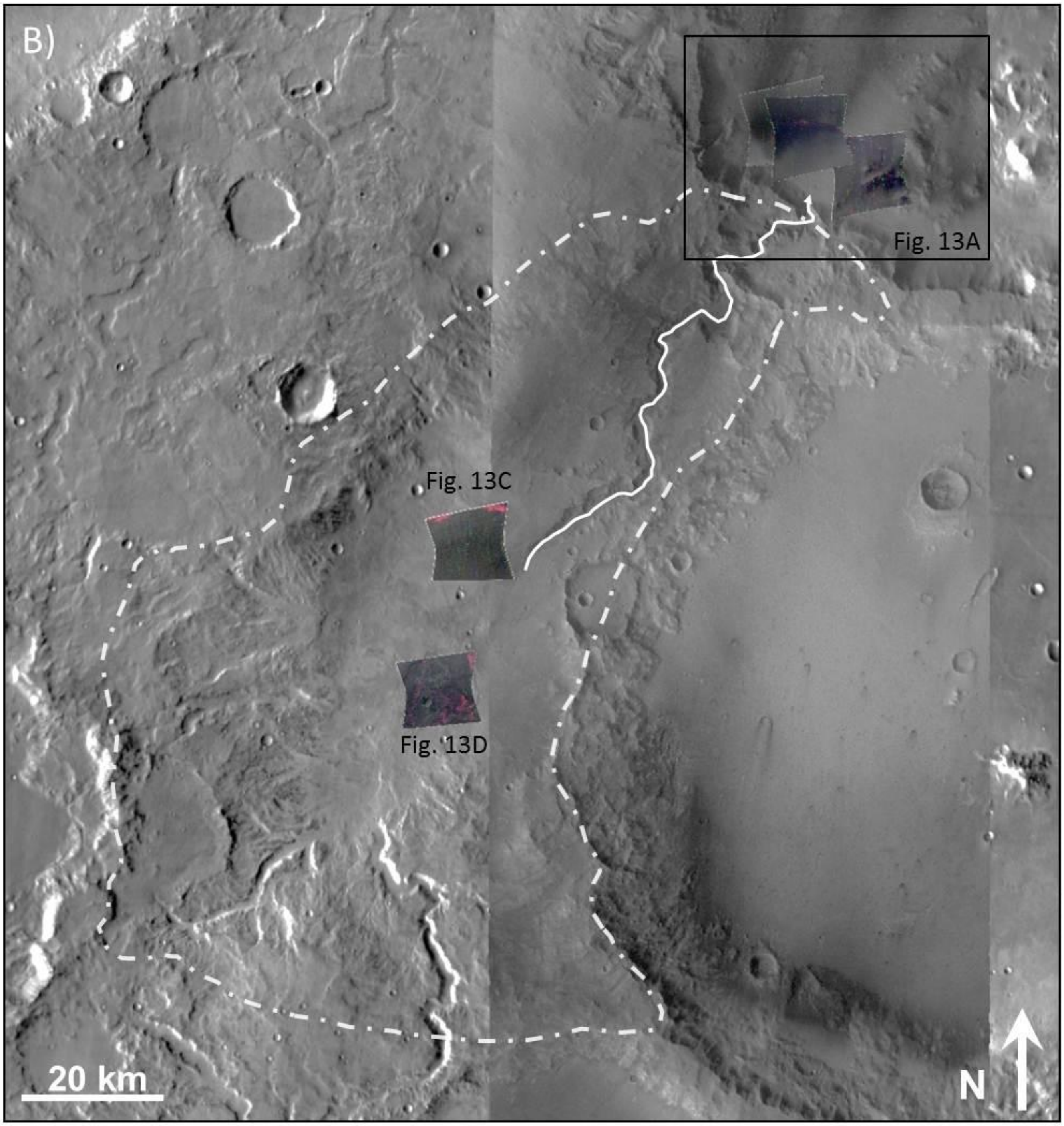

Figure 13B

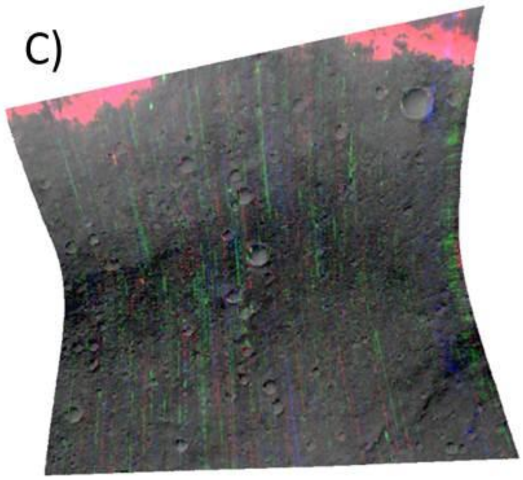

Figure 13C

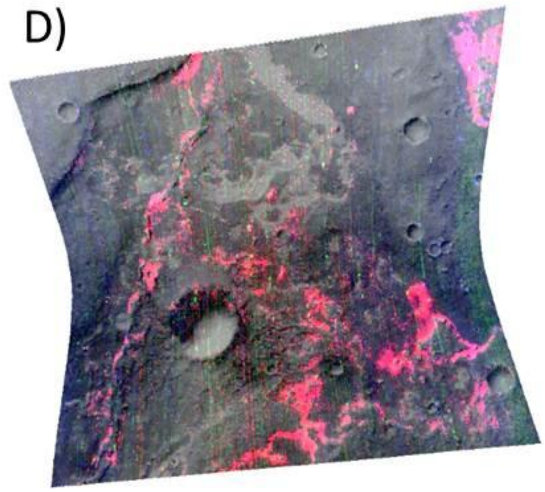

Figure 13D

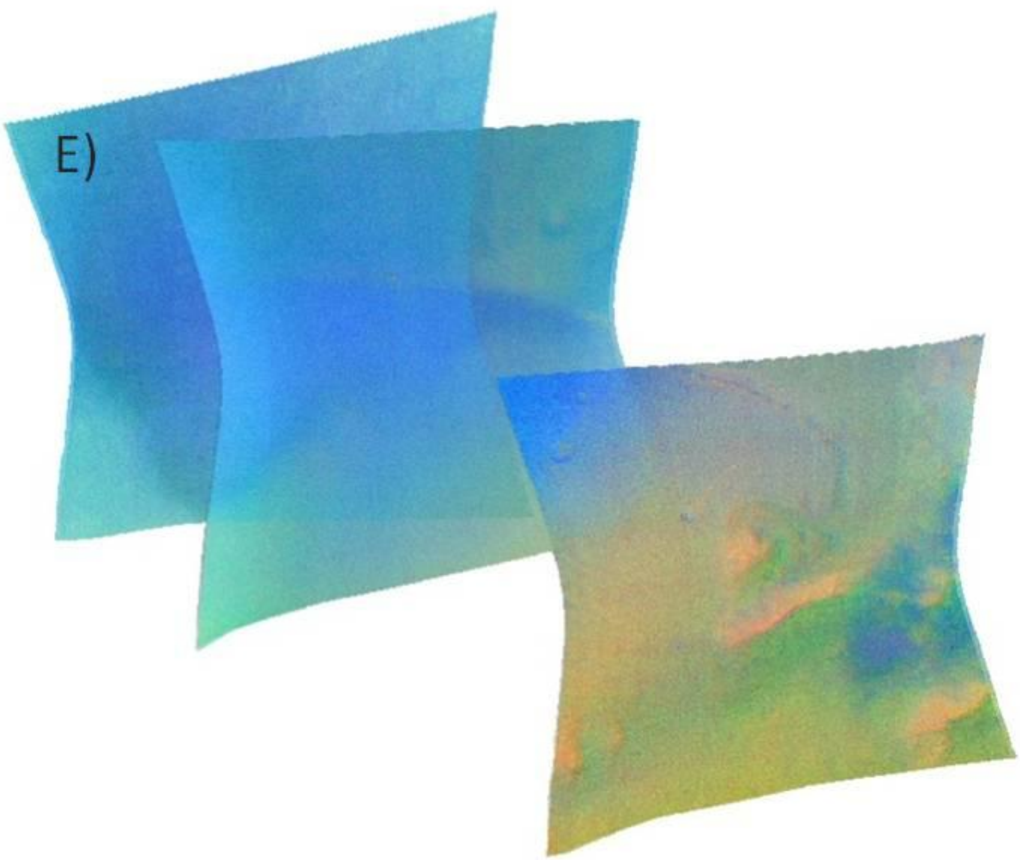

Figure 13E

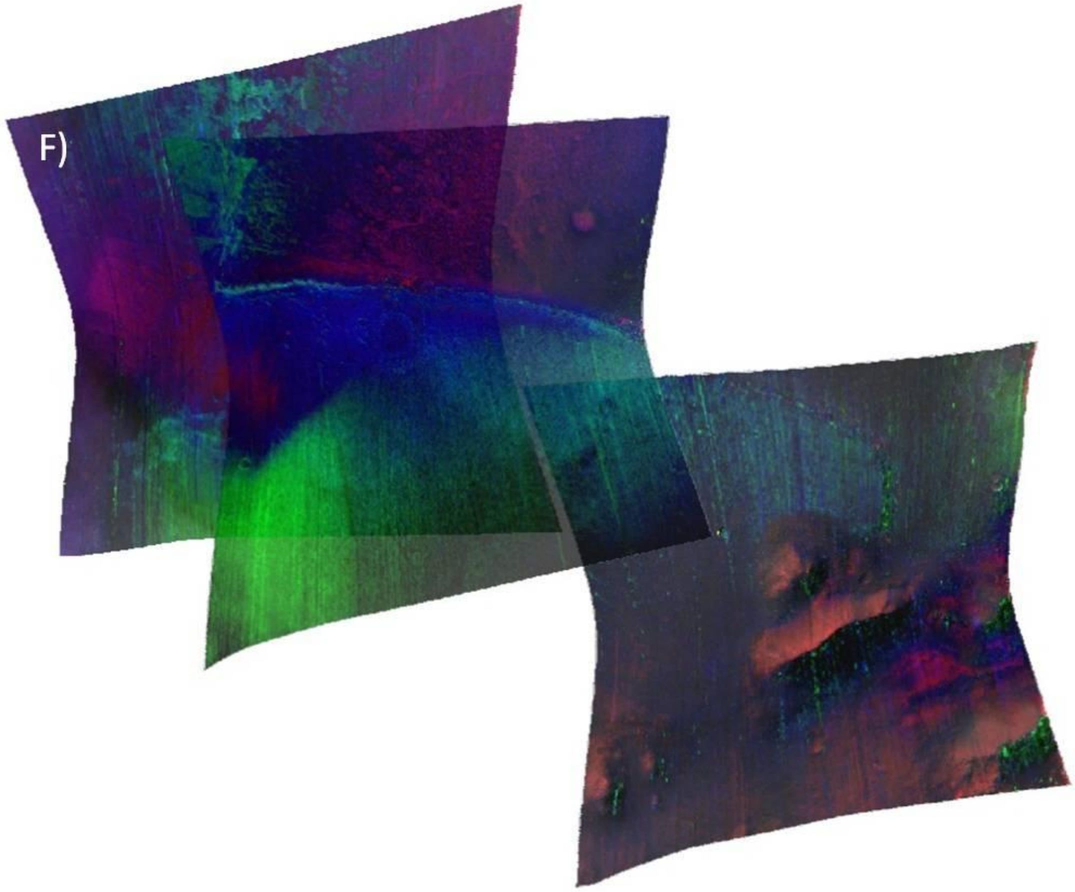

Figure 13F

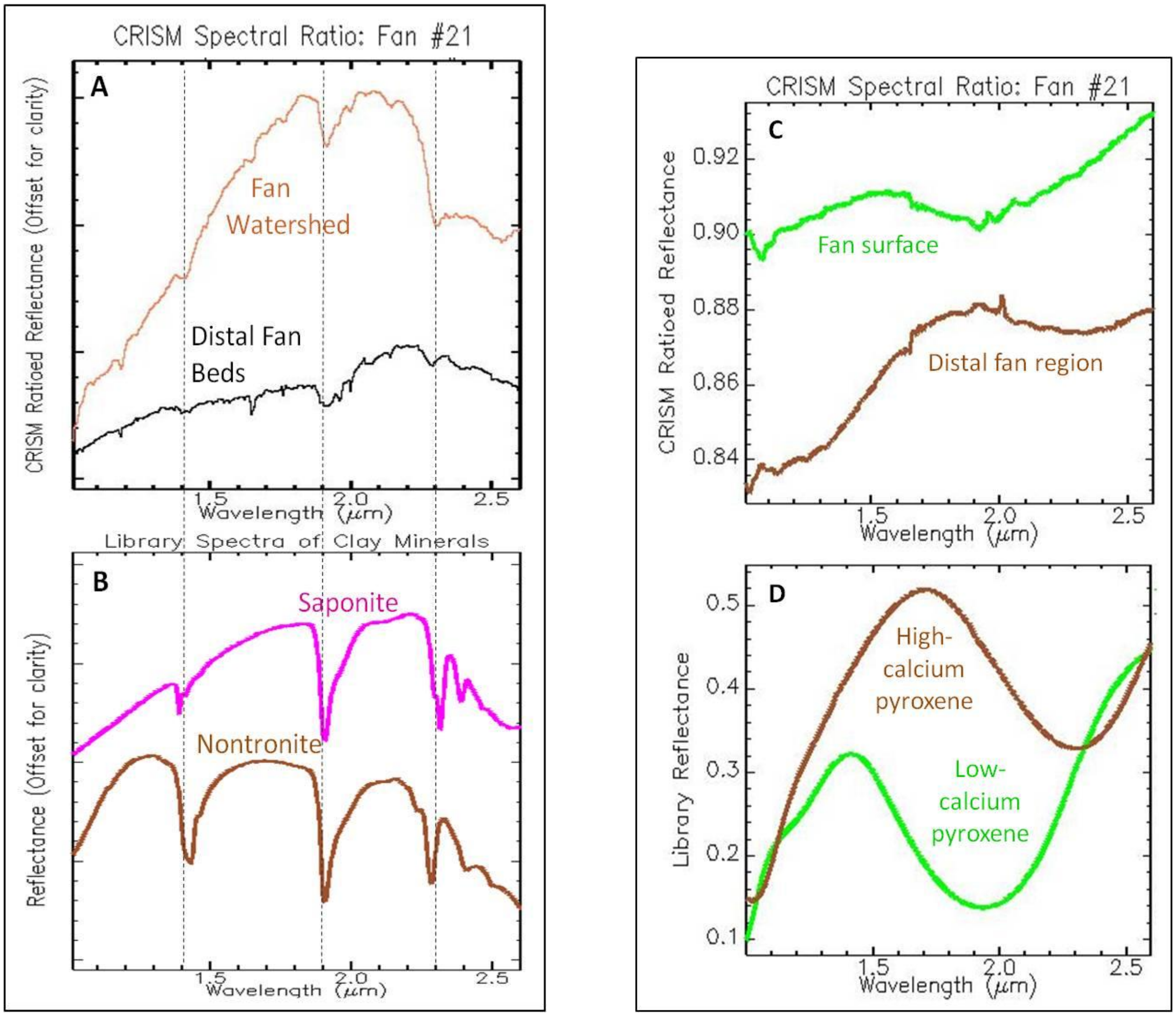

Figure 14: A) CRISM ratio spectrum of Fe/Mg-phyllosilicates in the lower beds and upstream watershed of Fan #21. Absorption features are most consistent of an Fe/Mg-smectite, likely nontronite and/or saponite. B) Library reflectance spectra of nontronite and saponite for comparison. C) Spectra on and distal to Fan #21 displaying absorption features consistent with low- and high-calcium pyroxene. D) Library spectra of pyroxene for comparison.

Figure 15: A) Portion of HRSC image H1982_0000 over Fan #21 with 100m elevation contours. White line shows location of topographic profile in B). C) & D) are portions of HiRISE image ESP_19975_1750 showing exposed layered variations in tonality in high albedo phyllosilicate-bearing regions of the fan scarp.

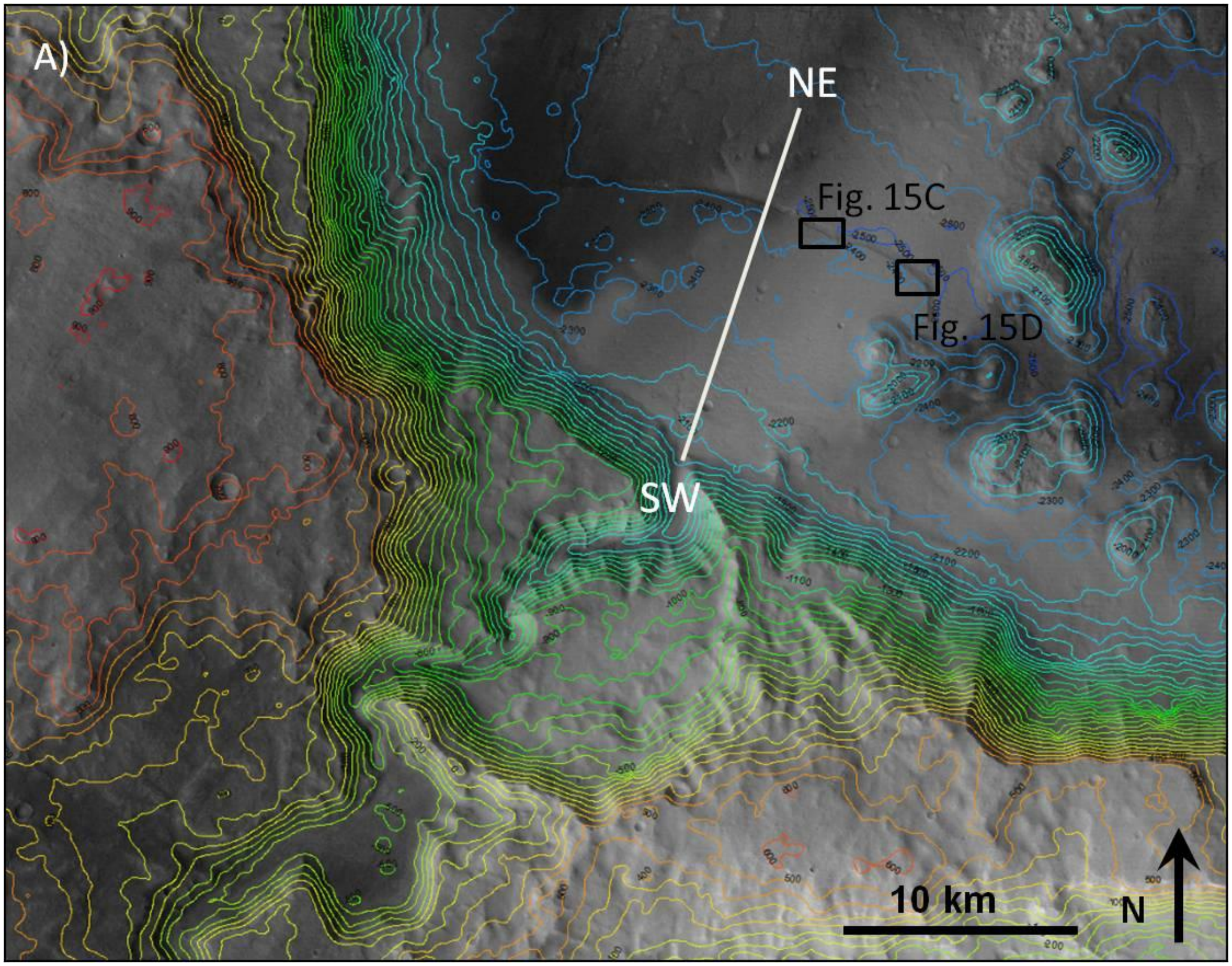

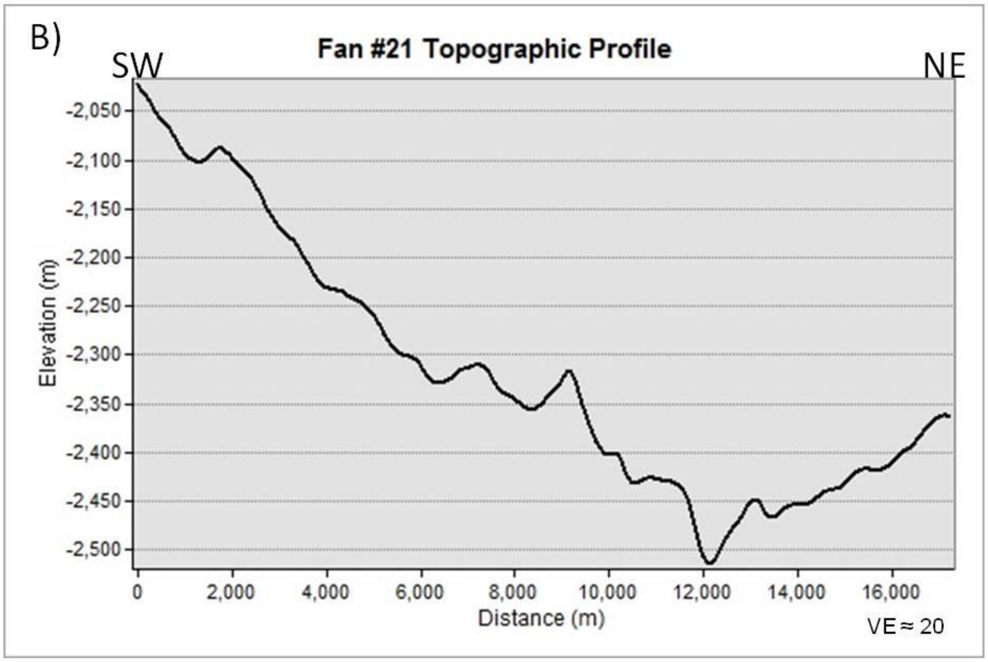

Figure 15B

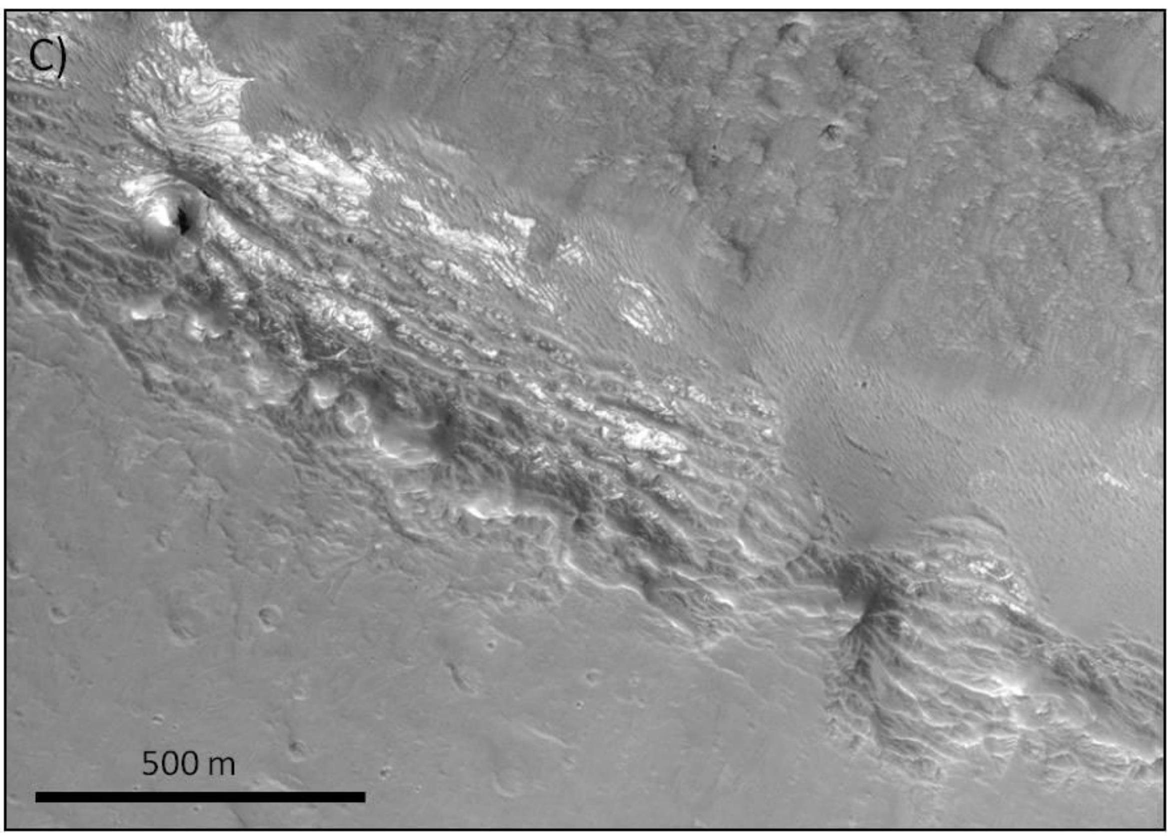

Figure 15C

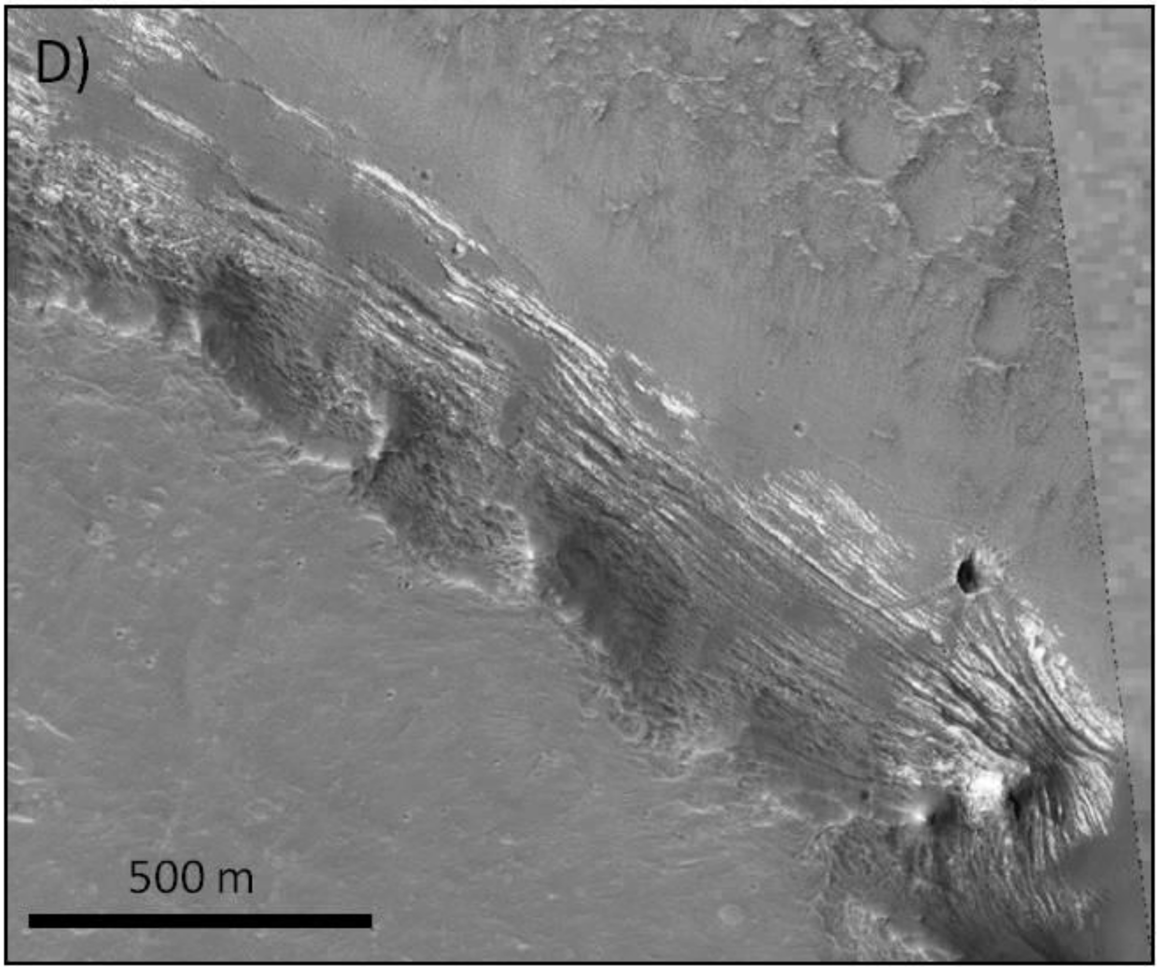

Figure 15D

Figure 16: A) CRISM phyllosilicate summary parameters (R: DB2300, G: 2210, B: BD1900) of images in crater containing Fan #25 overlain on HRSC image H4340_0009_ND4. Red/magenta regions in CRISM parameters represent locations containing Fe/Mg-phyllosilicates. White line shows location of topographic profile through crater from inlet valley to outlet valley, and yellow outlined CRISM image shows location of B). B) CRISM phyllosilicate summary parameters overlain on grayscale of image FRT944A showing phyllosilicate-bearing regions (red/magenta) on Fan #25 and in small elongate depression ("ED") superposed on southern fan surface. C) CRISM summary parameters highlighting diversity in mafic minerals (R: OLINDEX, G: LCPINDEX, B: HCPINDEX) for data in the crater. D) CRISM visible-wavelength summary parameters of oxidized iron minerals (R: BD530, G: SH600, B: BDI1000) for data in crater containing Fan #25 (data stretch same as Figure 3C). E) Topographic profile through crater containing Fan #25, showing a relatively flat floored crater that has likely been filled in with sediment.

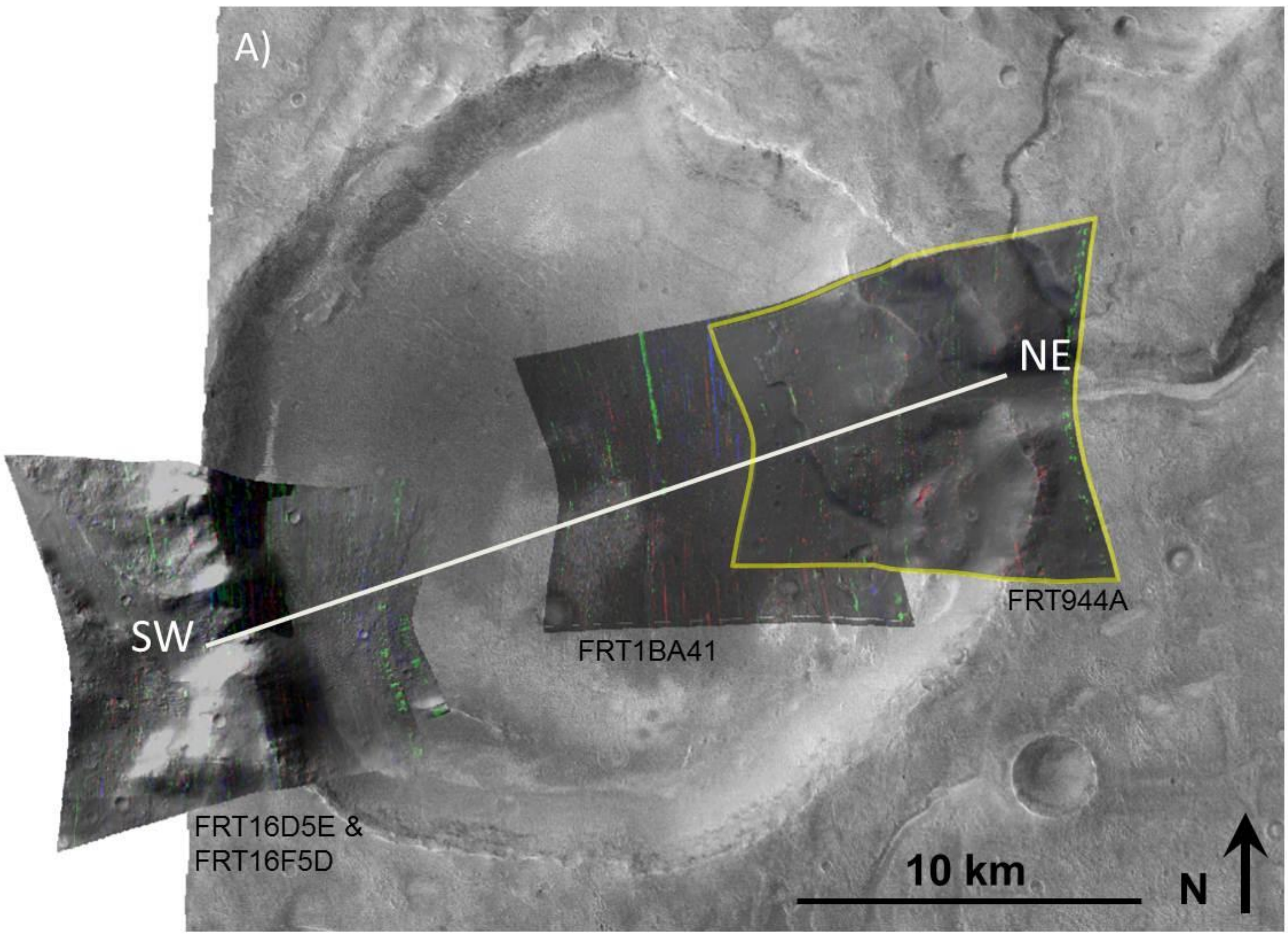

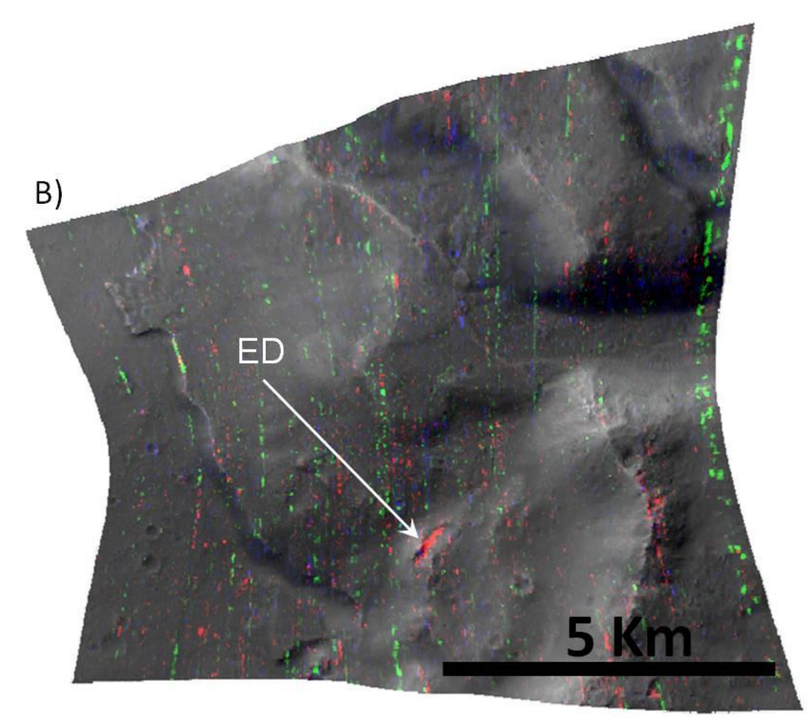

Figure 16B

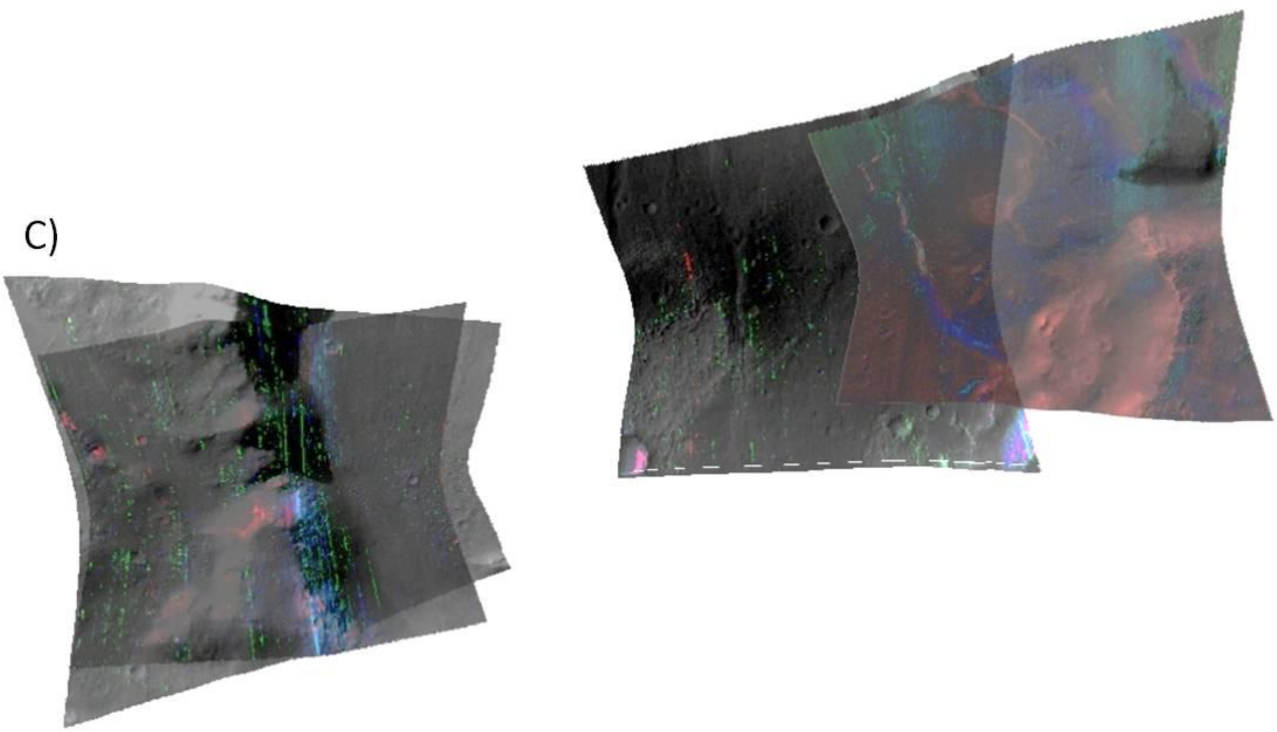

Figure 16C

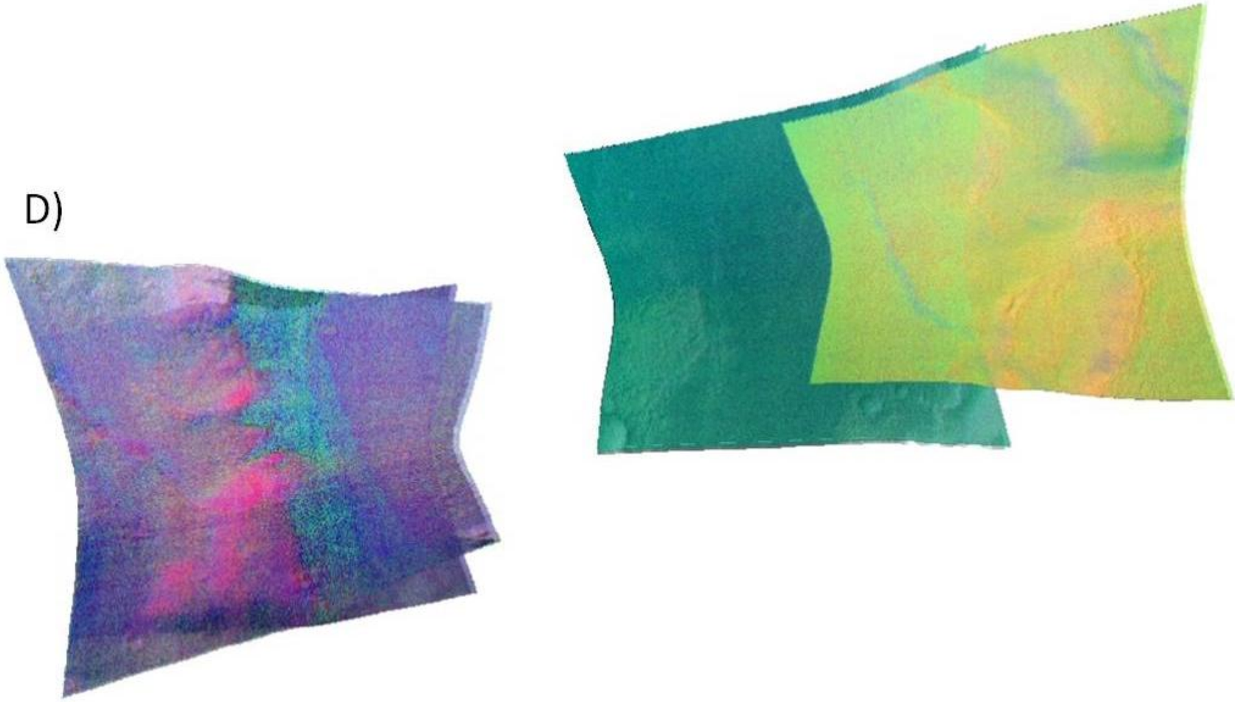

Figure 16D

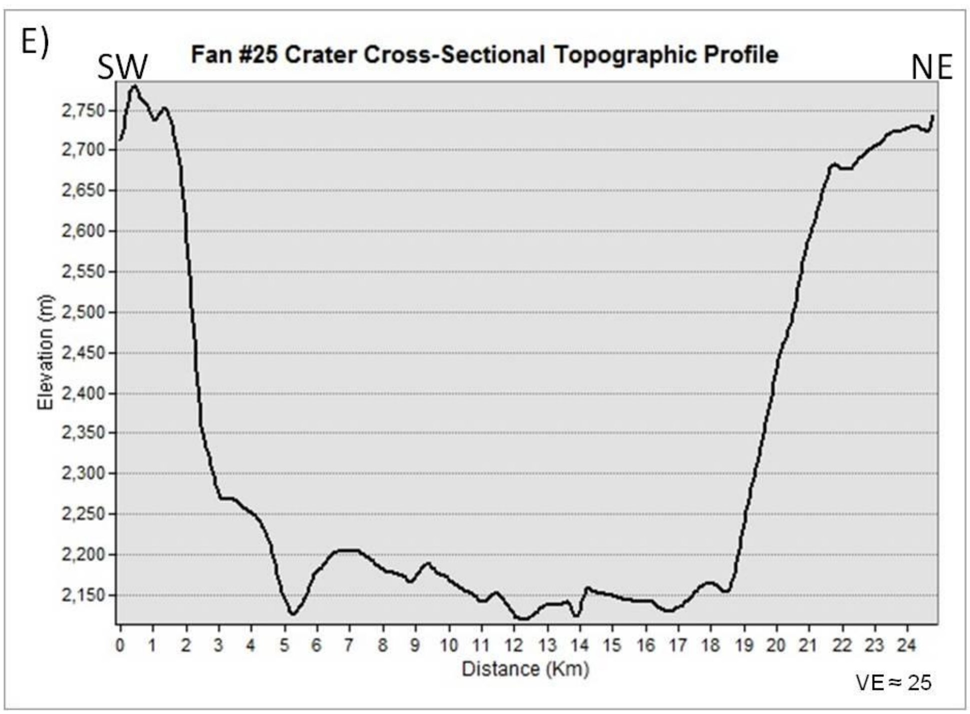

Figure 16E

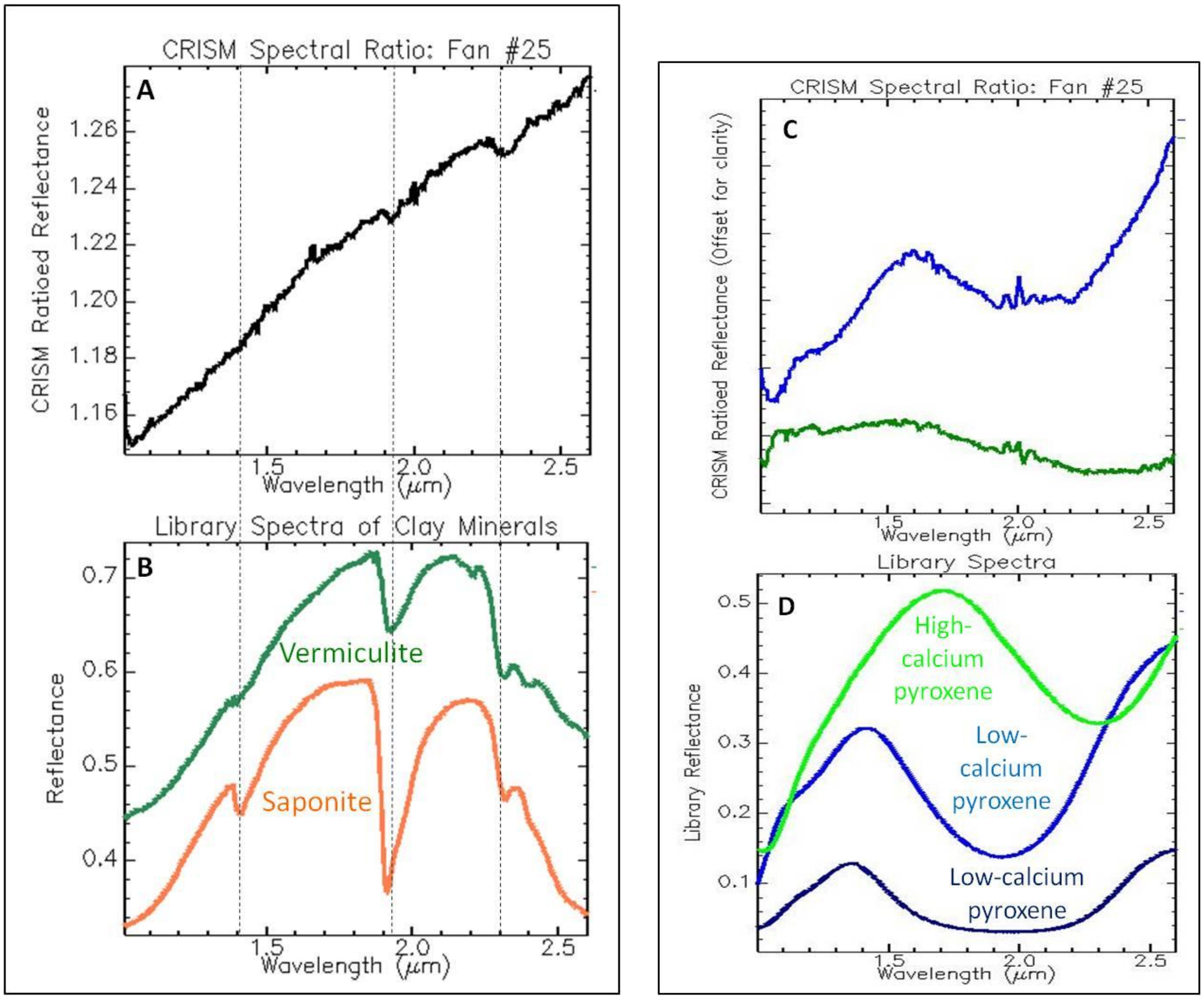

Figure 17: A) CRISM ratio spectrum of Fe/Mg-phyllosilicates on/near Fan #25. Absorption features are most consistent of an Fe/Mg-smectite, perhaps saponite and/or vermiculite. B) Library reflectance spectra of saponite and vermiculite for comparison. C)Spectra on Fan #25 displaying absorption features consistent with low- and high-calcium pyroxene (blue and green, respectively). D) Library spectra of pyroxene for comparison.

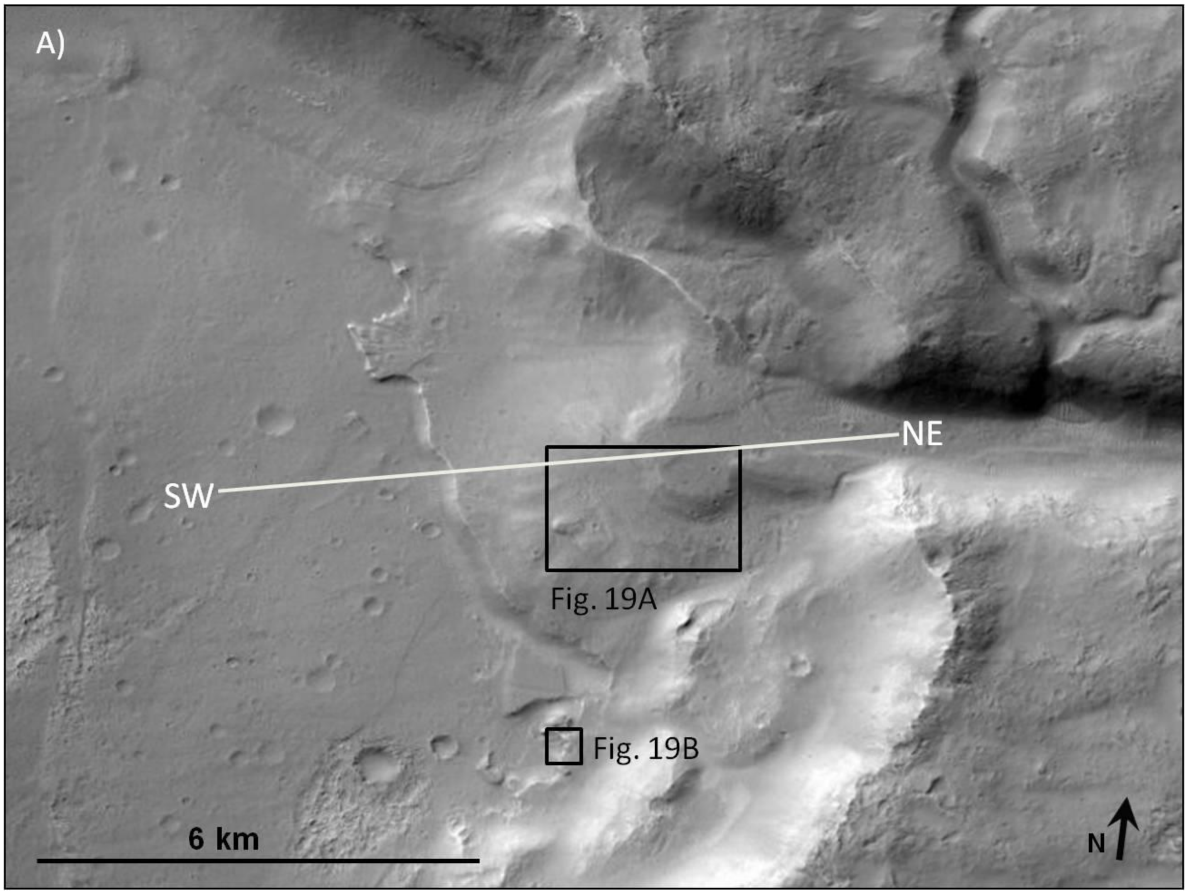

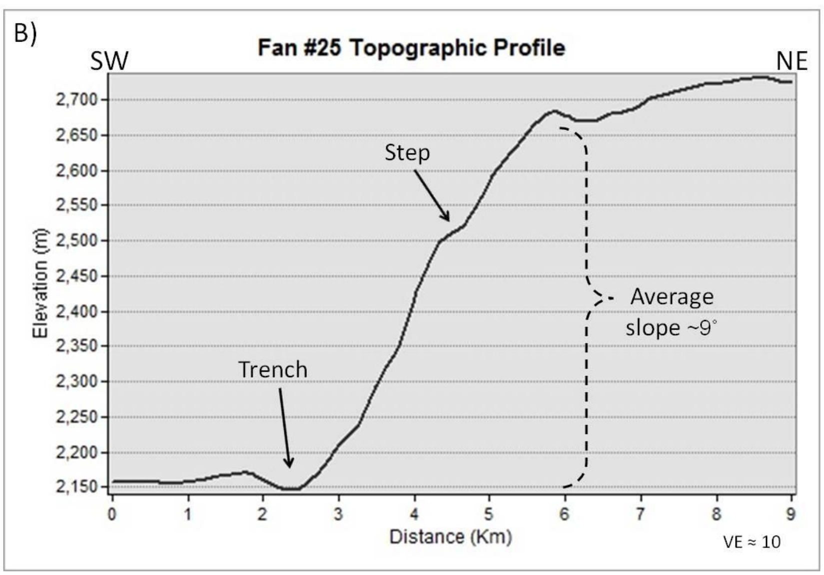

Figure 18: A) Portion of CTX image P15_006798_1405_XI_39S103W showing morphology of Fan #25. Boxes show locations of images in Figure 19. B) Topographic profile of Fan #25 showing relatively flat sloping top bottom regions, and a relatively steep scarp.

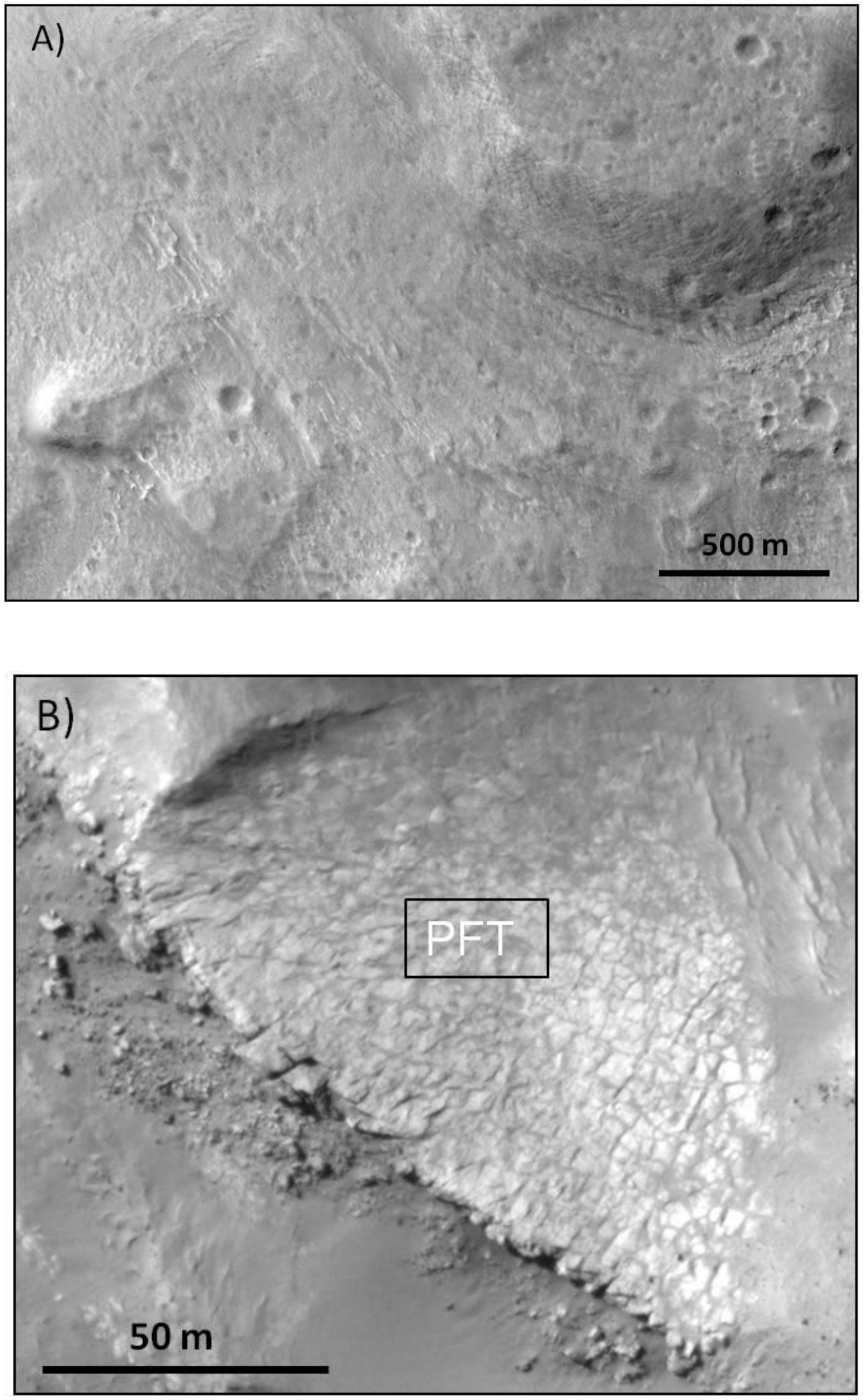

Figure 19: Portions of HiRISE image PSP_006798_1405 showing small scale morphologies on/near Fan #25. A) Possible layering on exposed fan scarp; B) polygonal fractured terrain ("PFT") in distal fan region.

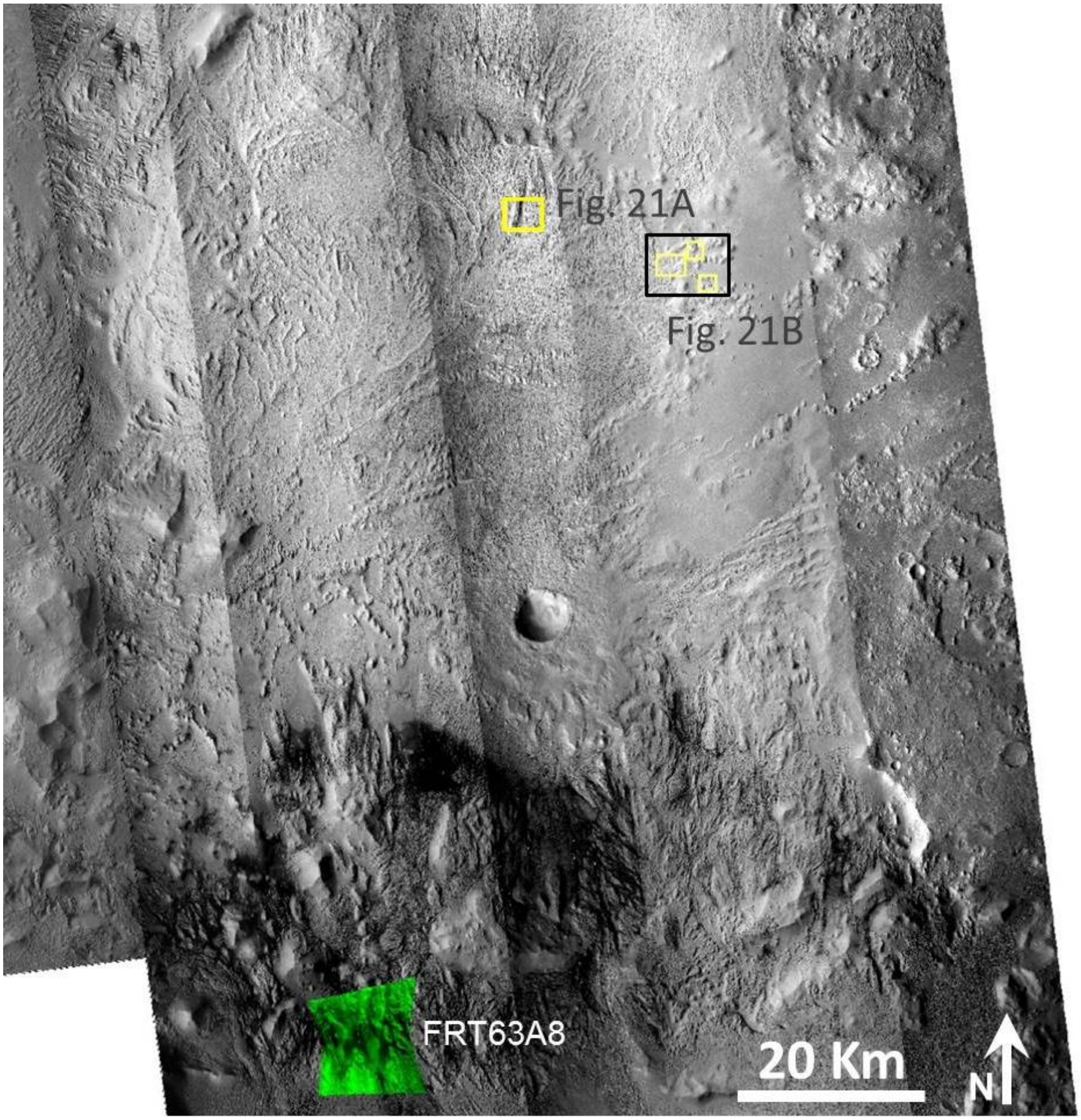

Figure 20: CTX mosaic showing large scale morphology of Fan #22. Green “bowtie” shape shows location of CRISM image associated with this feature; yellow boxes show zoomed in areas in Figure 21 (base image courtesy of Lefort *et al.*, 2011).

Figure 21: CTX images showing small scale features on/near Fan #22. A) Exposed layers in a small trough between sinuous ridge features (and N-S oriented yardangs between ridges); B) Layering exposed in distal portions of, and between sinuous ridge features, and C), D), & E) show close-up figures of areas yellow boxed in B). North is toward top for all images (images courtesy of Lefort *et al.*, 2011).

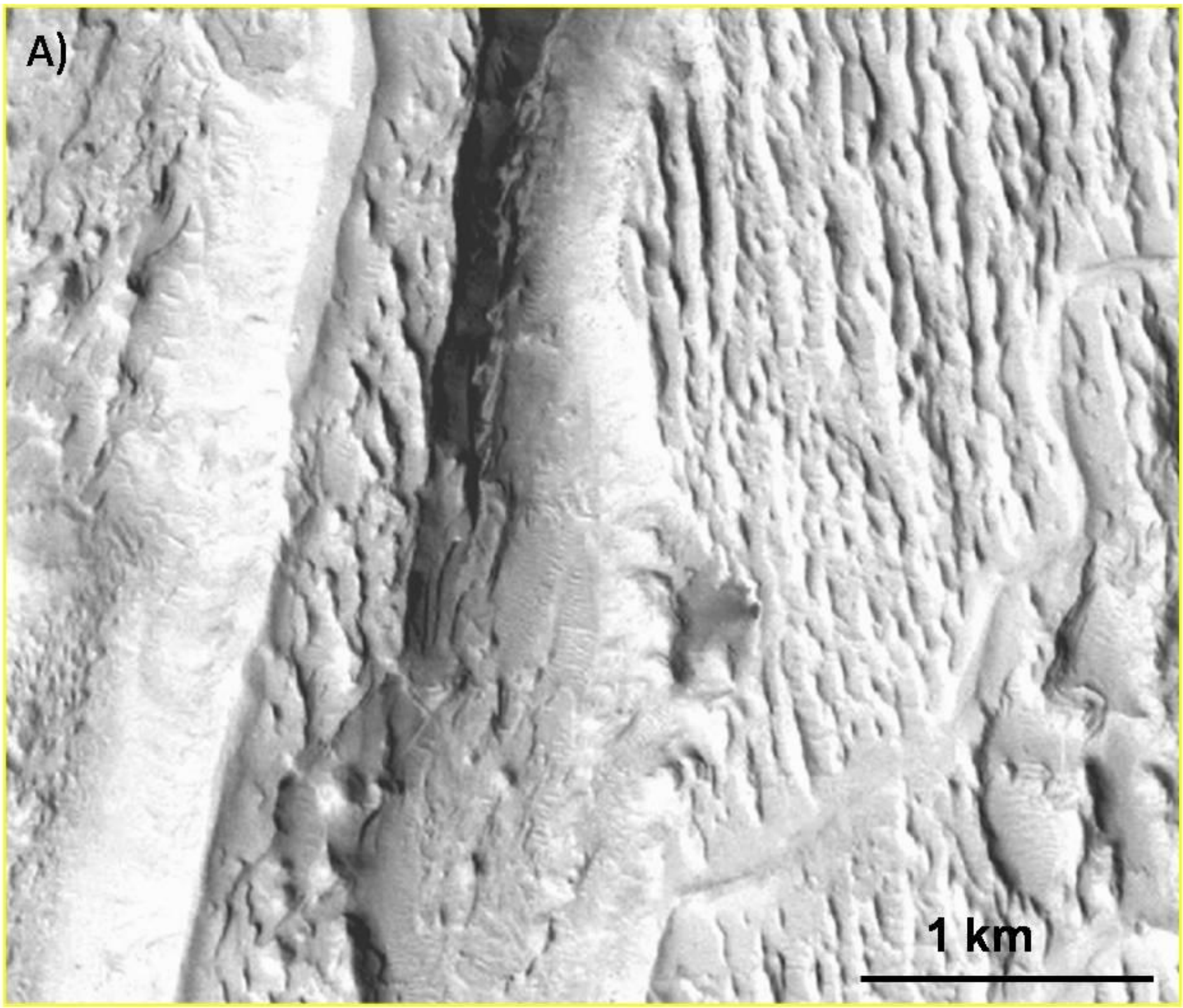

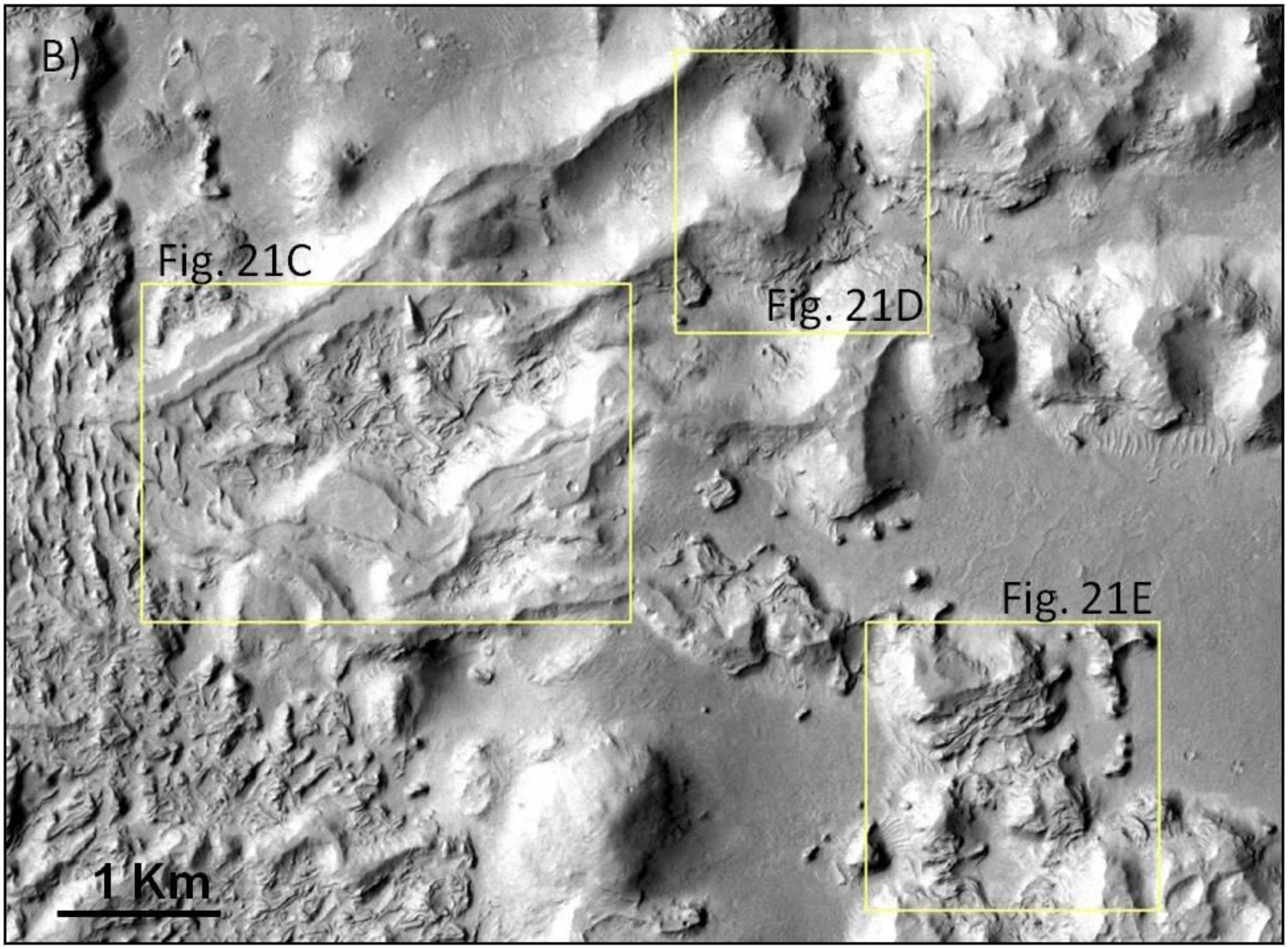

Figure 21B

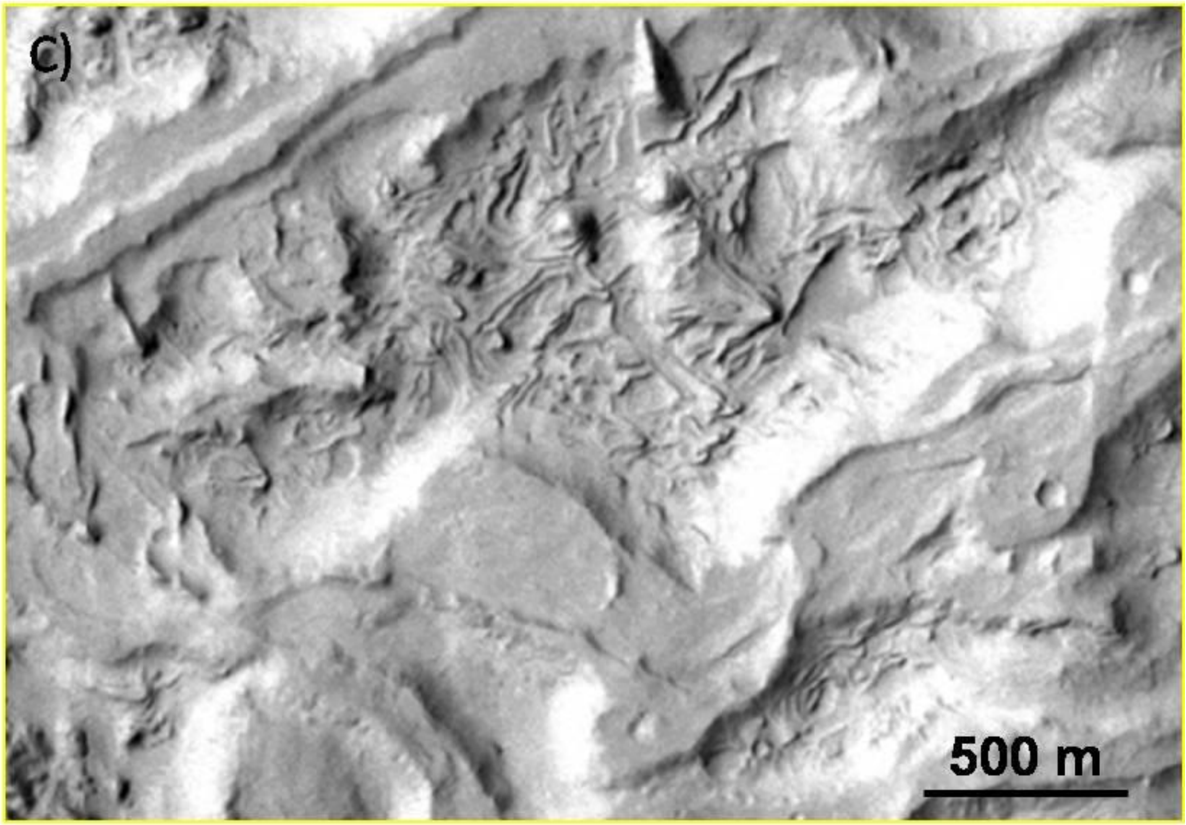

Figure 21C

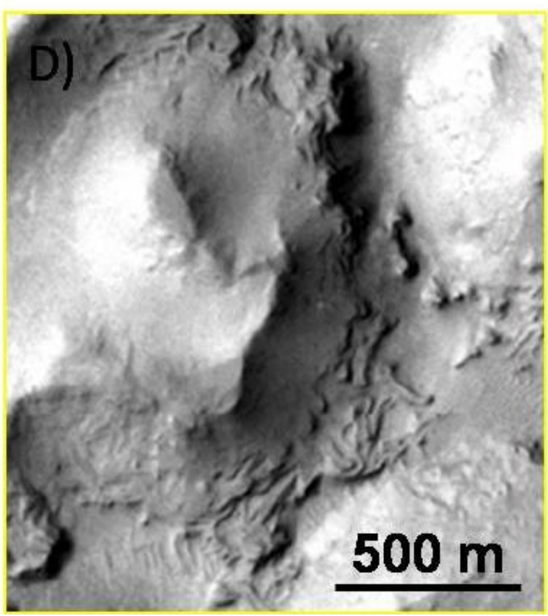

Figure 21D

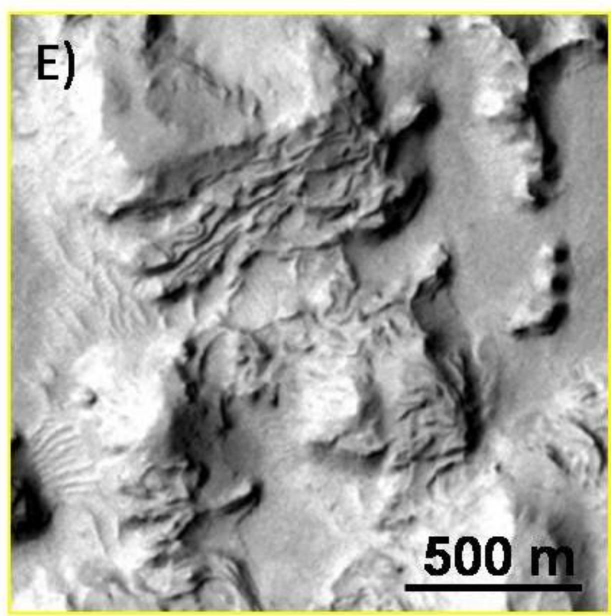

Figure 21E

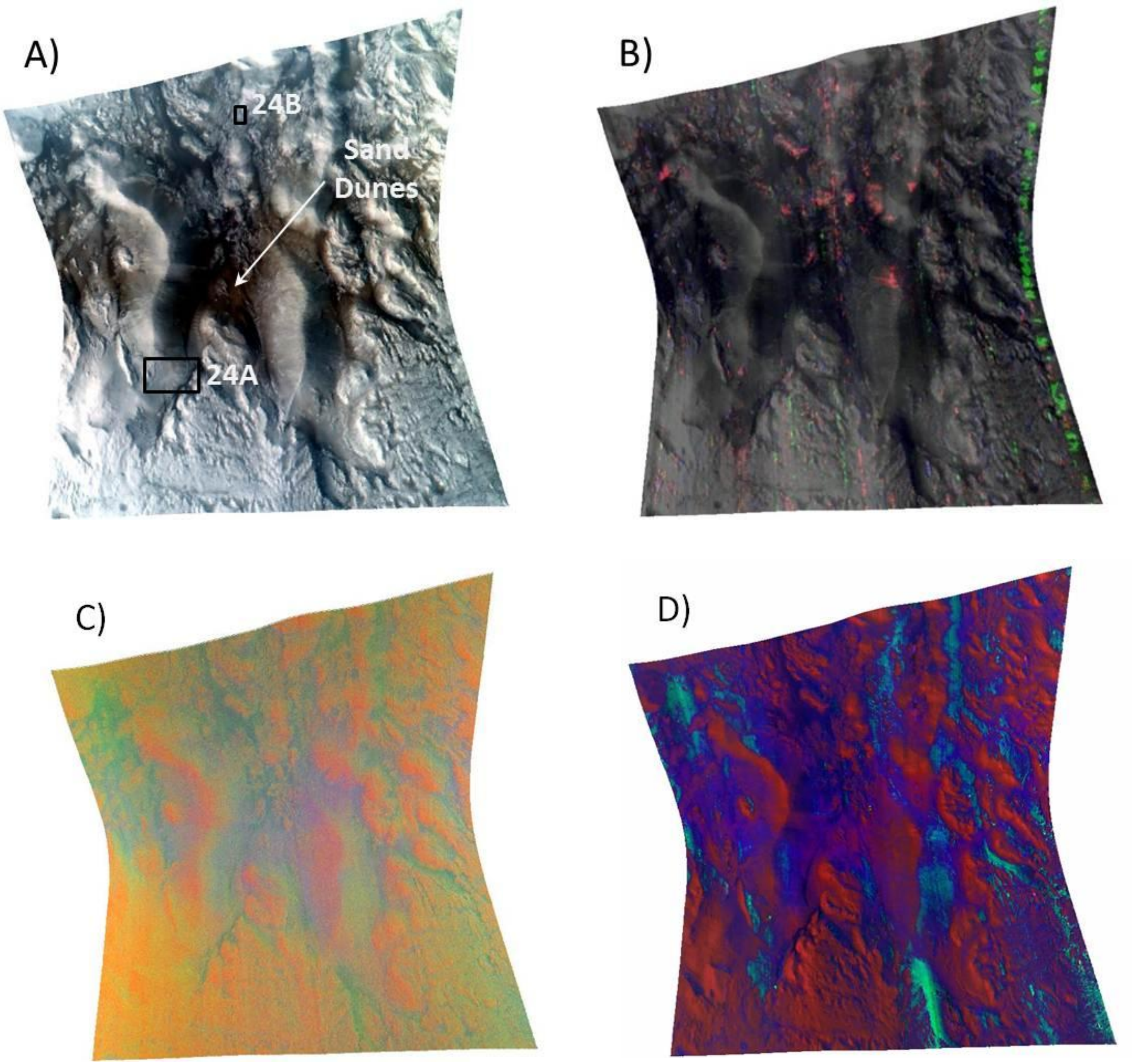

Figure 22: CRISM image near Fan #22; A) Default RGB composite of FRT000063A8 (arrow points to sand dunes between knobs and black boxes show locations of HiRISE images in Figure 24), and B) Phyllosilicate summary parameters (R: DB2300, G: 2210, B: BD1900) overlain on grayscale CRISM image showing the presence of phyllosilicates (red/magenta regions) on and distal to two semi-parallel, curvilinear, elongate knobs ~60 km south of Fan #22. C) CRISM visible-wavelength summary parameters of oxidized iron minerals (R: BD530, G: SH600, B: BDI1000) for this image; areas abundant in dust appear orange-yellow (data stretch same as Figure 3C). D) CRISM summary parameters highlighting diversity in mafic minerals (R: OLINDEX, G: LCPINDEX, B: HCPINDEX) for this image.

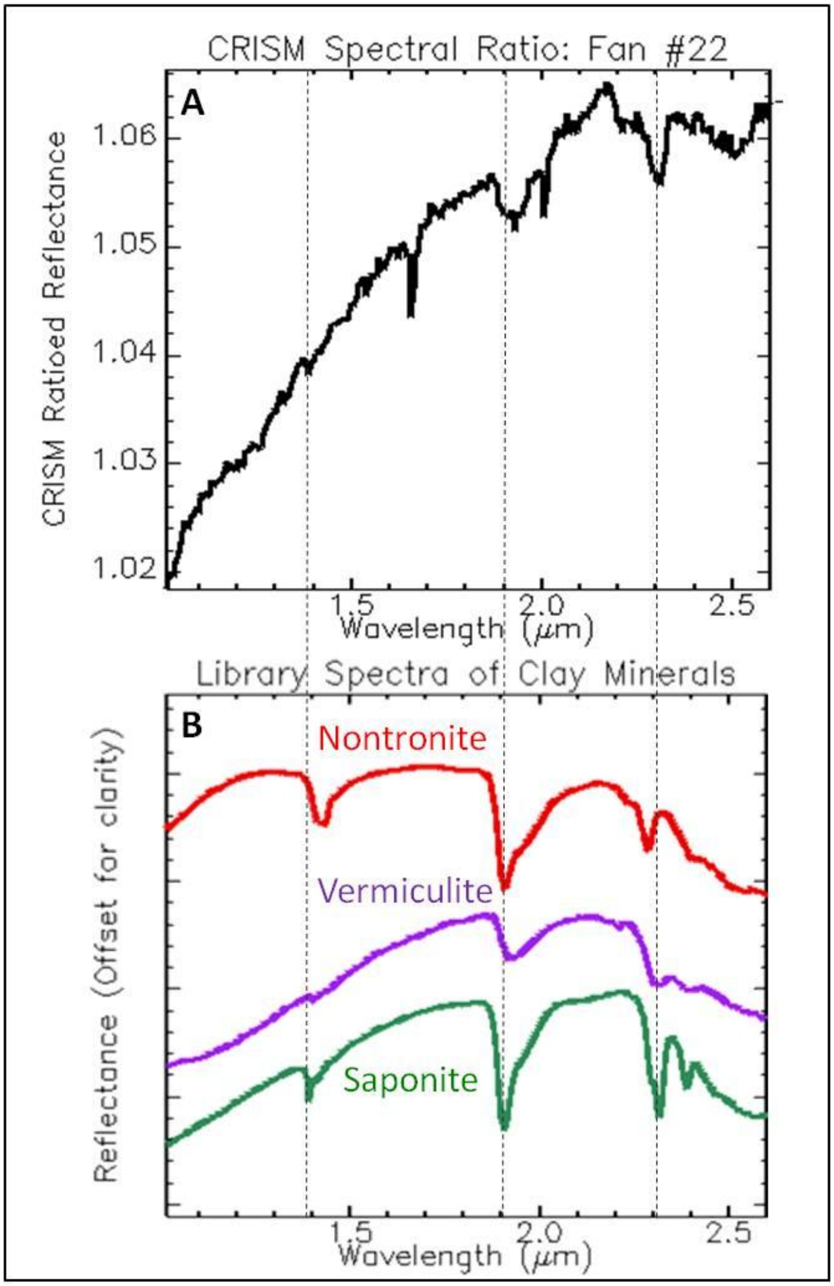

Figure 23: Spectra of hydrated minerals identified in CRISM image FRT000063A8, near Fan #22. A) CRISM Ratio spectrum of Fe/Mg-phyllosilicate-bearing regions in image FRT 0006A38, ~60 Km south of Fan #22. B) Library reflectance spectra of nontronite, saponite, and vermiculite for comparison.

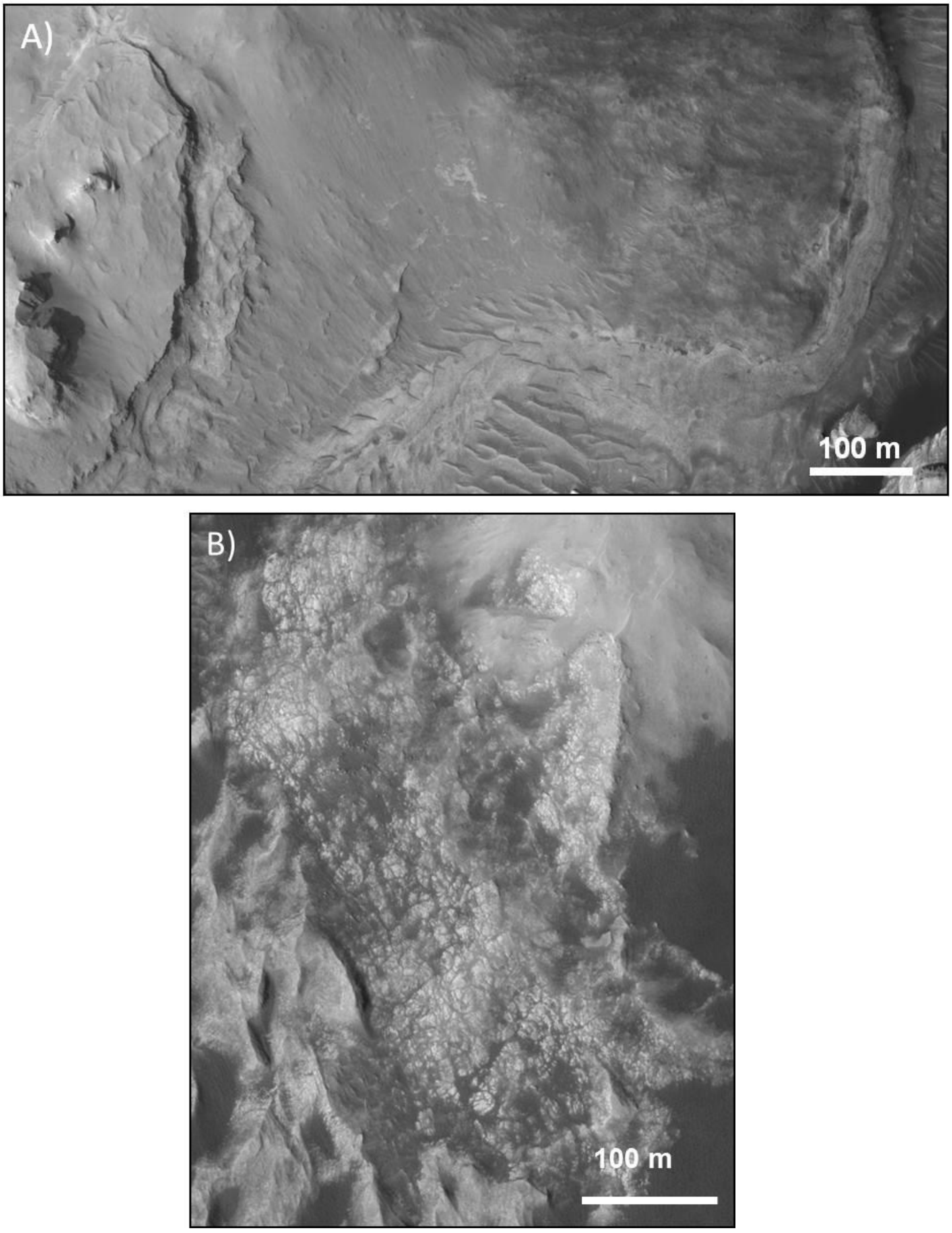

Figure 24: Portions of HiRISE image PSP_004125_1720 showing A) Layered, and B) fractured terrain associated with phyllosilicate-bearing regions in CRISM image FRT63A8 near Fan #22.

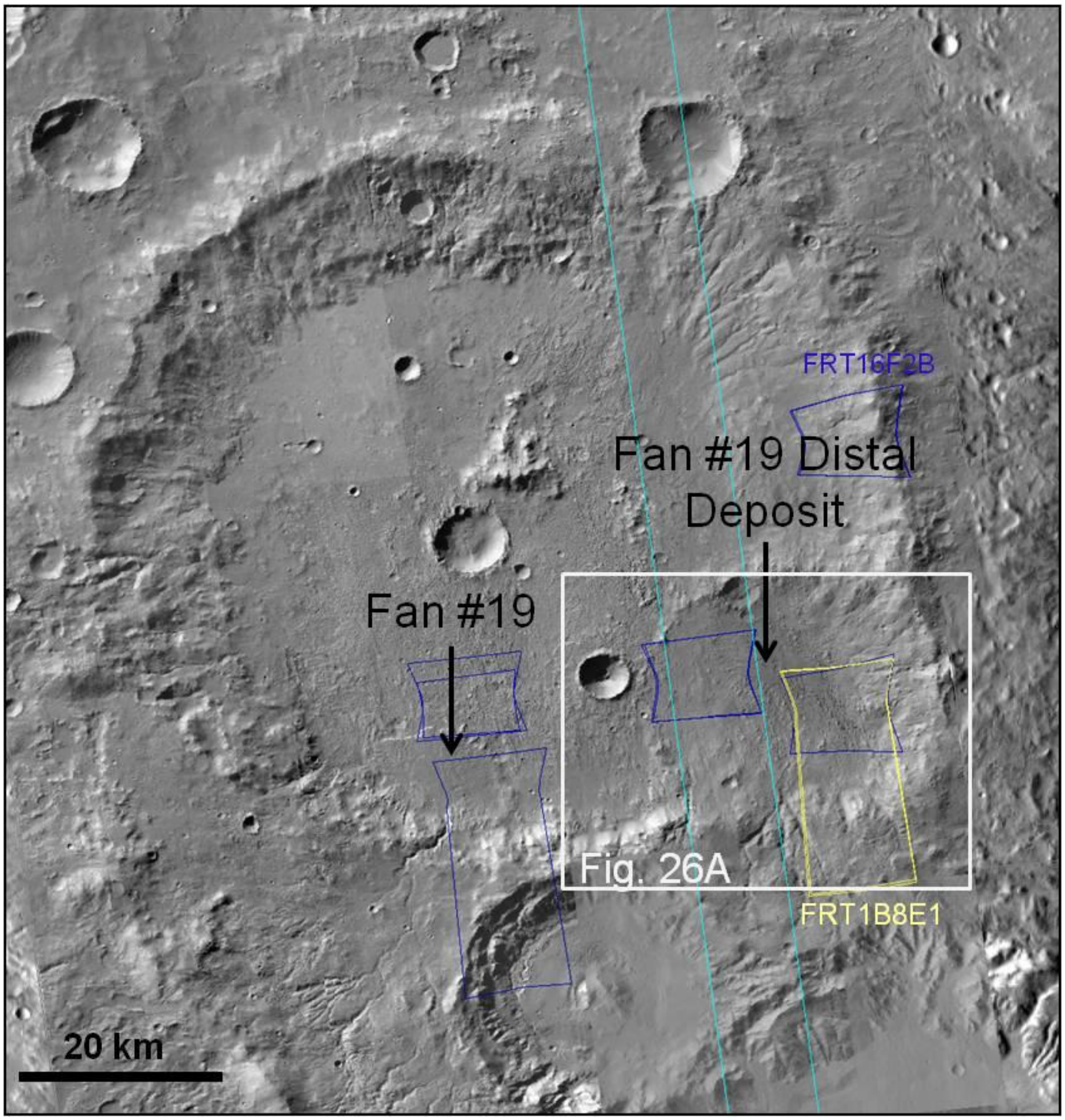

Figure 25: A) CTX mosaic of large unnamed crater (containing Fan #19) and smaller, superposing crater that contains Fan #19 Distal Deposit. White box shows location of Figure 26A. Blue bowtie-shaped outlines show CRISM footprints, and yellow bowtie-shaped outline shows footprint of CRISM image FRT1B8E1, where phyllosilicates were identified (Figure 27). Cyan rectangular strip shows location of CRISM multispectral image MSP0000821E_03 in Figure 29. North is toward the top of figure.

Figure 26: A) CTX mosaic of small crater containing Fan #19 Distal Deposit. Solid red line shows location of topographic profile, and dashed white arrows show examples inferred flow features, pointing in direction of flow. B) MOLA 128 ppd topographic profile over deposit, revealing steep slopes near the apex and shallow slopes in the distal regions of the deposit; blue line shows location of kink in the profile line. C) Portion of HiRISE image PSP_001754_1520 showing small scale morphologies on the deposit surface, including blocky textures, curvilinear ridge features (R), smooth intra-ridge regions (S), and boulder-sized clast inclusions entrained within and eroding from ridges (*e.g.*, white arrows). North is toward top of figures.

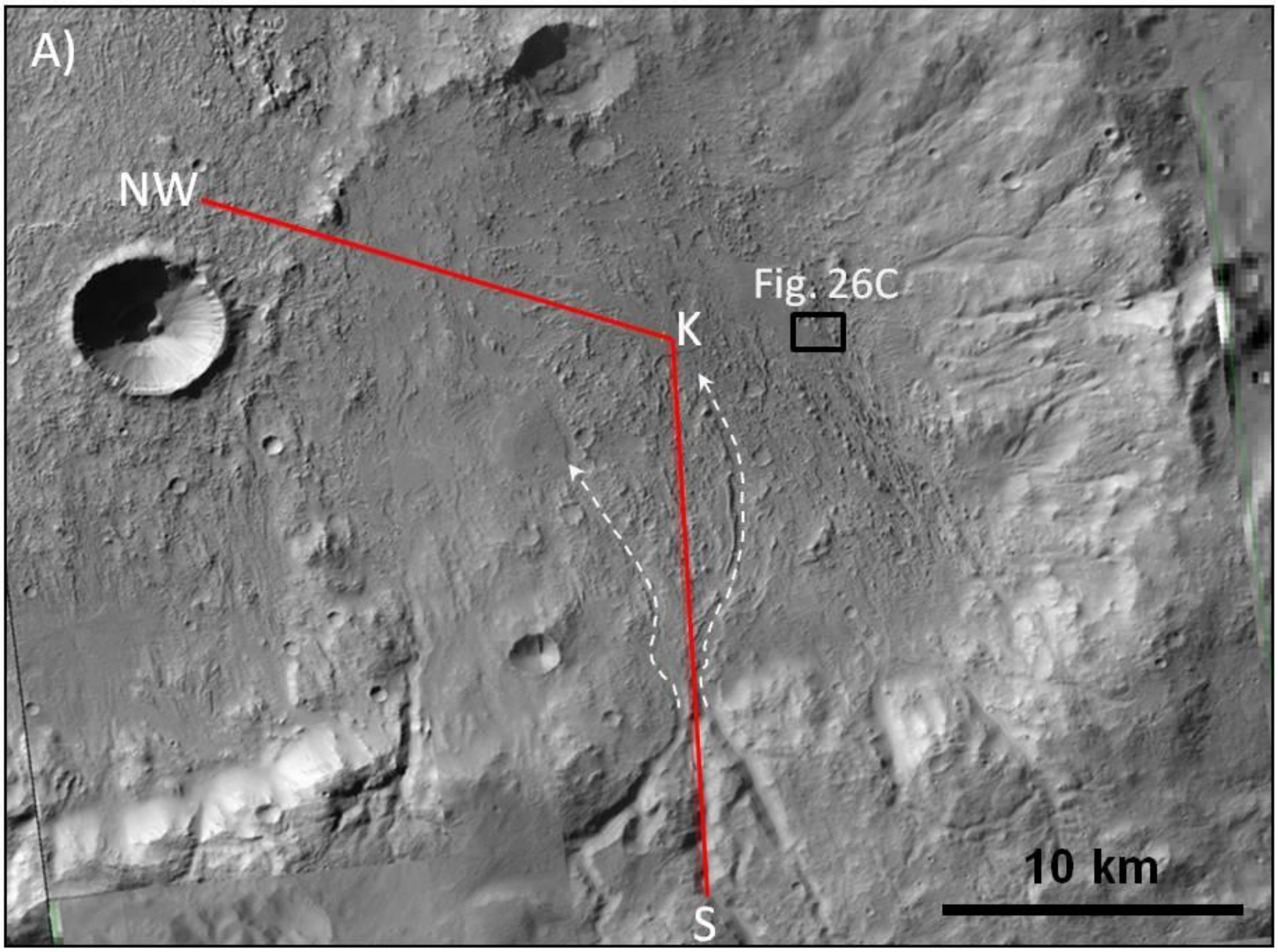

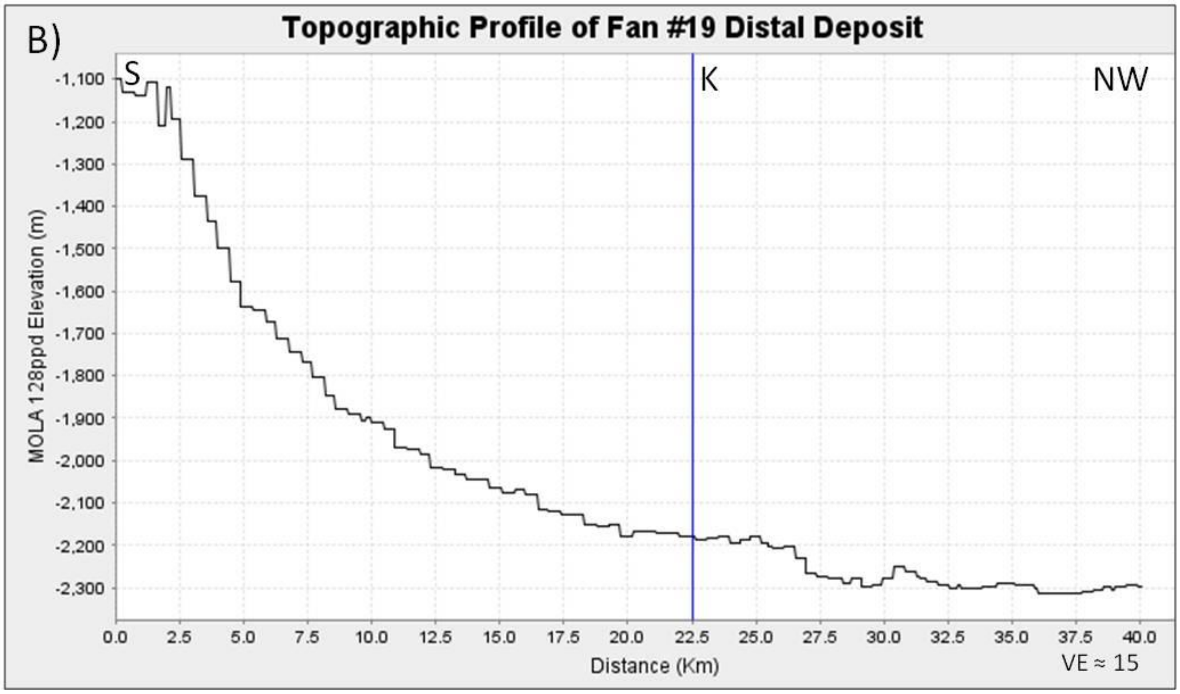

Figure 26B

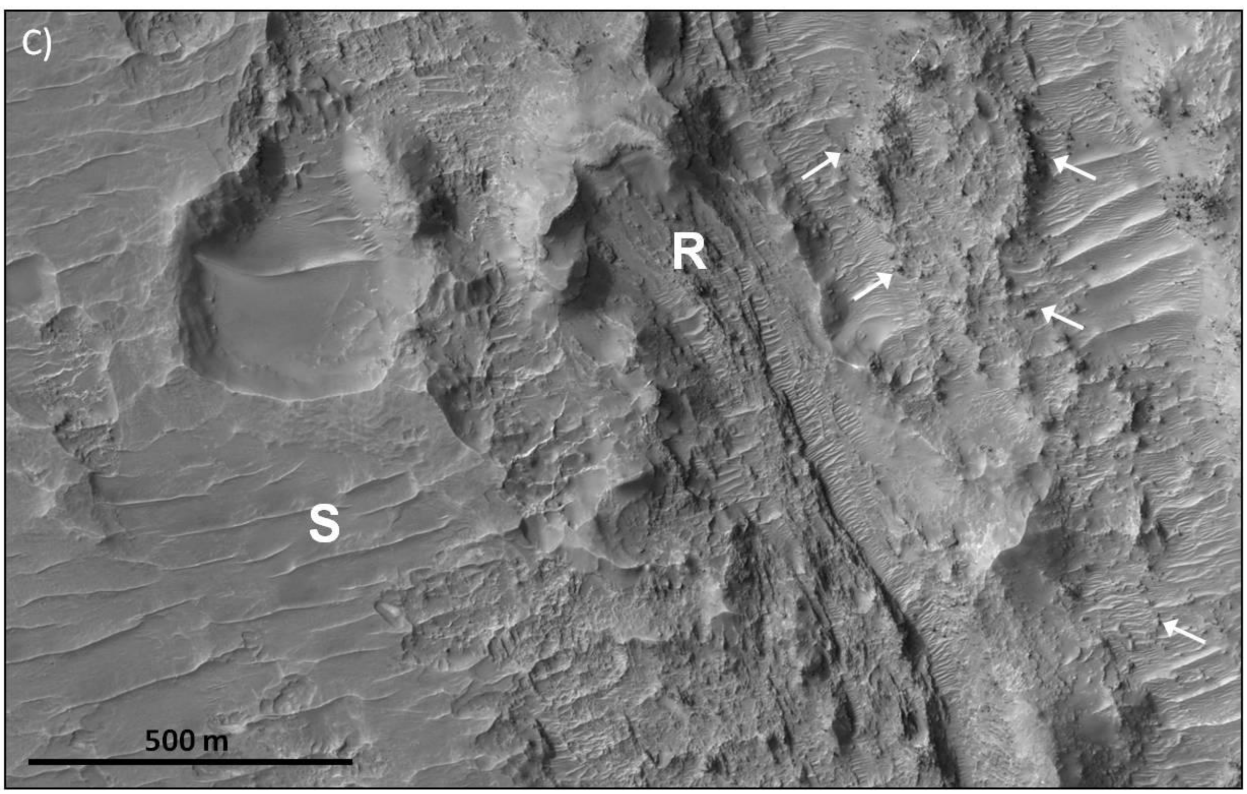

Figure 26C

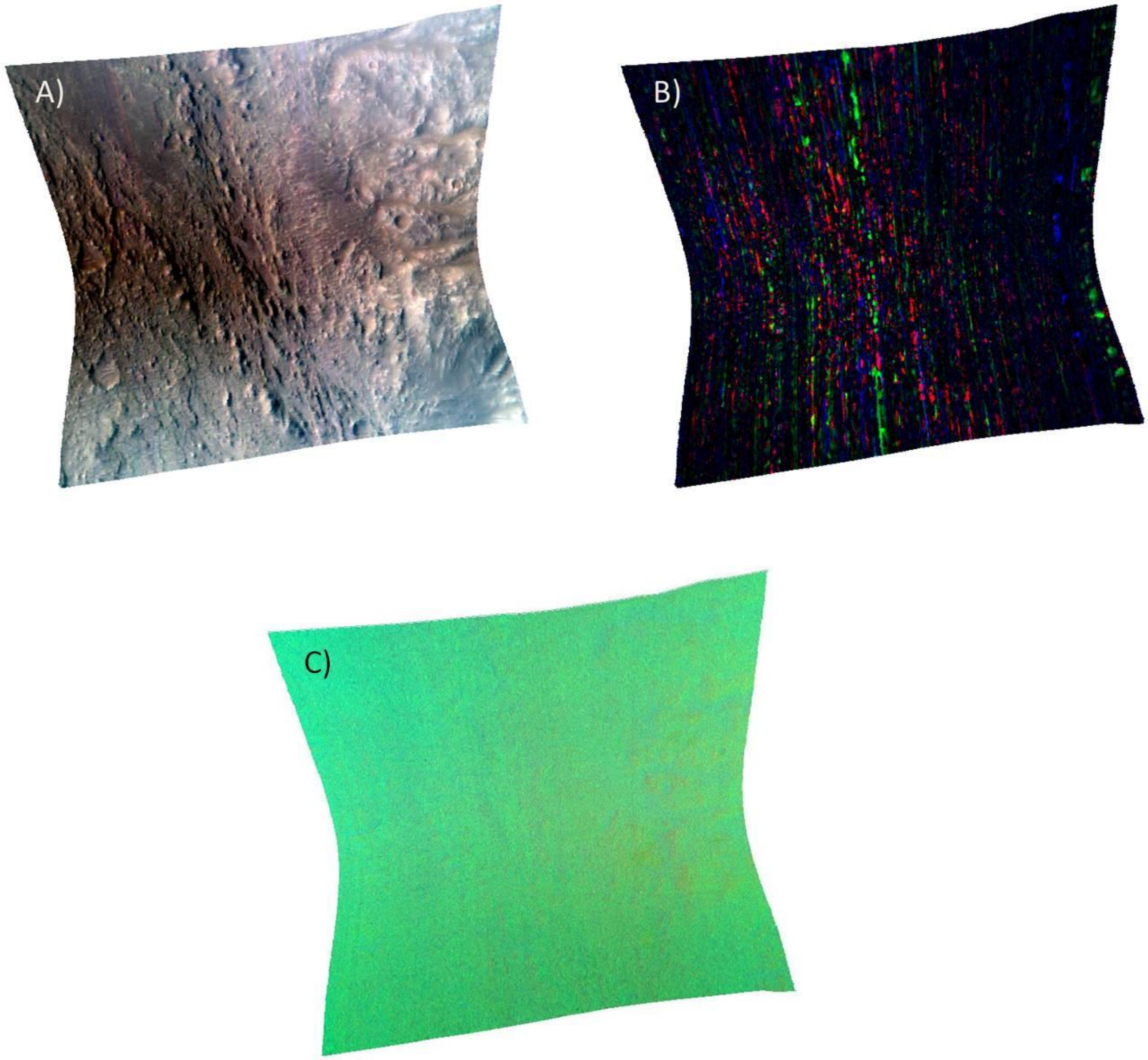

Figure 27: A) Default RGB composite of portion of CRISM FRT 0001B8E1, and B) CRISM phyllosilicate summary parameters (R: DB2300, G: 2210, B: BD1900) overlain on grayscale image, showing locations of phyllosilicate detections (red/magenta). Shadows/sharp brightness boundaries associated with ridge features in this image may cause detector artifacts in phyllosilicate summary parameters, therefore phyllosilicate spectra were taken from relatively flat –lying areas in this image. C) CRISM visible-wavelength summary parameters of oxidized iron minerals (R: BD530, G: SH600, B: BDI1000) for this image (data stretch same as Figure 3C).

.

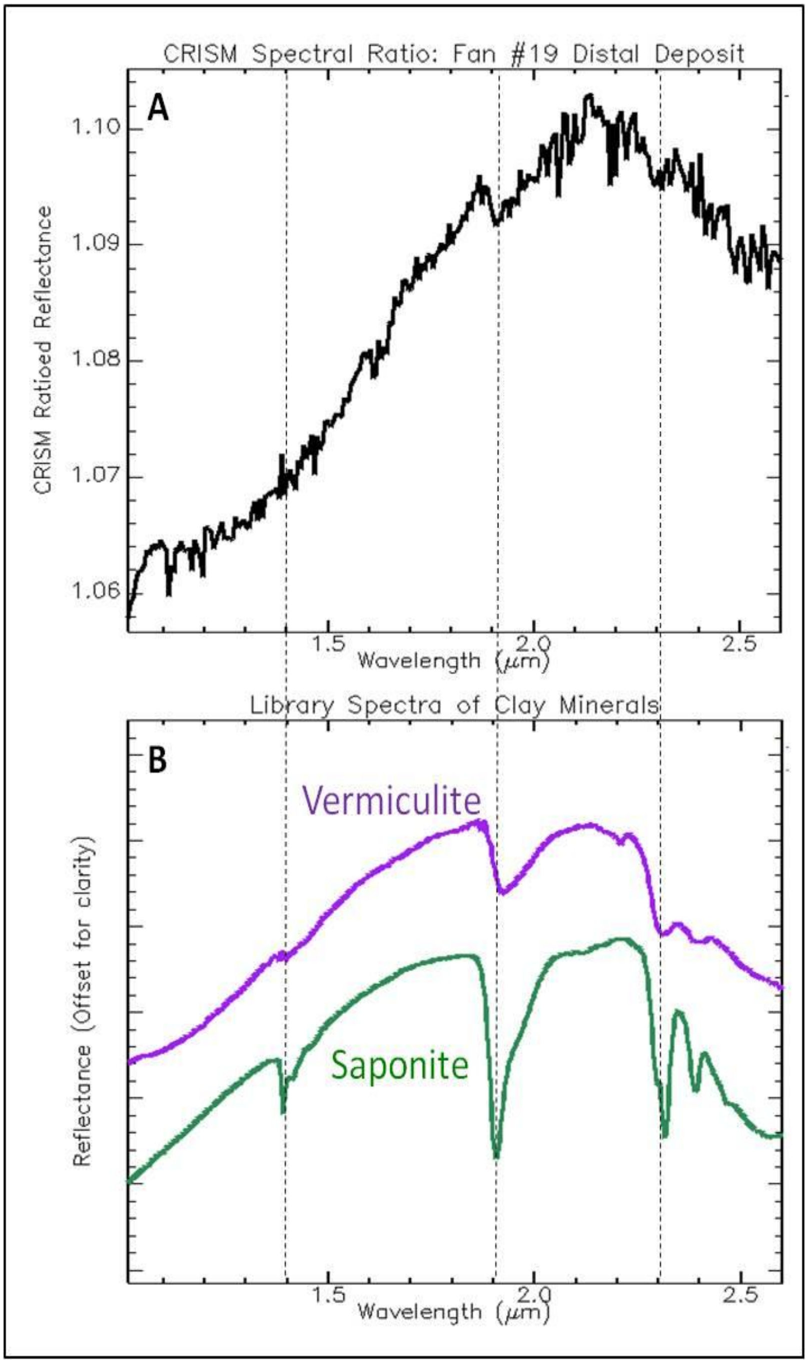

Figure 28: A) CRISM Ratio spectra of phyllosilicate-bearing region in image FRT 0001B8E1 on Fan #19 Distal Deposit. B) Library reflectance spectra of possible phyllosilicate mineral matches, saponite and vermiculite.

Figure 29: Portion of CRISM multispectral image MSP0000821E_03 over Fan #19 Distal Deposit, the containing crater, and larger adjacent crater (location shown in Figure 26A). A) Default RGB composite, B) Phyllosilicate summary parameter (R: DB2300, G: 2210, B: BD1900) overlain on grayscale image, showing widespread phyllosilicate detections (red/magenta colors) on the deposit and on the floors of both craters.

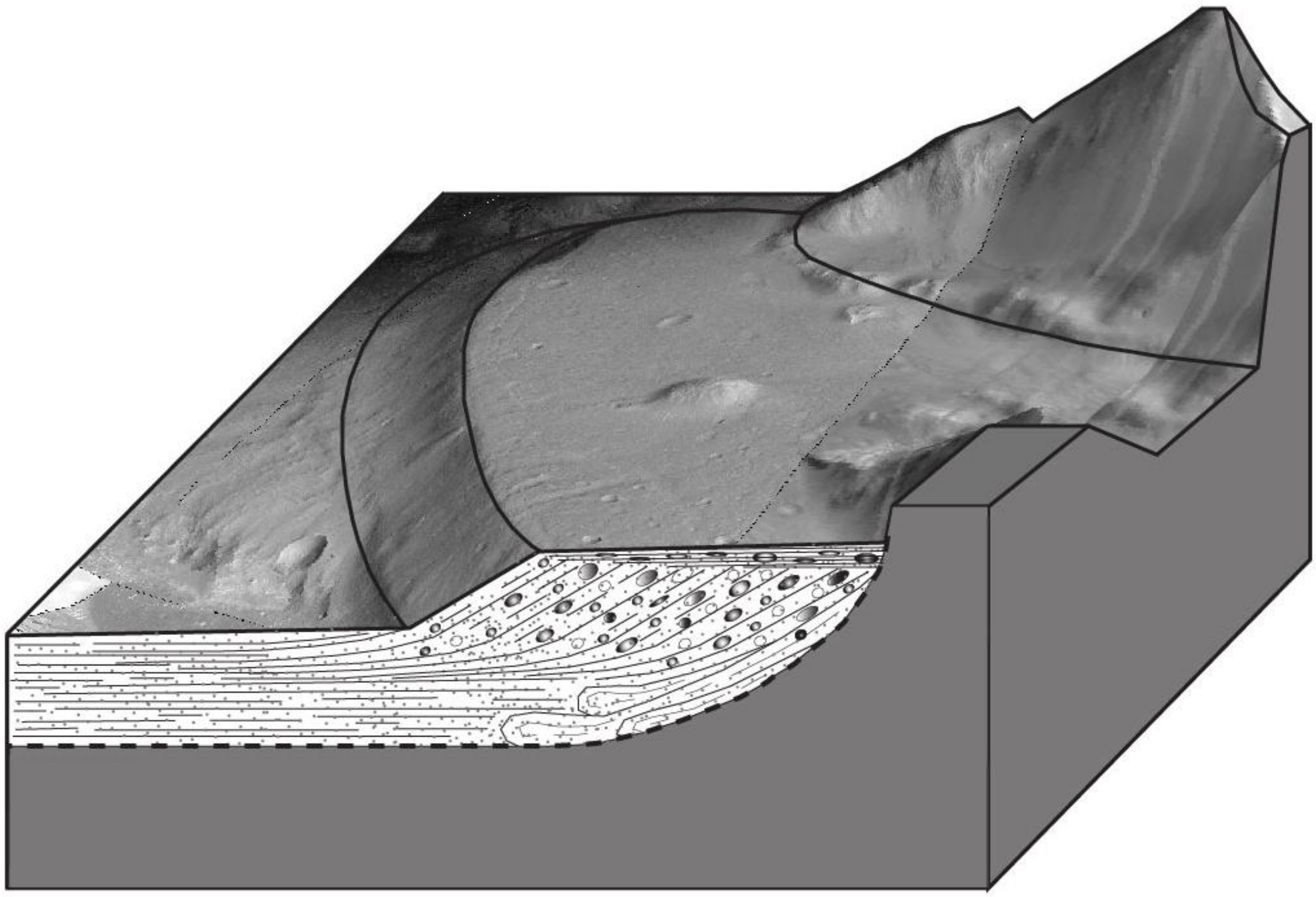

Figure 30: Simplified hypothetical block diagram of the internal structure of an intracrater Gilbert-type delta on Mars, based on terrestrial facies models and analogues (*e.g.*, White, 1992). Diagram shows a Gilbert-type delta that has built out over a subaqueous fan core (lobate deposits). The basal lobes accumulate vertically until reaching the mouth of the inlet valley, at which time delta formation and progradation begins. Internal structure of delta shows shallow-dipping topset beds, steeply-dipping foreset beds, and shallow-dipping bottomset beds. Grayscale surface image is HiRISE and CRISM data of Fan #26 overlain on HRSC DTM (2X vertical exaggeration).

VITA

Andréa C.G. Hughes attained her high school degree in 2004 from Baltimore City College in Baltimore, Maryland. She went on to complete a Bachelor of Science degree in Space Sciences at Florida Institute of Technology (Melbourne, Florida) in 2008. While pursuing her undergraduate degree, she worked as a research assistant studying high energetic radiation associated with lightning. Andréa earned a Master of Science degree in Geology with a concentration in Planetary Geosciences from the University of Tennessee in 2011. Her master's research, completed under advisors Devon Burr and Jeff Moersch, involved the identification and classification of hydrated minerals and morphologies associated with hypothesized Martian deltas (*i.e.*, aqueous deposits) in order to better understand the climatic and geologic history of Mars.

Andréa's dream career is to work as a research scientist and Mission Operations Specialist at the National Aeronautics and Space Administration (NASA), where she will facilitate the organization of manned, robotic, and spacecraft exploration missions of planetary bodies in the solar system.